Measurement and Prediction of Temperature-rise in Switching Cabinet

UNIVERSITY OF LIVERPOOL

Thesis submitted in accordance with the requirements of the

University of Liverpool for the degree of MPhil

By

Sicheng Zhao

January 2018

Department of Electrical Engineering and Electronics

University of Liverpool

Acknowledgement

Firstly, I would like to express my sincere gratitude to my supervisor, Professor Joseph Yan for his generous help and invaluable guidance throughout the duration of this project. Without his help, I would not have grown into a postgraduate research student who can understand how to carry out research and deliver the results industries want. I know my journey as a research student only began and there are a lot of hard work ahead of me. Thank you so much, Professor Yan, I have learned so much from you and you have given me the confidence to continue the journey!

Secondly, I would like to acknowledge the help from the Department of Electrical Engineering and Electronics for providing relevant facilities and resources to conduct my research, and also the financial and technical support from Pinggao Group Co. Ltd.

Thanks to all my colleagues in the Department of Electrical Engineering and Electronics at the University of Liverpool for your help, companionship and encouragement. Together, we grow in the last two years, and our friendship will last for life.

Last but not least, I wish to express my gratitude to my family for their unconditional love and support, during my MPhil study at the University of Liverpool.

Abstract

Modern electrical equipment tends to be designed in a more compact way, higher in power rating and smaller in size. Therefore, thermal management has become a dominating issue in product design, type test and online monitoring. Technically, it is necessary to maintain a reasonable temperature for all the components under operating conditions, irrespective of high load current or excessive environment temperature.

The main purpose of this research is to perform reliable temperature measurement inside a model busbar compartment and develop a simulation model to predict the temperature field and thermal-flow field in the three dimensional space of the cabinet.

The work in this thesis consists of three parts. Firstly, the experimental setup that consists of a high current source, the model busbar compartment and the temperature measurement system, was designed. Calibration tests of thermocouples and data acquisition systems were carried out to define the measurement accuracy. Secondly, a widely used contact resistance model was validated by experimental tests with the empirical model parameters to suit the busbar joint used in the compartment. Lastly, a study based on mesh refinement was carried out to assess the suitability of the boundary conditions. The simulation results based on the developed mathematical model agree well with the experimental results.

This thesis presents a computational fluid dynamics (CFD) based simulation methodology for studying the phenomena of thermal-flow field in modern electrical apparatus. It will be useful to predict the maximum temperature-rise (hot spot) and the flow of thermal energy in the three dimensional space of switching cabinet, hence providing useful information to optimize product design. The simulation tool can also be used to confirm an improved design by comparing the relative largeness of the temperature of the hot spot.

Contents

Figure List

Table List

Symbol List

I	Load current
t	Time
$\Delta\theta$	Temperature-rise
$R_{conduction}$	Conductive thermal resistance
L	Characteristic linear dimension
k	Thermal conductivity
$R_{radiation}$	Radiative thermal resistance
h_R	Radiation heat-transfer coefficient
ε	Emissivity of radiation surface
$\sigma_{Stefan-Boltzmann}$	Stefan-Boltzmann constant
F_{1-2}	View factor for radiation dissipating from surface 1 to the absorbing surface 2
T_1	Temperature of surface 1
T_2	Temperature of surface 2
$R_{convection}$	Convective thermal resistance
h	Heat transfer coefficient
σ	Electrical conductivity
V	Electrical potential
E	Electrical filed
Q	Joule loss heating
σ_T	Electrical conductivity at individual temperature T
T	Temperature
ρ_{ref}	Electrical resistivity at reference temperature
T_{ref}	Reference temperature
α	Temperature resistivity coefficient
J	Current density
h_c	Constriction conductivity of contact area
φ_2	Higher voltage potential of contact surface
φ_1	Lower voltage potential of contact surface
$\sigma_{contact}$	Electrical conductivity of contact surface
m_{asp}	Average slope of the microscopic asperities on contact surface

σ_{asp}	Average height of the microscopic asperities on contact surface
H_c	Reference micro-hardness
p	Pressure
σ_1	Electrical conductivity of one of the contact materials
σ_2	Electrical conductivity of the other contact material
n_d	Unit vector
$Q_{contact}$	Heat generated by contact resistance
q	Heat flux
T_{amb}	Ambient temperature
Γ	Diffusion coefficient
k_{air}	Thermal conductivity of air
μ	Dynamic viscosity
R_e	Reynolds number
ρ	Density
u	Velocity vector
I	Three-dimensional identity matrix
C_p	Heat capacity
$R_{specific}$	Specific gas constant of air
F	Volume force
δ	Thickness of thermal boundary layer
R_j	Resistance measured of busbar joint
R_s	Spreading resistance
R_i	Contact resistance
a	Width of busbar
b	Thickness of busbar
l	Length of overlapped area of busbar joint
e	Resistance ratio of spreading resistance
n	Number of bolts used in busbar joint
d	Diameter of bolt at busbar connection
T_q	Torque
K	Nut factor of bolt
S	Area of busbar cross-section
A	Surface area

Chapter 1 Introduction

1.1 Background

Power systems have been rapidly developed all over the world in the past fifty years, at both transmission and distribution levels in terms of voltage level and power capacity. The highest voltage level of HVAC transmission has been increased to 1000 kV [1], as compared with 275 kV or 132 kV commonly used by most of the transmission systems in the 1960s, whilst the highest power rating of a 1000 kV transmission corridor has reached 9 GW. With the increase of voltage and power, the fault current level of a modern transmission system is also increased, which requires better and faster control and switching devices to change the topology of power network and protect operating apparatus from the fault. On the other hand, modern distribution networks tend to integrate more advanced automation and control functions for secondary system and primary equipment tend to become more compact in design. It is worth mentioning that with the development of modern computer, micro-controller and sensor technology, the automatic control and protection systems have been further developed to ensure that the primary power system can be operated with high reliability, stability and safety.

With the advance in electrical apparatus technology, an important objective for apparatus manufacturers is to increase the competitiveness of their products in terms of reducing the product size and cost. In addition, if a manufacturer can provide a maintenance-free product or at least guarantee to reduce the frequency of maintenance, it would place the manufacturer in a more advantageous position than its competitors. However, the reduction of product size will have some technological consequences, and one of the consequences is that the space between the components becomes smaller, imposing further constraints on electrical insulation

and thermal management. As far as temperature is concerned, thermal management is one of the most important aspects that need to be addressed at the design stage of apparatus.

Temperature-rise control is central to thermal management. It is well known that the load current carried by a conductor generates Ohmic heating and tends to raise the temperature of the conducting material over the ambient. Heat has to be removed from the heat generating location to reach a steady-state operation condition. If the heat generated cannot be managed or dissipated effectively, the components, especially the ones covered with solid insulation, will become hot or even overheated, and this may lead to insulation degradation or hardware failure.

It is thus necessary to control the temperature-rise and manage the heat dissipation. A proper design with appropriate thermal management for the apparatus can provide a longer life span and reduce the maintenance frequency during its normal operation. Taking a switching cabinet as an example, thermal management is very important if we consider the competitive market for distribution apparatus and the demand for compact design. Excessive temperature-rise over a long time not only results in weakened mechanical strength of the conducting materials and bolted connections, but also deteriorates the dielectric strength of the insulation materials [2]. The consequences would be either a shortened lifetime of the apparatus or a catastrophic pre-mature failure of the apparatus during its normal operation.

For most electrical apparatuses such as cables, transformers, over-head line and switching cabinets, gas and oil are mostly used as the cooling medium. The cooling process of electrical apparatus is always most efficient with flow of gases, and therefore, thermal management is focused on the coupled thermal-flow field study. Traditionally, the most commonly used strategy to study thermal behaviour is by experimentation with prototypes, as mentioned in [3]. Indeed for a long time, empirical formulas have been derived from the experimental results which were

subsequently used to guide the development of new product. However, experimental tests require expensive laboratory devices and time consuming. In addition, every new prototype will need tests and experimental analysis for its thermal performance.

Fortunately nowadays, experimental techniques can be co-operated with a wide range of effective numerical modelling and analysis methods, which allow the design of a new product to become more affordable, rapid and efficient. This is a result of increasing computational power as well as the improvement of mathematical methods and numerical algorithms [4]. Numerical modelling is nowadays a popular method to analyse heat transfer and fluid dynamics. Due to the continuous progress in Computational Fluid Dynamics (CFD), numerous commercial software packages have been developed to enable convenient setup of the thermal study. Hence, simulation and modelling approaches are being used to develop new products of electrical apparatus.

Based on the knowledge of heat transfer, the temperature variation in the electrical apparatus is predicted to optimize the design of those devices. It is reported in [5] that the use of three-dimensional (3-D) models for mechanical and cooling design by means of CFD software is becoming the standard method used by many leading companies in the world.

The work reported in this thesis is part of a project to study the temperature rise in a distribution switching cabinet, supported by Pinggao Group Co. Ltd of State Grid Corporation of China. Switching cabinet will therefore be the subject of study in this thesis.

1.2 Literature Review

1.2.1 Switching cabinets

The main function of a switching cabinet in a power system is to change the topology of a circuit and switch on/off the load and clear fault. In other words, it energises or de-energises the power equipment in a part of circuit. Under normal operational conditions, de-energisation allows maintenance or repair work to be done on the power equipment. Under fault conditions, it operates to clear the faults at the downstream of the circuit.

A switching cabinet consists of many components such as the power conducting components which conduct or interrupt the flow of electrical power, i.e. the busbar, switch, circuit breaker and fuse. The other type of components, which link to the control system to monitor, control, and protect the power conducting components, includes the control panel, current transformer, potential transformer, protective relay and associated circuitry. High voltage components use different types of insulating materials and structures depending on individual considerations.

The earliest power stations, before the 20th century, used simple open-knife switches, mounted on insulating panels of marble or asbestos [6]. However, the open-knife switch did not meet the demand of power system development, and manually operating the open-knife switches was too dangerous at higher power levels and rapidly escalated higher voltages. By the early 20th century, the switching cabinet which had a metal enclosure with electrically operated switching element (e.g. circuit-breaker) was designed to de-energise the circuit.

With the technological development of electrical apparatus, the switching cabinets can be operated nowadays safely by automatically controlled circuit breakers under large current and power levels.

1.2.1.1 Switching cabinet under investigation

With the development of electrical apparatus, numerous designs of switching cabinets have been produced since 1920s, when the earliest metal clad switching equipment was resembled. This research project focused on the KYN28-12 switching cabinet for 10 kV distribution power network [7]. It is a metal-clad enclosed switching cabinet accommodating three-phase at a rated voltage of 3.6~12 kV of AC 50/60 Hz for receiving and distributing power energy, and also for circuit control, monitor and protection.

Since this research deals with the steady-state flow and temperature distribution in the switching cabinet, the rated current is needed for calculating the heat sources. For information, the short-time withstand current is the r.m.s. value of the current which the switchgear and control-gear can carry in the closed position during a specified short time, in this case it is a 4-second duration. The rated peak withstand current is equal to 2.5 times the rated short-time withstand current, for a rated frequency of 50Hz. Design wise, a switching cabinet has to pass tests for all three types of current.

Table 1. 1 Parameters of switching cabinet related with heat sources

Item	Unit	Data
Rated current of main busbar	A	630,1250,1600,2000,2500,3150,4000
Rated current of branch busbar	A	630,1250,1600,2000,2500,3150,4000
Rated short-time withstand current (4s)	kA	16,20,25,31.5,40,50
Rated peak withstand current	kA	40,50,63,80,100,125

Within the switching cabinet, the air insulation distance from the vacuum circuit breaker to the enclosure wall is over 125 mm, and the thickness of composite insulation is over 60 mm. It was claimed that these parameters will ensure the circuit breaker to have unique advantages of long life, high reliability, less maintenance and small size.

For the outline dimension, the width of the cabinet is 800 mm when the short-time withstand current is up to 31.5 kA and the rated current of bus-bar is up to 1250 A. The width becomes 1000 mm, when the short-time withstand current is up to 40 kA and the rated current of bus-bar is up to 1250 A. In addition, the depth of the cabinet would be 1500 mm for incoming or outgoing by overhead lines rather than 1300 mm by cables. It is understandable that the size of the cabinet will restrict the air flow within the cabinet hence influence the temperature-rise in the components.

1.2.1.2 Geometry of switching cabinet under investigation

The geometry of the KYN-28 switching cabinet is important for thermal analysis. The enclosure, the metal separating plates of each function unit, the internal structure and all components in the cabinet are shown in Figure 1.1.

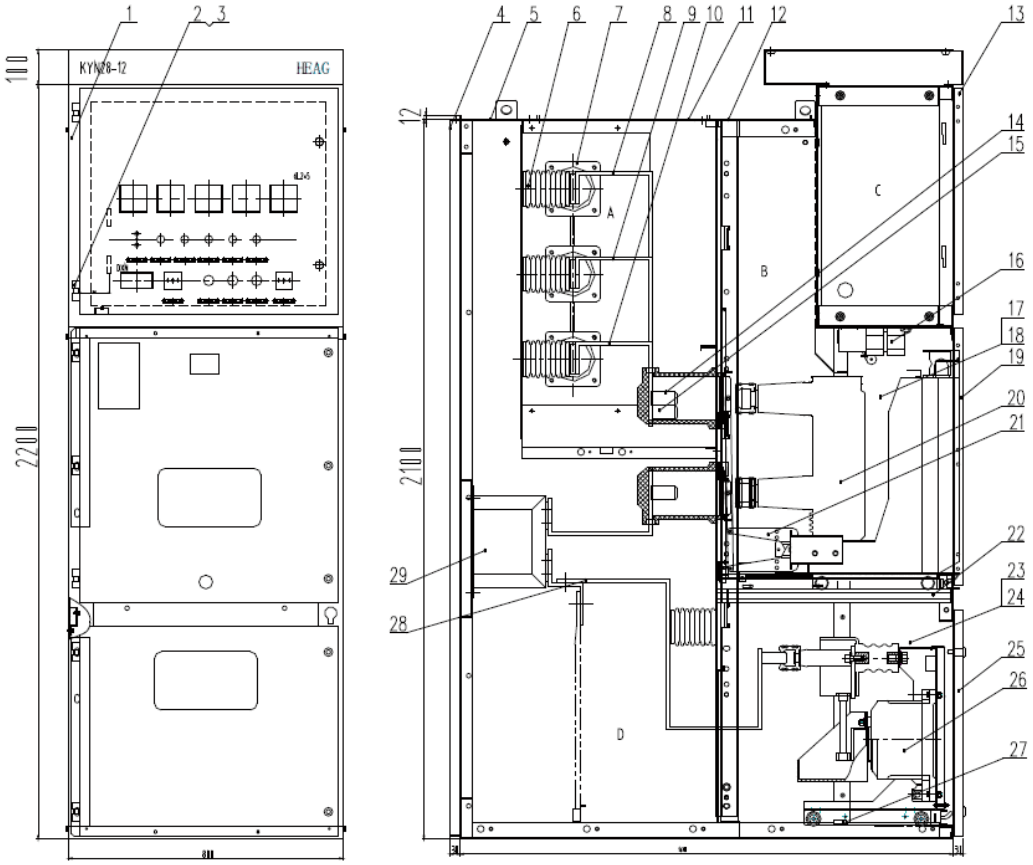

Fig. 1. 1 Structure and components of KYN28-12 switching cabinet

The switching cabinet is divided into four compartments, which are bus-bar compartment (A), circuit breaker compartment (B), instrument compartment (C) and cable compartment (D). In Figure 1.1 components (6) to (13) and (14) to (15) belong to busbar compartment (A), components (16) to (21) belong to circuit breaker compartment (B), instrument compartment is in area C, and components (22) to (29) belong to cable compartment (D).

The components are: (1) Framework, (2) Hinge, (3) Middle hinge, (4) Rear plate, (5) Top cover of cable compartment, (6) Post insulator, (7) Bus-bar bushings, (8) A-phase bus-bar, (9) B-phase bus-bar, (10) C-phase bus-bar, (11) Top cover of bus-bar compartment, (12) Top cover of vacuum circuit breaker compartment, (13) Door of instrument compartment, (14) Contact box, (15) Fixed contact, (16) Fixing plate of

aerial socket, (17) Left plate of vacuum circuit breaker compartment, (18) Right plate of vacuum circuit breaker compartment, (19) Door of vacuum circuit breaker, (20) Vacuum circuit breaker, (21) Interlock & shutter system, (22) Earthing switch interlock, (23) Left plate of cable compartment, (24) Right plate of cable compartment, (25) Door of cable compartment, (26) PT handcart, (27) Earthing busbar, (28) Branch busbar, (29) Current transformer.

It should be noted that the air-cooling device should be added when the current is above 3150 A. This would of course change the air cooling mode from natural convection to forced convection.

1.2.1.3 Busbar Compartment

The main bus-bar connects with the branch bus-bar through fixed contacts, the overlapped part of the busbar is round copper bar with rectangular section as shown in Figure 1.2. In the cabinet, all the bus-bars are covered with heat-shrinking tubes, and the bus-bar is led from one compartment to the other under the supporting insulation bushing.

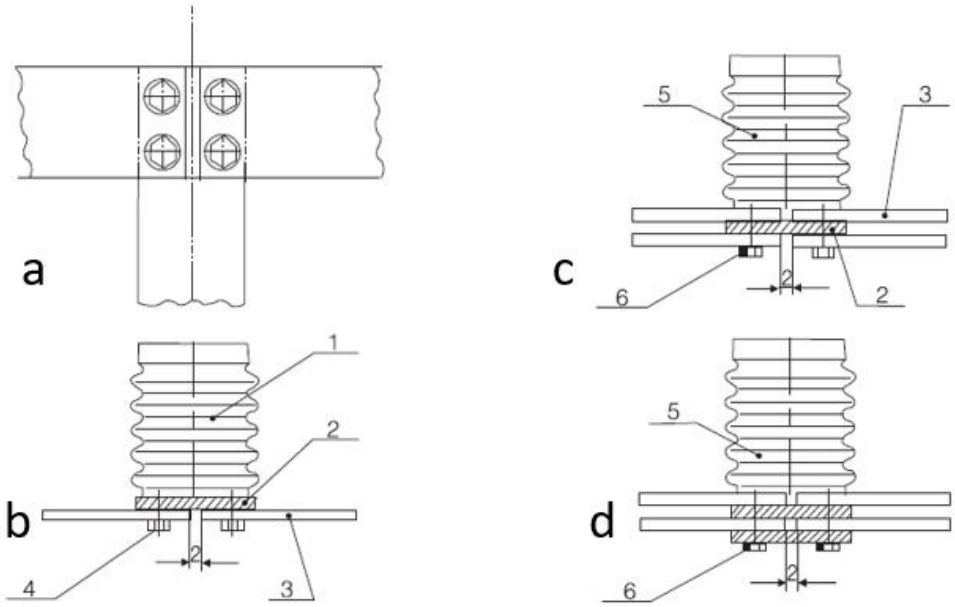

(a) top view of bus-bar junction, (b) side view of junction in single busbar system, (c) side view of junction in single branch busbar system, (d) side view of junction in double branch busbar system

Fig. 1. 2 Configuration of busbar connection, components (1) supporting insulator $\emptyset 130mm$, (2) branch busbar, (3) main busbar, (4) M12 bolt, (5) supporting insulator $\emptyset 145mm$, (6) M16 bolt. [6]

In the switching cabinet, double busbar system is designed for high load current to reduce the Joule loss heating. Moreover, to keep the two branch busbars in the same temperature, the current density is fixed the same. Supporting insulators (1) and (5) are designed to meet the different demands of mechanical strength in busbar compartment.

1.2.1.4 International Standards for Switching Cabinets

The governing international standards for switching cabinet are the IEC standards IEC60694 [8] and IEC60298 [9].

IEC60694 “Common specifications for high voltage switchgear and control-gear standards” is a general standard. The relevant clauses for this research will be

discussed here for various aspects such as the normal and extreme service conditions, the temperature-rise tests and maximum permissible temperature-rise limits for different materials used in a switchgear and control-gear.

Under normal service conditions, the average measured over a period of 24h, and the maximum ambient air temperature should not exceed 40 ℃. The influence of solar radiation up to a level of 1,000 W/m^2 should be considered for an outdoor switchgear and control-gear, and under certain conditions measures to reduce the effect of solar radiation such as roofing or de-rating may be used in order not to exceed the specified temperature-rise. For very hot climates the preferred ranges of minimum and maximum temperature to be specified should be -5 ^oC and +50 ^oC respectively.

For temperature-rise tests, IEC60694 gives a clear guidance on the measurements of ambient air and component temperatures using thermometer and thermocouples, and these tips will be followed in the experimental work of this research.

Most importantly, IEC60694 gives the temperature-rise limits for various parts of the switchgear and control-gear or auxiliary equipment. These limits of temperatures and temperature-rises are re-produced here as shown in Table 1.2. [8]

Table 1. 2 Limits of temperature and temperature-rise for various parts, materials and dielectrics of high-voltage switchgear and control-gear in IEC standard 60694[8]

Nature of the part, of the material and the dielectric	Maximum value	
	Temperature ^oC	Temperature-rise at ambient air temperature not exceeding 40 ^oC K
1 Contact		

Bare-copper or bare copper alloy		
In air	75	35
In SF_6 (Sulphur hexafluoride)	105	65
In oil	80	40
Silver-coated or nickel-coated		
In air	105	65
In SF_6	105	65
In oil	90	50
Tin-coated		
In air	90	50
In SF_6	90	50
In oil	90	50
2 Connection bolted or the equivalent		
Bare-copper or bare copper alloy		
In air	90	50
In SF_6	115	75
In oil	110	60
Silver-coated or nickel-coated		
In air	115	75
In SF_6	115	75
In oil	100	60
Tin-coated		
In air	105	65
In SF_6	105	65
In oil	100	60
3 All other contacts or connections made of bare metals or coated with other materials	(See point 7)	(See point 7)
4 Terminals for the connection to external conduction by screws or bolts		
Bare	90	50
Silver, nickel or tin-coated	105	65
Other coatings	(see point 7)	(see point 7)
5 Oil for oil switching devices	90	50
6 Metal parts acting as springs	(see point 11)	(see point 11)
7 Materials used as insulation and metal parts in contact with insulation of the following classes (see point 12)		
Y	90	50
A	105	65
E	120	80
B	130	90
F	155	115

Enamel oil base Synthetic H C other insulator material	100 120 180 (see point 13)	60 80 140 (see point 13)
8 Any part of metal or of insulating material in contact with oil, except contacts	100	60
9 Accessible parts Excepted to be touched in normal operation Which need not to be touched in normal operation	70 80	30 40
NOTE The points referred to Section 4.4.3 in IEC standard 60694 Point 7 When materials other than those given in the table are used, their properties shall be considered, notably in order to determine the maximum permissible temperature-rise. Point 11 The temperature shall not reach a value where the elasticity of the material is impaired. Point 12 Classes of insulating materials are those given IEC 60085. Point 13 Limited only by the requirement not to cause any damage to surrounding parts.		

IEC60298 is specifically for “AC metal-enclosed switchgear and control-gear for rated voltage above 1 kV and up to and including 52 kV”. The most relevant chapters and sections to the researched thermal topic are IEC 60298 Section 4.4 “Rated normal current and temperature-rise”, Chapter 5 “Rules for design and construction”, Section 6.3 “Temperature-rise tests”, and Annex BB “Method of calculating the cross-sectional area of bare conductors with regard to thermal stresses due to currents of short duration”.

In IEC 60298 Section 4.4, it is stated that the temperature-rise for accessible enclosures and covers shall not exceed 30 K.

In IEC 60298 Chapter 5, clause 5.102.6 stated that “Ventilating openings and vent outlets shall be so arranged in such a way that gas or vapor escaping under pressure does not endanger the operator”, which indicates that the design not only needs to

consider thermal issue e.g. using forced convection to further cool the internal temperature, but also other factors such as safety.

In IEC 60298 Section 6.3, among many addition supplements to the specification of "Temperature-rise tests" of the main standard IEC60694, one of the most relevant statement is that "the temperature-rise of the different components shall be referred to the ambient air temperature outside the enclosure", and "if the ambient air temperature is not constant, the surface temperature of an identical enclosure may be taken under the same ambient conditions". This clause is particularly helpful for this research, for it provides the proof that people can use the measured enclosure surface temperatures from the experimental work to set the boundary conditions in the initial simulation studies for natural convection cases, as described later on in chapter 2 of this thesis.

In IEC Standard 60298 Annex BB, an important empirical formula is given to calculate the cross-sectional area of bare conductors with regard to thermal stresses due to currents of short duration in the order of 0.2 s to 5 s.

$$S = \frac{I}{\alpha}\sqrt{\frac{t}{\Delta\theta}} \qquad (1\text{-}1)$$

Where S is the cross-section, expressed in square milli-meter (mm^2), I is the r.m.s (A), value of current in amperes, α has the following values: 13 for copper; 8.5 for aluminium; 4.5 for iron; and 2.5 for lead; t is the time, expressed in seconds, Δθ is the temperature-rise (K), expressed in Kelvins, for bare conductors, it is normally 180 K [8].

If the time is more than 2 s but less than 5 s, the value for Δθ may be increased in the same formula to 215 K [8].

This takes account of the fact that the temperature-rise is not strictly adiabatic.

1.2.2 Modern approaches for thermal analysis

An introduction of computer modelling approach for a complex thermal network was given by Mellor in 1991 [10]. Since then, thermal-network modelling and analysis has been used by many researchers in thermal analysis of electrical machines, for both steady-state and transient cases [3, 10-12]. In recent years, thermal analysis of electric motors has received more attention than any other electrical devices, as the thermal design aspect especially for small- or medium- sized motors was in the past superficially dealt with by specifying empirically a limiting value of current density. The modelling approaches for thermal analysis can be generally divided into two basic types, analytical lumped-circuit method and numerical method [13], and these two categories are also applicable for the models developed for any other electrical apparatus.

1.2.2.1 Lumped-parameter thermal network

The lumped-parameter thermal network (LPTN) model is also widely known as the lumped-circuit method, which allows to lump a group of components together as having the same temperature and then to represent them as a single node, in thermal analysis. Due to this, nodes separated by different temperatures can be built together to define a new circuit to describe the heat transfer process in the whole domain.

In terms of analytical lumped-circuit method, there are several advantages such as less model complexity and time saving. LPTN is particularly effective for sensitivity study when a large number of scenarios are accounted for. A parameter sensitivity analysis of thermal network is performed in [14]. As reported in [13], much more detailed thermal and flow networks can be solved in a fast speed, including a high number of thermal and flow elements, with the advance of computational capability.

In [15], both natural convection and forced convection situations are taken into consideration for the induction motors, using the lumped-parameter network method. A comprehensive set of formulations in [16] to describe the heat transfer in electric machines are developed for the lumped-parameter thermal network, and these formulations of convection heat transfer and flow resistance can be used for similarly shaped geometries with different sizes. In other words, the LPTN method and relevant formulations in [16] can be considered as a reference to calculate the convection and flow in electrical machines.

This lumped thermal network method can be divided into two main processes: heat transfer and flow-network studies. To make sure that the heat transfer and flow paths can accurately reflect the reality, the user needs to invest efforts in defining key thermal parameters for calculating thermal resistances representing conduction, convection and radiation, as shown in equation (1-2) to (1-4):

Conductive thermal resistance can be calculated as:

$$R_{conduction} = \frac{L}{kA} \tag{1- 2}$$

where $R_{conduction}$ (K⁄W) is conductive thermal resistance, L (m) is the path length, A (m^2) is the cross section, and k (W⁄(m·K)) is the thermal conductivity of the material

Radiative thermal resistance can be calculated as:

$$R_{radiation} = \frac{1}{h_R A} \tag{1- 3}$$

$$h_R = \sigma_{Stefan-Boltzmann} \cdot \varepsilon \cdot F_{1-2} \frac{({T_1}^4 - {T_2}^4)}{(T_1 - T_2)} \tag{1- 4}$$

where $R_{radiation}$ (K⁄W) is radiative thermal resistance, A (m^2) is the surface area and h_R (W⁄(m^2·K)) is the heat-transfer coefficient, $\sigma_{Stefan-Boltzmann}$ is Stefan-Boltzmann constant as 5.669×10^{-8} (W⁄(m^2·K^4)), ε is the emissivity of the surface, F_{1-2} is the view

factor for dissipating surface 1 to the absorbing surface 2 (the ambient temperature for external radiation), and T_1 (K) and T_2 (K) are the temperature of surface 1 and 2 respectively.

Convective thermal resistance can be calculated as：

$$R_{convection} = \frac{1}{hA} \tag{1-5}$$

where $R_{convection}$ (K⁄W) is convective thermal resistance, A (m^2) is the surface area and h is convection-heat-transfer coefficient (W⁄(m^2·K)).

In these equations above, there are some parameters difficult to define accurately, i.e. radiated emissivity and view factor in radiation. Also, some parameters such as convection-heat-transfer coefficient are dependent on empirical formulations from available literature. For the above reasons, the degree of error is sometimes quite high between experimental values and thermal network simulation results. In [17], it is reported that the temperature predicted by the lumped-parameter method is as large as 10% of the measured value.

For some practical cases, the thermal-flow field is too complex to be described by simple nodes. LPTN is consequently not a suitable tool to solve the problem and the numerical method needs to be employed instead.

1.2.2.2 Numerical method

The main strength of numerical analysis method, which is also called Computational Fluid Dynamics, is that any complex geometry can be modelled. Therefore, the flow field can be described in detail in a complex geometry. However, this method requires a high demand of computer speed with large memory capacity and it is very time consuming. To solve the differential governing equations in CFD software, different

discretization methods have been studied, such as finite volume method (FVM), finite element method (FEM) and finite difference method (FDM).

In fact, CFD needs a long “pre-processing” time, which means that the more complex model requires more time to create the geometry model first and then more calculation time for the results. All the discretization methods require to firstly subdivide the whole domain of physical process into small and single parts, called finite elements, and then to assemble the solution of each element into a large system to describe the entire and complex physical process. The method FEM is widely used for the calculation of electromagnetic field, and this approach is available together with numerical thermal analysis to solve heat management issue in electrical machines, where electromagnetic field is closely coupled with thermal-flow field. In [18], the temperature variation and electromagnetic flied in a three-phase bus-bar model was solved, and the simulation results show a good agreement with the experimental data. Similar work can be found in [19, 20].

Computational Fluid Dynamics is used to numerically solve and analyse the fluid flow problem. The main advantage of the CFD approach is that it can predict the flow field in a complex geometry and therefore the thermal-flow field can be analysed in detail. CFD is the most widely used method to obtain the result of heat transfer calculation, due to the development of supercomputers and friendly CFD software.

In light of the above, the thermal solution module of the FEM package can be extended by CFD. This essential extension is referenced as conjugate heat-transfer modelling, which is introduced and used in [21].

1.2.3 Modelling switching cabinets

There has been limited work done for the thermal analysis in switching cabinet as compared with the thermal modelling for motors. To enable high accuracy of

simulation results and good spatial resolution, the numerical models developed so far were mostly focused on the key component or the hot spots in the cabinet. Out of references [7, 18, 22-24], only [7] obtained a complete model of switching cabinet and calculated the thermal-flow filed inside it.

In [22], a very simple cooper wire model has been built in COMSOL Multiphysics to simulate bad contact and the temperature distribution in contact area was described. The cooper material interface at the contact area can become fatigue or fractured under elevated temperature where extra contact resistance in the current loop generates excessive heat. The authors used a combination of theoretical and numerical simulation methods to identify the range of temperature variation. A formula for describing contact resistance in an electrical-thermal coupled field in COMSOL was introduced.

For [23] and [18], models based on the geometry of busbar of GIS were developed to calculate the thermal-flow field coupled with magnetic field, due to a high rated AC current level of 3150 A. In the GIS cylindrical enclosure, a balanced three phase bus-bars were arranged symmetrically and the SF6 gas is in natural convection mode. The hottest spot inside the GIS were calculated as 63.6 ℃, which is very close to the measured temperature of 71.1 ℃. In addition, the simulated thermal distribution results were validated by the experimental data.

As one of the important components in switching cabinet, the circuit breaker was taken in to consideration in [24]. A detailed three-dimensional model was built to describe the complex structure of circuit breaker, including metal contact finger and insulating cover. Natural convection is simulated and the simulation results were validated by the experimental results, and the simulated temperature results provided evidence on where the hottest area is in the circuit breaker. [24] also gave the strategy for the simplification of the simulation model.

Work has been done in calculating the thermal-flow field in a complete geometry of switching cabinet (KYN28A-12) in [7]. A numerical model, using finite volume method, was built to solve a set of differential equations under turbulent flow condition. The author adopted the wall function method instead of using numerous refined mesh cells, to enable the computation of convection heat transfer within limited time and computer storage. In this paper, although the hottest spot and air flow direction are studied, the simulation results have not been validated by the experiments.

1.3 Motivation

As we all know, CFD aided simulation is widely used to predict the thermal behaviour inside the apparatus when designing a new structure of power apparatus. Yet it seems that limited work can be found on modelling the thermal processes of switching cabinets, i.e. the metal-clad enclosed medium voltage electrical apparatus cooled by air.

Switching cabinet, as important electrical apparatus for controlling and monitoring the power flow in distribution network systems, has a great number of components and numerous bolts. The sheer size of the whole cabinet requires a fast computer with numerous memory to model it in a numerical way. However, it is not possible to simulate the whole structure of the cabinet in the University of Liverpool due to the limitation of super computer.

Luckily, there are four compartments in a switching cabinet, and each individual compartment is independent with a minor thermal effect on the other compartments [2]. Therefore, based on the switching cabinet design, the one-year MPhil study is only focused on the busbar compartment. In the real busbar compartment, there are three-phase busbars, however only one phase busbar is modelled in this research when considering the experimental setup. This is due to the consideration of reduce the structural complexity in experimental setup but maintain the research of key

issues. Our busbar compartment model includes busbars and the busbar joint, and take all the important factors into consideration, i.e. the maximum temperature and air flow field.

The research aims at processing the basic modelling principle for one compartment. Once the simulation results are successfully validated by the experimental results, then the whole cabinet can be modelled in the same way, to help the industry to understand how air flows inside the cabinet and how to optimise the heat transfer process.

In this thesis, there are a number of key issues that have been tackled：

- to develop an experimental busbar compartment model;
- to identify the devices for the experimental setup and to develop relevant strategies for temperature and electrical resistance measurement;
- to build a CFD model with the coupled electrical and thermal-flow field in COMSOL;
- to conduct a convergent simulation to accurately predict the maximum temperature and the thermal-flow field;
- to compare simulation results with experimental results for verification.

Once the modelling principle is proved to be correct, a model for calculating the electric current distribution inside the conductors coupled with heat transfer, is used to predict the temperature variation for different loading and environment conditions. The temperature distribution inside the switching cabinet can also be predicted.

With this knowledge, designers would be able to find the optimal solution to manage the heat inside the cabinet and the temperature of each component. Hence the lifetime of insulation can be properly managed, and the thermal runaway failure can be reduced as well. Moreover, when the large-size switching or control gear is in its normal working condition, it is difficult to measure the temperature inside the

enclosure, even placing some small-size sensors like thermocouple. An accurate prediction of temperatures on the cabinet wall and inside, using such a model to simulate thermal transient process, could also help monitor the thermal behaviour of electrical devices under normal working condition.

1.4 Outline of the thesis

This thesis aims to study the complex phenomena of the thermal-flow field in a simplified geometry. The generalised methodology through this study is aimed to be applicable for the industrial application of optimizing design of switching cabinet. The thermal fluid model has been built by using a numerical platform provided by COMSOL (CFD commercial software). The simulation results have been validated by the experiments which were conducted during this MPhil study.

The project background, motivation and thermal modelling approach are given in Chapter 1. A literature review on switching cabinet and thermal analysis method is also introduced.

Chapter 2 discusses the mathematical equations used to describe the thermal processes and how to build a numerical model to predict the temperature variation and obtain an accurate thermal-flow field. The heat generating and dissipating processes are analysed. The key issues in numerical solving thermal-flow field are also introduced.

Chapter 3 is focused on the experimental design of the busbar compartment model and the measurement plan. The relevant international standards are studied and referred to. The experimental tests are designed to be used in Chapter 5 to validate the numerical solutions.

As the contact resistance generates more heat and makes the contact area the hottest spots in the entire system, the calculation of contact resistance becomes

vitally important for predicting the maximum temperature. Therefore, in Chapter 4, a widely used contact resistance model is validated by experiments, and the parameters from previous empirical formulas are re-evaluated to better suit our study objects.

The main content of Chapter 5 is the numerical solution process in CFD software COMSOL. The results of the simulation models with different boundary conditions are compared and analysed, and a suitable boundary condition is then determined. Then the simulation results of models using this boundary condition are compared with the experimental results under different load currents, and reasonable agreement is shown between simulations and experiments.

Finally conclusions are given in Chapter 6. A guide for further work is also intended in this chapter.

Chapter 2 Simulation Methodology

As all known, too much heat generated in electrical devices, if not dissipated appropriately, would not only decrease the mechanical strength of metal material, but also deteriorate the insulation material. In the light of above, the temperature-rise of each different kind of electrical apparatus must be ensured to comply with the relevant standards for normal operating condition. For electrical devices such as transformers and switching cabinets, not only the temperature distribution but also the flow field inside the device need to be studied to control the temperature, and optimize the cooling device for the design of these devices.

Compared to the experimental method to predict the maximum operating temperature of an electrical device, the computational method, which is based on mathematical models, is more advantageous in terms of cost and time efficiency. It is also easier to change the geometry of the device at the design stage. To obtain accurate results from numerical simulation, a suitable mathematical description should be developed or chosen first. Then the governing equations is solved by numerical calculation at the next stage. The numerical method used in this project is the so called finite element method, which divides the whole calculating domain into small cells. With respect to the accuracy of the model required and the limitation of modern computer, the crucial area, where the occurrence of energy transfer is the most in the equipment, needs to be identified and solved with enough spatial resolution. This area is also called vital area in our simulation. However, different ways to set the boundary condition would re-define the crucial area for the numerical solution. Therefore, in section 2.4 and 2.5, different boundary conditions for the calculating domain, vital boundary layer area and mesh strategies, these key points to ensure the accuracy of numerical calculation process are introduced.

Chapter 2 is focused on the development of the mathematical model for thermal-flow field, the relevant governing equations are explained here and the issues in numerical calculations are also discussed. The simulation CFD modelling and processes of building the simulation model are shown in the following flow chart given in Figure 2.1.

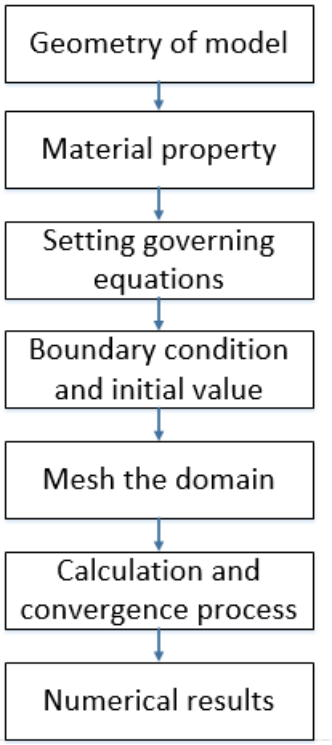

Fig. 2. 1 CFD modelling and simulation process

2.1 Mathematical models

To study the thermal-flow field in electrical devices, two processes need to be taken into consideration, i.e. heat generation process and heat dissipation process. In most electrical devices, the heat is generated by Joule loss which is caused by the electrical resistance and contact resistance of conductor and conductor joint, whilst the heat dissipation consists of three processes, i.e. conduction, convection and radiation. The heat transferred in the solid conductor is by conduction, however the heat generated

from conductor would be mainly transferred into its surrounding area by conduction and radiation inside the device. The heat transferred into the fluid, either a gas or a liquid, would then be dissipated through convection. To describe the convection process in the flow field, Navier-stokes equations are used, which are based on the law of conservation of energy, momentum and mass.

There are two basic forms of heat transfer, i.e. steady-state condition and transient condition. The differences between these two conditions are dependent on whether the temperature-rise in an individual object changes or continues to change. The temperature-rise of any electrical device would reach a stable value after a certain time when the quantity of heat produced inside the device is equal to the heat dissipated to the outside environment. At this time, the electrical device is called to reach its steady-state heat transfer condition, which also means that it reaches the maximum temperature-rise at its normal working condition. Prior to this time, the device is thermally in the transient condition. In this project, this maximum temperature-rise is important and needs to be predicted for the switching cabinet. Hence, the steady-state condition is the main consideration in the thesis.

2.1.1 Heat source

In most electrical apparatus, there are two types of electrical resistances which could produce Joule heating, conductor resistance and contact resistance.

For the conductor resistance, the heat generated in a current loop is calculated in equation (2-1) to (2-3) as:

$$\nabla \cdot (\sigma \nabla V) = 0 \tag{2-1}$$

$$E = -\nabla V \tag{2-2}$$

$$Q = \sigma E^2 \tag{2-3}$$

where σ (S/m) is the electrical conductivity, V (V) is electrical potential difference of the conductor, E (V/m) is the electrical filed, Q (W/m^3) is the Joule loss heating. To describe the electrical field and the associated Ohmic heating as the heat source in commercial CFD software (COMSOL), the current conducting process is described by the equation of current continuity. The electrical field is produced by a stable current source. The AC current source of r.m.s value is added to the two ends of the conductors.

The conductor in electrical apparatus is made by metal materials, of which the electrical resistance changes with temperature. This means that the value of electrical resistance is increased with the Joule loss heating. The factor, i.e. resistivity temperature coefficient, is used to describe the rate of resistance change with temperature.

To obtain an accurate result of mathematical model, the value of temperature resistivity coefficient must be defined. In this project, the solid conductor is made of copper, and the dependence between the electrical conductivity of copper and temperature is shown in the equation (2-4) [25]:

$$\sigma_T = \frac{1}{\rho_{ref}(1+\alpha(T-T_{ref}))} \tag{2-4}$$

Where: σ_T (S/m) is the electrical conductivity of the conductor at individual temperature T (K), ρ_{ref} (Ω·m) is the electrical resistivity of copper at reference temperature T_{ref} (K), which is usually set as 20 °C (273 K), and α is the temperature resistivity coefficient of copper.

α is referred as 0.0039 for copper busbar conductor in [26]. To ensure the correctness of this value (0.0039), validating experiment was carried out in section 4.3.1.

The other heat source is produced by contact resistance at the conductor joint. In large electrical devices, different conductors need to be connected and they can be connected using bolts or being braised together. As reported in [27], if the two bodies touch each other, the highest asperities comes into contact first and contact takes place only at a few spots, which are randomly distribution over the contact interface. Therefore, each of these contacting ways could not make the whole overlapping area to carry the current flow evenly, this means the current flow only passes through certain spots in the whole contact area or part of the area. The microstructure of the contact surface is shown in Figure 2.2 [28]:

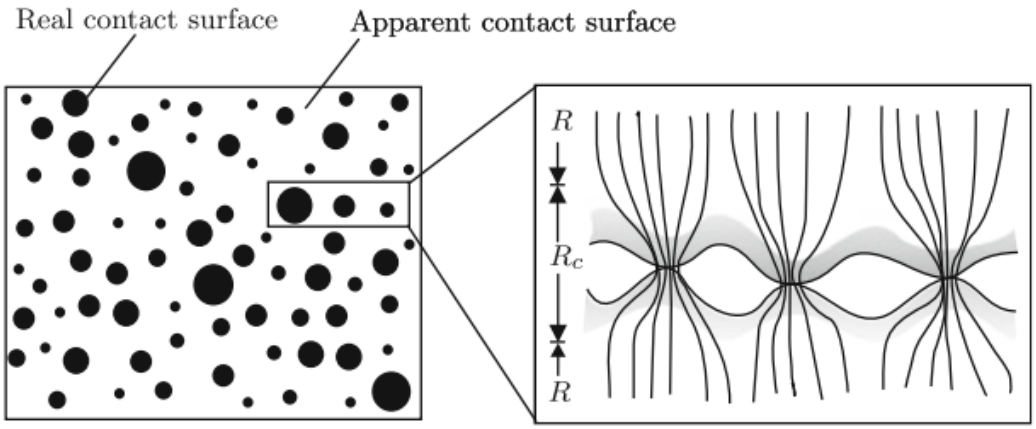

Fig. 2. 2 Microstructure of contact area [28]

In Figure 2.2, the left picture is the top view of the microstructure of contact surface. In the whole apparent contact surface, only a few number of the black spots, normally called real contact surface or A spots, are the effective area, which could pass the current flow. The right picture is the side view of contact surface, R represents normal electrical resistance where the current flow passes in overlapped area, whilst Rc is the area where current flow passes the A spots, and the current flow there is distorted. These A spots make the current density across the contact area much larger

than that of conductor. Due to this, the contact area of the conductor is always the hottest area in switching cabinet.

Literature [28] has been dedicated to the research of contact resistance R_c in Figure 2.2. The basic concept of contact resistance was provided by Holm in 1931 [28, 29], and the contact resistance consists of constriction resistance and film resistance. The constriction resistance is dominated when the contact force is high as reported in [30]. Moreover, when interface becomes electrical conductive, meaning metal to metal contact spots ('a-spots') are produced, the film resistances are ruptured [31]. Therefore, the constriction resistance is only taken into consideration in this thesis.

It was found that the constriction resistance can be affected by three main factors, i.e. temperature, contact pressure and surface roughness. The value of contact resistance is dependent on the electrical resistivity of the conductor, which is of course temperature dependent. In [32] and [33], they proved the linear relationship between contact resistance and temperature-rise, as the same thermal and electrical behaviour to pure metal conductor. Their results were proved by both experimental and simulation methods. As for contact pressure and surface roughness, smooth surface and sufficient pressure could increase the amount of 'spot A' in Figure 2.2, which could increase the area of current path and therefore reduce the contact resistance. It was reported in [29, 34] that contact resistance versus contact pressure is exponential in different contact shapes and with different metal materials.

The heat dissipation in the contact surface was managed by conduction, convection and radiation. In [35], thermal radiation across the interfacial gaps is generally considered as insignificant as long as the surface temperature is less than approximately 700 K. For convection process, natural convection is generally neglected as a heat transfer mode within the interfacial gaps due to the fact that the small thickness of interfacial gaps (typically less than 10 μm) [36].Therefore, for this

thesis, the heat dissipation process of contact resistance is only by thermal conduction.

In light of above, the Cooper-Mikic-Yovanovich model developed in [35, 37, 38], which is generally regarded as an accurate model and widely used for calculating contact resistance, is chosen in this project to describe the contact resistance. It describes the influence of temperature, contact pressure and surface roughness, as shown in equations (2-5) to (2-8) below:

$$J = h_c(\varphi_2 - \varphi_1) \tag{2-5}$$

$$h_c = 1.25\sigma_{contact}\frac{m_{asp}}{\sigma_{asp}}\left(\frac{p}{H_c}\right)^{0.95} \tag{2-6}$$

$$\frac{2}{\sigma_{contact}} = \frac{1}{(\sigma_1 n_d)\cdot n_d} + \frac{1}{(\sigma_2 n_d)\cdot n_d} \tag{2-7}$$

$$Q_{contact} = J \cdot (\varphi_2 - \varphi_1) \cdot A \tag{2-8}$$

Where: J (A/m^2) is the nominal current density across the contact area, h_c (S/m^2) is called as constriction conductance, φ_2 (V) is the higher voltage potential of contact surface, φ_1 (V) is the lower voltage potential of contact surface, $\sigma_{contact}$ (S/m) is the electrical conductivity in contact surface, m_{asp} is the average slope of the microscopic asperities, σ_{asp} (m) is the average height of the microscopic asperities, H_c (P_a) is the reference micro-hardness, always set as 3 GP_a, p (P_a) is the contact pressure applied on the surface, σ_1 (S/m) is the conductivity of one of the contact materials, σ_2 (S/m) is the conductivity of the other contact material, n_d is the unit vector , $Q_{contact}$ (W) is the heat generated by contact resistance, and A (m^2) is the area of contact surface.

The Cooper-Mikic- Yovanovich model is short named as the C-M-Y model in this thesis later on, it includes all the effects caused by temperature, pressure and surface roughness on the contact resistance. The number of A spots in contact area are

defined by parameter m_{asp} and σ_{asp} shown in Figure 2.3. To validate the empirical parameters in this model, relevant experiments were carried out in section 4.3.2.

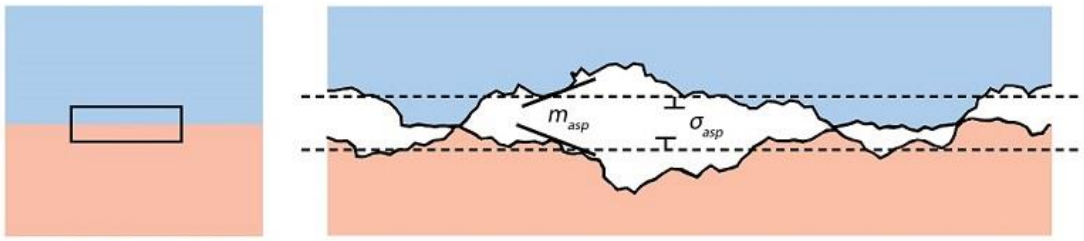

Fig. 2. 3 Configuration of factors m_{asp} and σ_{asp} [38]

2.1.2 Heat transfer

To reach the equilibrium state in thermal-flow field, the quantity of heat generated must be equal to the heat dissipated. The dissipation process consists of conduction, convection and radiation. Therefore, in this section, these three processes, relevant theories and equations are introduced.

2.1.2.1 Thermal conduction

Conduction is one of the main heat transfer processes, which is caused by the temperature difference between two bodies. Due to the temperature difference, microscopic particles, such as molecules, atoms and electrons, are forced into movement and collision, thus the kinetic and potential energy of the bodies will be changed, which re-organise the temperature distribution in these bodies. As heat is transferred by these microscopic particles, the thermal conduction could take place in all phases of matter, such as solid, liquid and fluid. The law of heat conduction (Fourier law of conduction), which is proposed by French scientist Joseph Fourier [39], states that the conduction heat flux rate is proportional to the temperature gradient in the material body (as shown in Figure. 2.4), and relevant equation is given as:

$$q = -k\nabla T \tag{2- 9}$$

Where q (W/m^2) is the local heat flux, k (W/(m·K)) is the thermal conductivity of material, ∇T (K/m) is the temperature gradient.

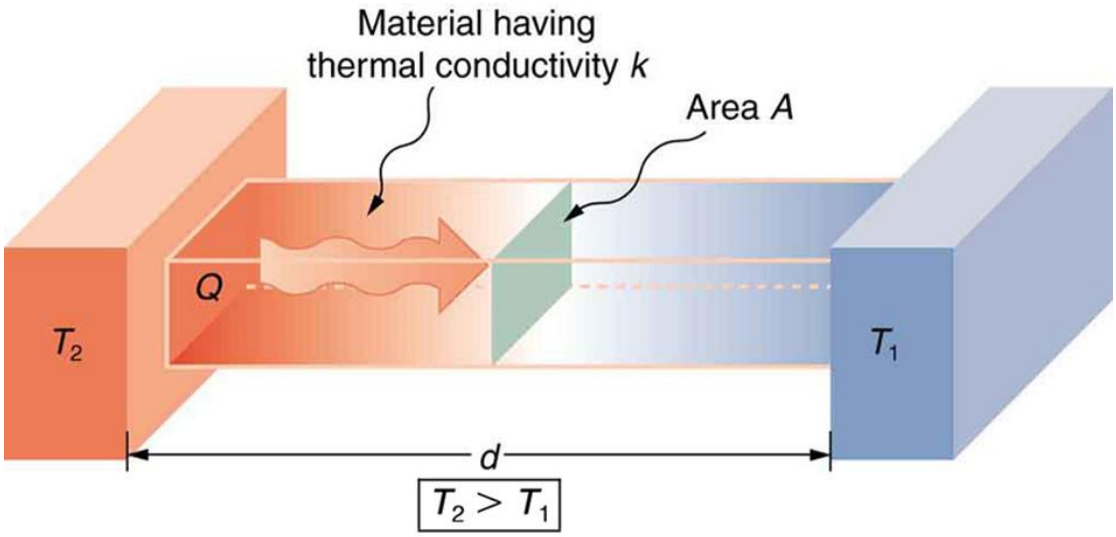

Fig. 2. 4 Thermal conduction [39]

2.1.2.2 Thermal convection

Convection is shown in Figure 2.5, heat transferred from one place to another by the movement of fluids. It is usually the dominant form of heat transfer in fluid or gas.

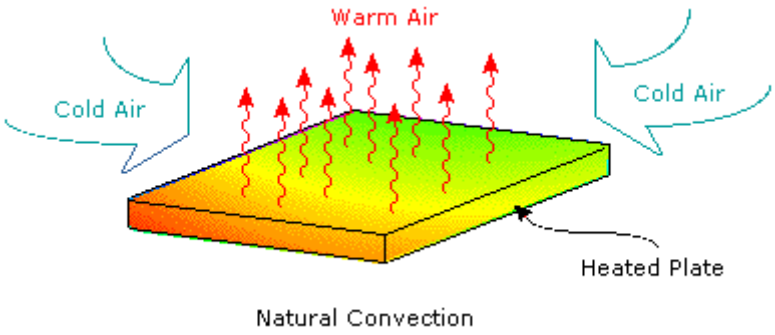

Fig. 2. 5 Thermal convection [40]

For the small-size electrical devices, the temperature of solid heat source is always focused. In Figure 2.5, the velocity of fluid flow right on the surface of heated plate (so called wall in a thermal-flow field) is zero, and the heat is transferred from the solid surface to fluid flow is by thermal conduction. However, the temperature gradient of fluid flow near the wall is dependent on the vertical flow rate at which the fluid carries the heat away, and a higher velocity right above the heat plate produces a larger temperature gradient. Therefore, the temperature gradient at the wall depends on the flow field, a suitable expression is developed to describe the overall processes, as Newton's law of cooling.

Newton's law of cooling states that the rate of heat loss of a body is proportional to the difference in temperatures between the body and its surroundings, as given in equation (2-10):

$$q = h(T - T_{amb}) \tag{2- 10}$$

*w*here q (W/m^2) is the heat-transfer rate of convection, h (W/(m^2·K)) is the heat transfer coefficient, T (K) is the temperature of the surface, T_{amb} (K) is the temperature of the ambient.

Heat transfer coefficient (h) is dependent on heat transfer modes, fluid types, flow regimes and thermohydraulic conditions [40] from the experiment and empirical

formula. Therefore, Newton's cooling law always applies when the heat transfer coefficient is independent of temperature difference between solid body and environment, such as small-size electronic device in natural air flow. In large-size electrical apparatus, the heat transfer coefficient would change with the variation of temperature, pressure and velocity of fluid. Newton's cooling law cannot meet the demand of an accurate thermal-flow field study, which needs the velocity and flow direction in every point inside the apparatus.

To obtain the flow field in large-size electrical devices, Navier-Stokes equations are studied and solved, which are deduced from the conservation law of mass, momentum and energy, in the general analytical format as given in equation (2-11):

$$\frac{\partial(\rho\emptyset)}{\partial t} + div(\rho V\emptyset) = div(\Gamma \mathrm{grad}\emptyset) + S \qquad (2\text{-}11)$$

Where $\emptyset$ are the generic variables of either temperature, velocity or pressure, V is the velocity vector, Γ ($(N\cdot s)/m^2$) is the coefficient of diffusion. S (W) is the heat source.

2.1.2.3 Thermal radiation

Thermal radiation is the emission of electromagnetic waves from all the matters that have a temperature greater than absolute zero. It represents a conversion of thermal energy into electromagnetic energy. Thermal energy consists of the kinetic energy of random movements of atoms and molecules. Under the condition with a high temperature, particles that have kinetic energy would interact with each other. This interaction results in the electrodynamics generation of coupled electric and magnetic fields, emission of photons, radiating energy away from the body through its surface boundary.

The characteristics of thermal radiation depend on various properties of the material it is emitting from, including its temperature, its spectral absorptivity and spectral

emissivity, as expressed by Kirchhoff's law [40]. This means that most of the hot bodies would absorb the energy from the environment and at the same time emit energy by radiation. If the radiating body and its surface are in thermodynamic equilibrium and the surface has perfect absorptivity at all wavelengths, it is characterized as a black body. A black body is also a perfect emitter. The radiation of such perfect emitters is called black-body radiation. However, most of the bodies cannot act like black-body, so an emissivity factor ε, which is calculated as the ratio of any body's emission relative to that of a black body, is defined to describe the emissive effect of individual body. Considering the effect of surrounding environment, the power emitted from hot surface to environment is calculated in equation (2-12):

$$P = \varepsilon \cdot \sigma_{Stefan-Boltzmann} \cdot (T^4 - {T_{amb}}^4) \qquad (2\text{-}12)$$

Where P (W/m^2) is the power lost by radiation, ε is emissivity factor, $\sigma_{Stefan\text{-}Boltzmann}$ ($W/(m^2 \cdot K^4)$) is the Stefan-Boltzmann constant as 5.670373×10^{-8}, T (K) is the temperature of surface, T_{amb} (K) is the temperature of ambient.

2. 2 Model geometry and material property

When developing a computer simulation model in commercial software, the geometry of the simulated object is built first and its material property is inputted to define the object one by one, and then the components of this simulated system are constructed. To simplify the numerical calculation procedure and reduce the computational time, symmetric geometry is taken advantage of, and only a half of the system is built in the computer model. Whilst the geometry of our model is based on the busbar compartment of KYN28 switching cabinet, there are still some essential modifications to the geometry of the computer model to help simplify the numerical calculation and aid fast convergence.

The modifications have been done in two different aspects, i.e. the connecting bolts between two busbars and the thickness of the solid enclosure wall.

2.2.1 Bolt connection

In large switching or control gears, the bolt connection is one of the most common ways to connect the overlapped busbars. The function of these bolts is to provide a stable contact pressure applied on the contact surface. Since the current is not through the bolts, and it is time consuming to draw the bolts in the computer model, so very early on the project work a decision was made that the bolts are just simply ignored in the geometry drawing. However, the pressure produced by the bolts is still added on contact surfaces in CFD models. Neglecting the bolts might affect the air flow around the contact area, and this could be a shortcoming of this thesis.

In this project, the bolts used in the experimental work are M24 bolt. The dimension of a M24 bolt is given in Figure 2.6:

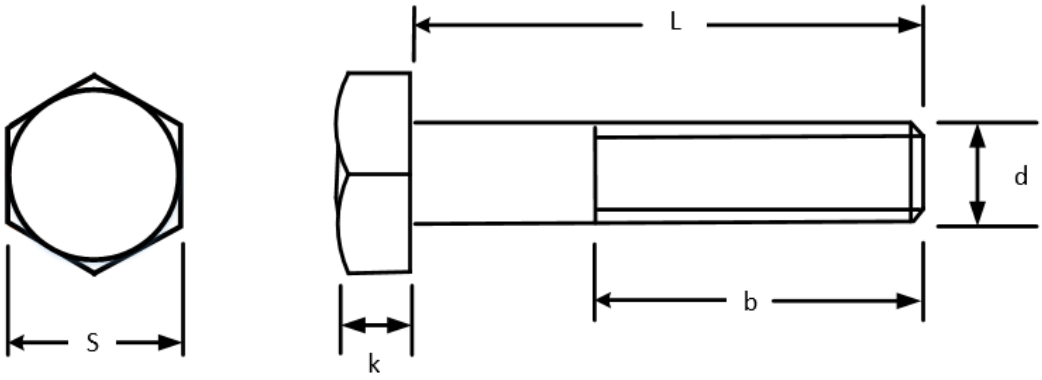

Fig. 2. 6 Dimensional parameters of M24 bolt

where s is the width across the flats as 40 mm, k is height of bolt head as 15 mm, L is the length of bolt as 125 mm, b is thread length of bolt as 44 mm, and d is body diameter as 24 mm.

2.2.2 Thickness of solid enclosure

In reality, the heat is generated in busbar and then transferred to the air inside the enclosure, the energy is taken and transferred by convection of air flow inside the enclosure, whilst conduction and radiation are caused by the solid enclosure wall to the ambient. In numerical solution, the most difficult problem is the coupled process from the solid wall to the surrounding ambient fluid when obtaining a convergent result.

Considering the geometry and material property of solid enclosure wall, the thickness of the solid enclosure wall is much less as compared to the height and width of the busbar compartment model, as 1 cm to 30 cm respectively. Moreover, the temperature of the inner surface of solid enclosure wall would be different from that of the outer surface.

In light of the above, the heat transfer process in the solid enclosure wall can be neglected, which dramatically reduces the difficulty in the model convergence process. Therefore, the geometry of solid enclosure wall is simplified as plate without thickness in our case.

2.2.3 Mirror symmetric geometry

Considering the geometry of real busbar compartment and experimental setup in Chapter 3, the geometry of our busbar compartment model is drawn as a single phase overlapped busbar placed in a transparent Perspex enclosure, its geometry is drawn in COMSOL as shown in Figure 2.7:

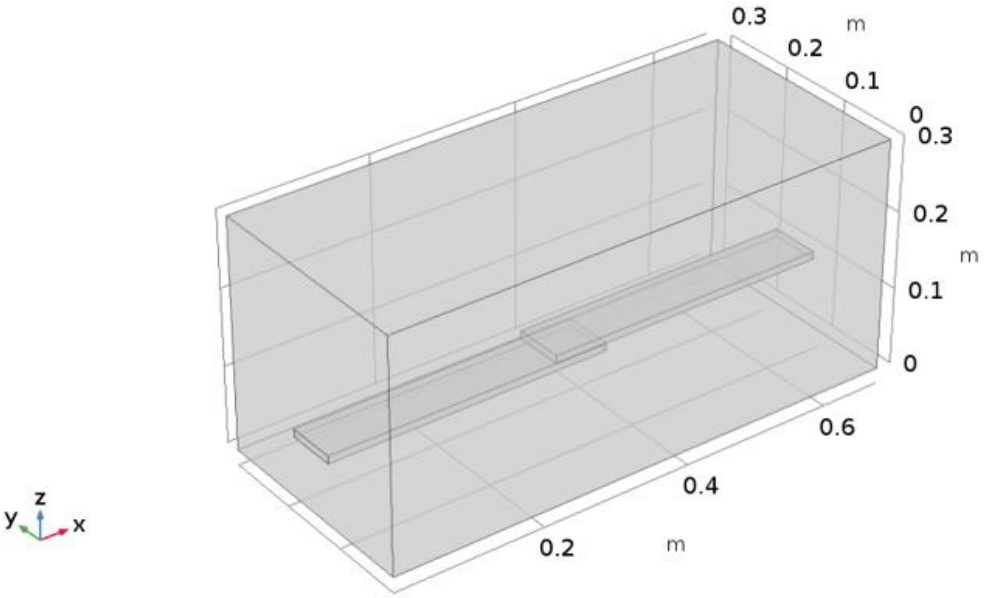

Fig. 2. 7 Geometry of busbar compartment model

As seen, the whole 3D gemetry is a mirror-symmetric geometry. To reduce the amount of simulation work and save the calculation time, the whole busbar compartment model is cut into two halves along the middle x-z plane and only a half is simulated when the numerical calculation was carried out in COMSOL.

In conclusion, the geometry of our computer model is built as shown in Figure 2.8:

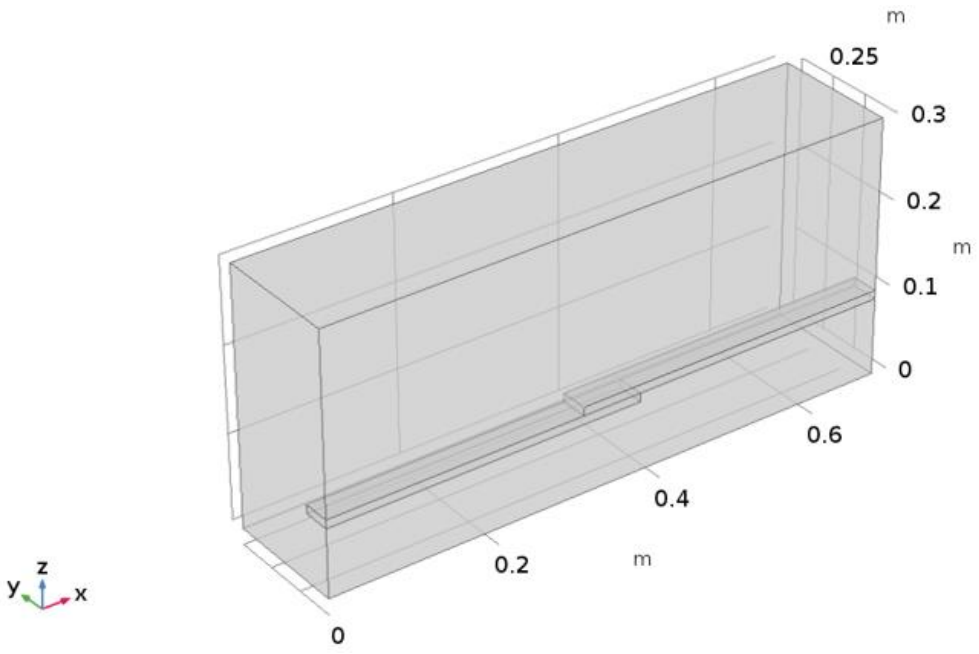

Fig. 2. 8 The CFD simulation model of busbar compartment model

2.2.4 Material properties

In this project, the heat conduction process occurs in both copper conductor and air flow, the numerical value of thermal conductivity of either copper or air needs to be defined accurately.

Thermal conductivity is used to indicate the rate of heat flow in a given material. For the conduction process in fluid, the faster the fluid molecules move, the faster they will transport the energy and dissipate the heat. Therefore, the velocity of fluid molecule would impact the conduction process dramatically. In other words, the thermal conductivity is mainly dependent on temperature, which is the main cause of active molecule in fluid. In this project, the temperature range of air is evaluated from as low as 293 K, and no higher than 350 K, so the dependence of thermal conductivity to temperature is referred from [41], and shown in equation (2-13) and Figure 2.9:

$$k_{air} = -0.00227583562 + 1.15480022 \times 10^{-4} \times T - 7.90252856 \times 10^{-8} \times T^2 + 4.11702505 \times 10^{-11} \times T^3 - 7.43864331 \times 10^{-15} \times T^4 \quad (2\text{-}13)$$

Where k_{air} (W/(m·K)) is the thermal conductivity of air at T (K).

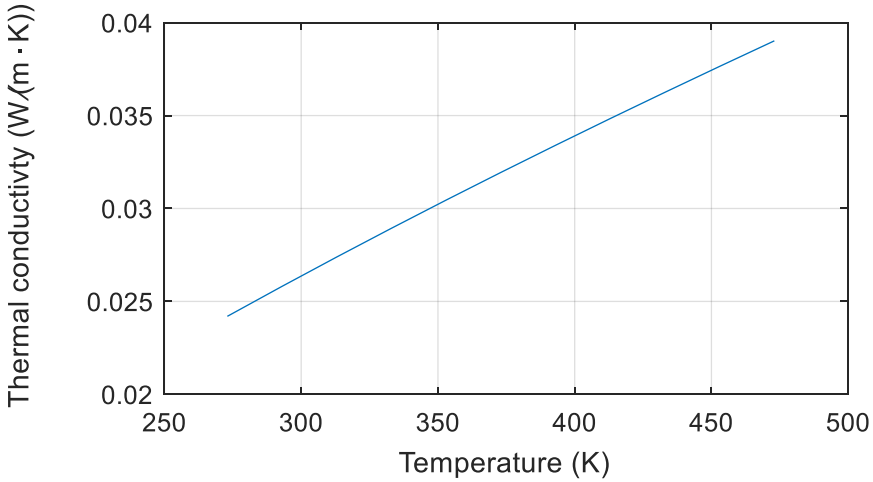

Fig. 2. 9 Thermal conductivity of air versus temperature

For electrical conductors, just like electrons transfer electrical charge, these electrons also carry thermal energy from a high-temperature region to a low-temperature region. Although thermal energy can also be transmitted by vibration in lattice structure of material, the energy transferred by vibration is much less than by free electrons. The main material of the conductors in our case is copper, which transfers heat mainly by free electrons. Since, the heat conduction process in copper conductor is mainly by free electrons, the temperature effect to the thermal conductivity is negligible, especially in temperature range from 293 K to 373 K for this project. As the temperature does not change much, the value of its thermal conductivity of the copper conductor is set constant as 385 (W/(m·K)) [41].

Due to Navier-Stokes equation group used in this model, the other values of air, as dynamic viscosity, heat capacity and density, change with temperature and pressure

difference. Furthermore, in natural convection, the air flows because of buoyancy force and gravity, so the gravity factor of air should also be set as 9.8 N/m^2.

For dynamic viscosity μ ((N·S)/m^2), it can be calculated in equation (2-14) [2] and shown in Figure 2.10:

$$\mu = T \times (8.38278 \times 10^{-7} + 8.35717342 \times 10^{-8} \times T - 7.69429583 \times 10^{-11} \times T^2 + 4.6437266 \times 10^{-14} \times T^3 - 1.06585607 \times 10^{-17} \times T^4 \quad (2\text{-}14)$$

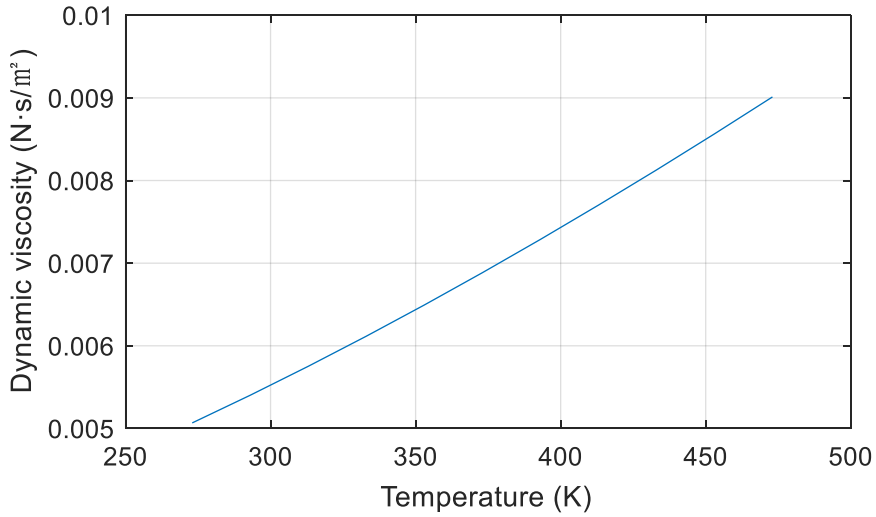

Fig. 2. 10 Dynamic viscosity of air versus temperature

As for heat capacity C_p (J/(Kg·K)), it can be calculated in equation (2-15) [2] and shown in Figure 2.11:

$$C_p = 1047.63657 - 0.372589265 \times T + 9.45304214 \times 10^{-4} \times T^2 - 6.02409443 \times 10^{-7} \times T^3 + 1.2858961 \times 10^{-10} \times T^4 \quad (2\text{-}15)$$

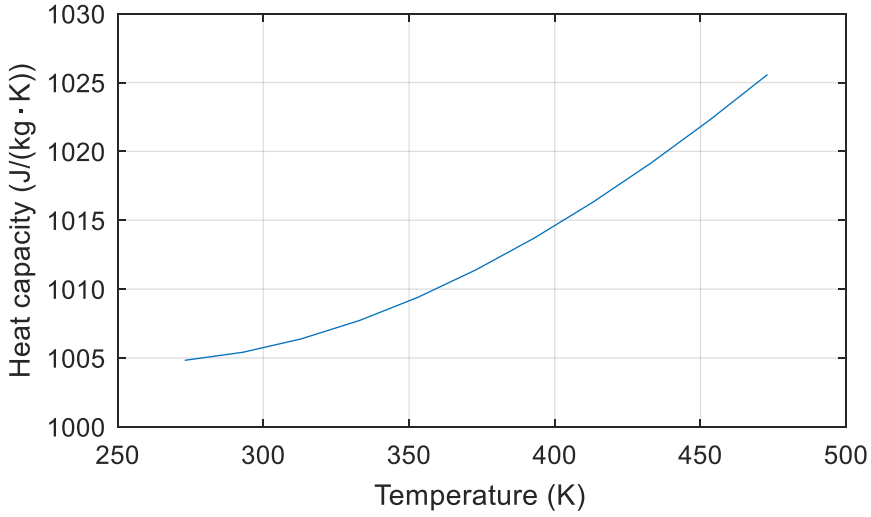

Fig. 2. 11 Heat capacity of air versus temperature

As for density, it is a function of temperature and pressure, so the air density is expressed as in equation (2-16) [2]:

$$\rho = \frac{p}{R_{specific} \cdot T} \tag{2- 16}$$

Where ρ (kg/m^3) is the air density, p (P_a) is the pressure, T (K) is the absolutely temperature, $R_{specific}$ (J/(kg·K)) is the specific gas constant of air, set as 287.508.

2.3 Governing equations and setting in CFD models

The thermal management in most electrical devices depends on two coupled processes, electrical heating (Joule heating) and conductor cooling (heat dissipation). In the electrical apparatus, Joule heating is treated as a heat source in the heat transfer process. When the temperature of conductor rises, the electrical conductivity of the conducting material would change. This in return varies the intensity of Joule heating. Joule heating as an energy source is obtained by solving the current continuity equation (2-1) to (2-4). Conductor cooling is realized by the heat transfer process. To obtain the true temperature of conductor, the two processes must be coupled to take the mutual influence into account.

Therefore, in our model two physical fields as electrical field and thermal-flow field are coupled strongly, the heat is generated by Joule heating of electrical current in solid busbar conductor, and then heat is dissipated from solid copper conductor to surrounding air by conduction, the fluid will take the energy and transfer it mainly by convection. Whilst the convection process in the fluid would have a dramatic impact on the conduction process between solid and fluid. The faster the air flow is, the cooler the solid conductor will be. This thermal-flow field is named as conjugate heat transfer problem in most thermal management study.

First of all, a stable current source is set in the copper busbar area, shown as the blue part in Figure 2.12, and its electrical field is solved by the equation of continuity of current. The rest domain is air in Figure 2.12:

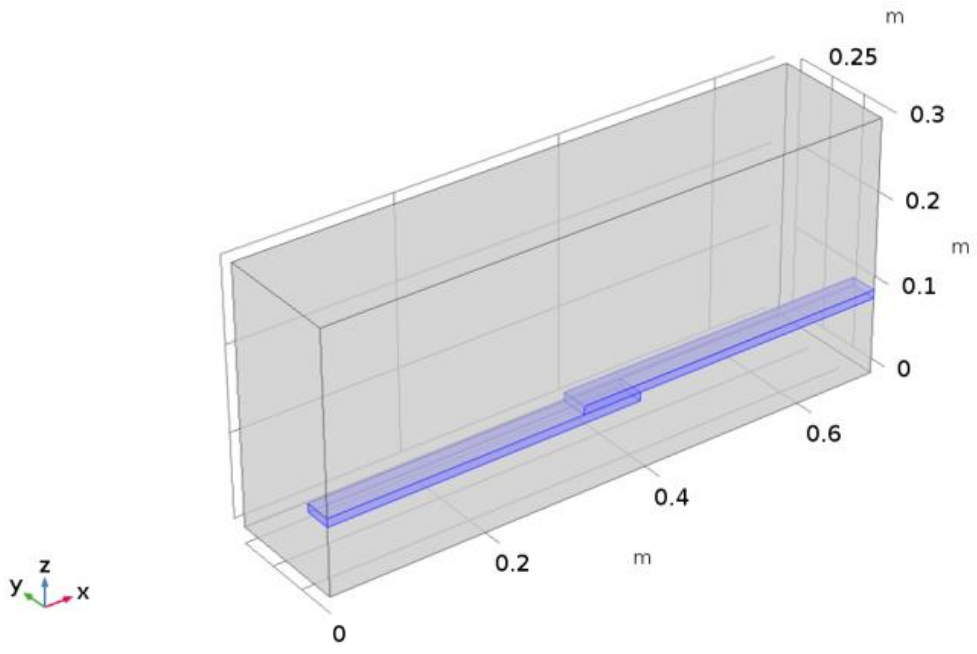

Fig. 2. 12 Domain for electrical field in blue parts

The conjugate heat transfer process is occurred on the surface of solid conductor and in the air flow domain. The governing equations of the fluid part is the combination

of conservation equations of mass, momentum and energy. The equations (2-18) to (2-20) are then set by adding the relative interfaces in the rest domain. There are two mathematical models to describe the flow pattern, as laminar flow and turbulent flow. The pattern flow is dependent on Reynold number, which is the ratio of inertial forces to viscous forces within the fluid. The Reynold number is calculated in equation (2-17), and it was estimated below 1000 when the maximum largest length was chosen as 0.2 m, which is distance from upper busbar surface to top enclosure wall. Therefore, the flow regime is defined as laminar flow in the busbar compartment model. Hence, the governing equations for the busbar compartment model is shown as following equations (2-18) to (2-20).

$$R_e = \frac{\rho u L}{\mu} \tag{2- 17}$$

$$\rho C_p \frac{\partial_T}{\partial t} + \rho C_p u \cdot \nabla T + \nabla(-k\nabla T) = Q \tag{2- 18}$$

$$\rho(\nabla \cdot u)u = 0 \tag{2- 19}$$

$$\rho u(\nabla \cdot u) = \nabla\left[-pI + \mu(\nabla \cdot u) - \frac{2}{3}\mu(\nabla \cdot u)I\right] + F \tag{2- 20}$$

Where: R_e is Reynolds number, L (m) is the characteristic linear dimension, ρ (Kg⁄m^3) is gas density, u is velocity vector, p (P_a) is pressure, I is three-dimensional identity matrix, C_p (J⁄(kg·K)) is heat capacity, μ (P_a·s) is dynamic viscosity, Q (W⁄m^3) is Joule loss and F is the volume force of gravity.

2.4 Boundary condition and initial value

2.4.1 Boundary conditions setting

How to set boundary conditions and choose initial values are the two key issues for numerical calculation, they ensure that the model can reach a correct solution.

Boundary condition is the restriction of the boundary with space or time in the whole calculating domain, it can define the maximum, minimum or the only solution in each individual physical process.

In this thesis, boundary is chosen to be the enclosure wall, and there are two different ways to set the boundary condition when facing a conjugated heat transfer problem in thermal-flow filed study, one is setting the boundary temperature and the other is to set heat flux. As setting the temperature is an easier way to obtain a solution than setting the heat flux for the boundary wall, the definition of boundary is a constant temperature and the relevant equation for boundary wall is simple. However, if the temperature changes at the boundary wall, then setting the heat flux is more appropriate. And the partial differential equation for setting the heat flux makes the numerical calculation more complex, which takes more time to solve.

In the light of above, how to set the boundary condition can easily make a difference between a successful and an unsuccessful computation process, or between a fast and a slow one. In our case, the maximum temperature under normal working condition is the most important parameter we care, and it is difficult to know which setting for boundary condition is more suitable than the other for prediction of maximum temperature and the study of thermal-flow field. Therefore, in section 5.4, the numerical results of the two different boundary conditions are discussed and then a suitable approach is decided through comparison with measurement results.

In reality, these solid enclosure walls transfer the heat from the inner side of the wall to the outside environment, and the temperatures of the individual side of the four walls are not the same.

By setting the heat flux as boundary condition, temperature distribution on the surface of enclosure wall can be obtained. However, this method to set the boundary condition requires a high quality of mesh element and extra governing equation for

heat transfer through the wall, these make the simulation process difficult to converge and time consuming. The setting strategy of heat flux is shown in Figure 2.13:

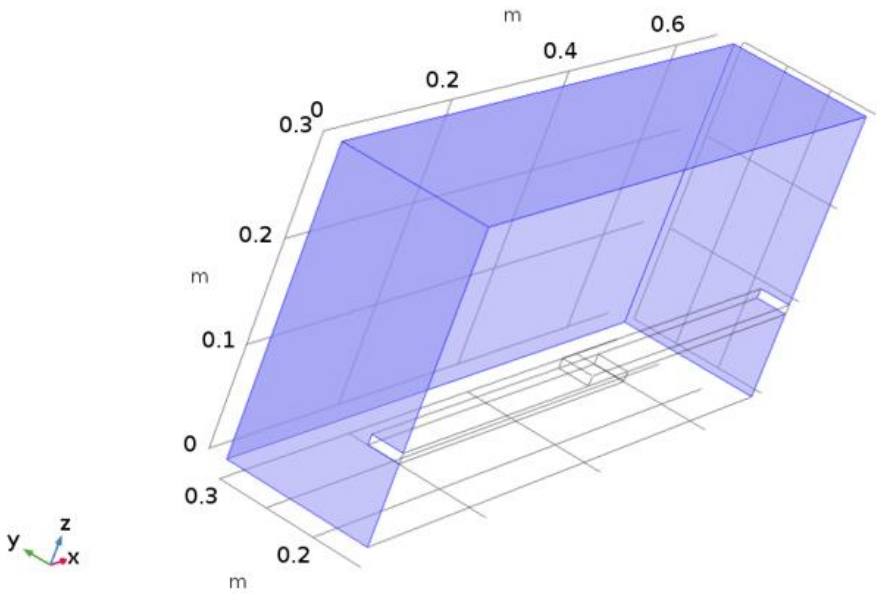

Fig. 2. 13 Heat flux set for boundary solid wall

The heat dissipated by the wall is set on the blue surface in Figure 2.13, the top wall and 3 side walls are given an unknown heat flux each, governing by convection equation (2-10) and radiation equation (2-12). In addition, the ambient temperature outside the 4 walls is set constant as ambient temperature. The two terminals of the busbar are set as constant temperature measured by the experiments. As the busbar compartment model, the bottom wall is placed on the ground, the temperature of the bottom wall is set as the ambient temperature.

On the other hand, the constant temperature set on each individual wall could reduce the complexity of numerical calculation, and it also saves the time of simulation process. When setting the boundary condition as constant temperature, it is straightforward as shown in Figure. 2.14:

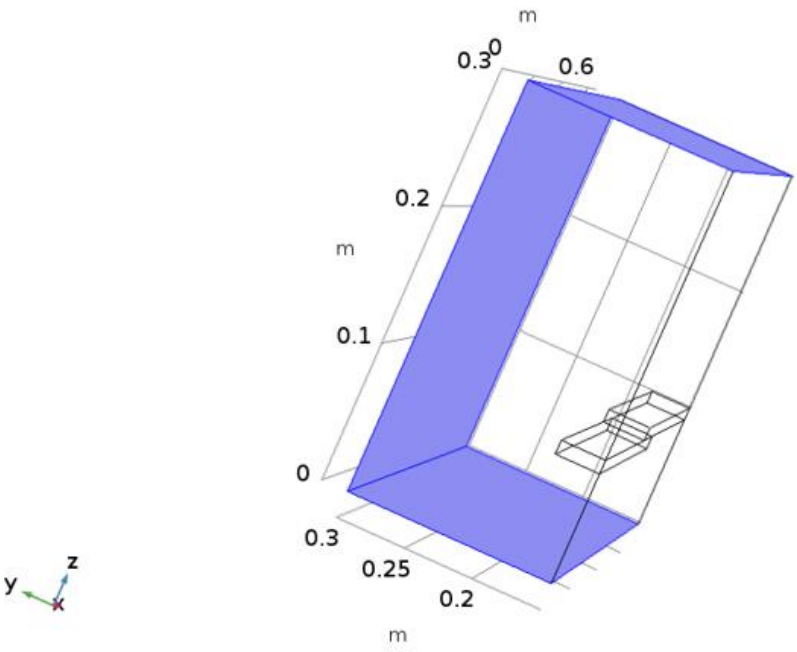

Fig. 2. 14 Temperature boundary set for busbar terminal

As the busbar terminal is at the same surface as the side wall (y-z plane), and heat is conducted most through the busbar terminal than the side wall. The side wall is set as a thermal insulating wall and the busbar terminal is set a constant temperature as measured in the experiments. The top wall and the side wall at x-z plane are both set a constant temperature, the temperature set for each individual wall was from the experimental results of temperature measurement.

2.4.2 Initial value

On the other hand, initial values are set in the numerical model before calculating the governing equations, and they are compulsory to both the transient and steady-state process. As the project is focused on the steady-state condition, initial value needs to be chosen wisely to shorten the calculation time to reach convergence, but it is not necessary for the steady-state condition, especially in our case.

2.5 Mesh strategies

Before the final calculating stage in numerical calculation, modern CFD software applies to the calculation domain a series of cells, elements and nodes that conform all together, as the so called mesh. Then the governing equations would be calculated at each of these nodes. Thus, the design of the mesh to its computation model is vital important to the computational process and the consequent success of the simulation.

As CFD technology is highly developed, better algorithms and discretion method have become available to the thermal-fluid dynamics community. By adding proper solvers to the disposable tools, the meshing process has increased its possibility of automation. However, designing and generating a proper mesh for complex geometry in coupled physical processes is still challenging and time consuming. There are two key issues which must be considered. The first one is the selection of appropriate shape of the finite element. The proper shape of element ensures that the element could stretch well in individual geometry, and it could provide a smooth grow of mesh element size to lead the solver to convergence to generate accurate results. The second issue is the size of mesh element should be designed sufficiently small in the area where energy transfer occurs most. However, if all the mesh elements in the whole domain are extremely fine, extra unnecessary computational resources will be needed to obtain the final result, even worse the computer may not be able to meet the demand of solver when facing an extremely complex geometry. The size of mesh element for this particular research work is defined by mesh refinement study and the results are shown in section 5.1.

Therefore, in different cases, the mesh system should be designed individually, especially the vital area in each domain should be accounted for. To design the mesh

elements, the mesh pattern and mesh element shape from previous experience are always useful.

2.5.1 Vital area

In the numerical solution process, considering the limitation of computer and time consumed for each calculation, some vital areas in the whole domain need to be spilt into mesh elements in small sizes, and the rest areas are simply spilt into relatively coarse large-size mesh elements. The crucial area is defined as the place where energy transfer occurs most.

In the thermal-flow field, the thermal boundary layer between the solid body surface and the fluid is where most of the energy from the hot solid body is transferred into the fluid by conduction. In thermodynamics, the proper solution of the numerical calculation in this thermal boundary layer region is crucial for the success of the entire simulation process, because it not only transfers most thermal energy, but it is also the key area to make the thermal field and flow field fully coupled. If this critical zone is not with sufficiently good resolution, the execution of the numerical calculation can be diverged or end with mistaken and unrealistic results. Many complex problems in thermodynamics of engineering applications have been simplified to a study of flow within the boundary layer and its effect on the general flow around a body [42].

Different objects in the system interacting with the flow, would generate different boundary layers, so the boundary layer regions can be different for each individual case. The following subsection is intended to clarify the study of the flow inside the thermal boundary layer and its interaction with the outer flow to identify the vital area in the whole domain.

2.5.1.1 Thermal boundary layer

In 1905, one of the most important fluid-dynamics paper ever written was published. It was titled 'On the motion of fluids with very small viscosity' by Ludwing Prandtl [43]. This paper gave the first description of the concept of boundary layer. In this type of flow associated with a body in flight, the boundary layer is very thin as compared to the size of body.

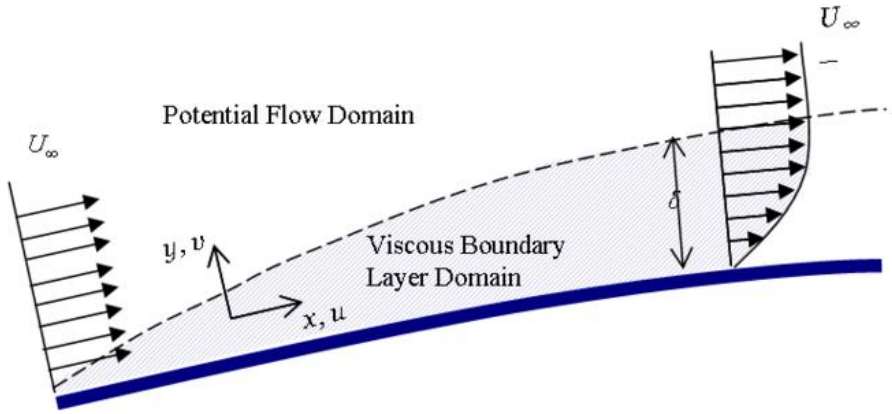

Fig. 2. 15 Thermal boundary layer. U∞ (m⁄s) is the velocity along the boundary, u (m⁄s) is the velocity vector in x direction, v (m⁄s) is the velocity vector in y direction, the area in dashed line is thermal boundary area (viscous boundary layer domain). δ (m) is the thickness of thermal boundary layer. [43]

The explanation of the physical process in the boundary layer between a fluid and a solid body could be obtained by the hypothesis of an adhesion of the fluids to the wall. There is a zero-relative velocity on the surface of the wall in the hypothesis from Ludwing Prandtl . If the velocity was small and the fluid path along the wall was not too long, the fluid velocity ought to resume its normal value at a very short distance from the wall, shown as Figure 2.15. In this thin transition layer, however, the sharp

changes of velocity, even with a small friction coefficient, can produce marked influence in terms of temperature and pressure.

One of the main consequences is that there is a great temperature gradient in thermal boundary layer. As hypothesised, the velocity of air on the surface of solid body is assumed as zero, so the heat transfer on the body surface is only by conduction. In Fourier's law of conduction, the effectiveness of conduction is only dependent on the thermal conductivity of each material. In this thesis, the conductivity of copper and air (20 ^{o}C) are 385 (W⁄(m·k)) and 0.024 (W⁄(m·k)) respectively. Due to low thermal conductivity of air, the temperature gradient in thermal boundary layer is extremely high, much higher than the other areas in the whole domain.

The other marked influence is that the viscosity by shear stress gives the major drag in the thermal boundary layer to keep the air along on the surface of hot solid body. According to Newton's shear stress law [40], which states that the shear stress is proportional to the velocity gradient as given in equation (2-21):

$$\tau = \mu \frac{\partial U_{\infty}}{\partial_y} \qquad (2\text{-}21)$$

Where τ (P_a) is the shear stress, μ (P_a·s) is the dynamic viscosity of the fluid, U_{∞} (m⁄s) is the velocity along the boundary, y (m) is the height of the boundary.

However, to the fluid outside the thermal boundary layer, it is ought to be separated from the wall according to Prandtl's theory [43]. The pressure distribution on the surface of the body is radically changed once the fluid flows out the thermal boundary layer. The pressure outside the boundary layer creates a pressure drag due to flow separation that is a large unbalanced force which acts in the direction of the free stream flow. The external flow that promotes boundary layer separation is a type of flow that produces an adverse pressure gradient, which will occur when the flow

presents an increasing pressure in the same direction of the fluid. This means the influence of viscosity of the flow outside of the thermal boundary layer is negligible, and the outer flow can be seen as inviscid flow, which is mainly caused by buoyance force, gravity force and other pressure from forced flow. At the same time, the temperature and pressure distribution and energy transfer for the outer flow is not as large as the distribution inside the thermal boundary layer.

In the light of above, the temperature variation in the thermal boundary layer is larger than any other area in the whole system, and this area is the crucial zone which needs to be calculated with high accuracy.

2.5.2 Prismatic layer technique

As stated above, the mesh element pattern of the calculating domain is most referred from previous experience. In our case, the fully coupled thermal-flow field is be studied and analysed, which means the energy transfer in both solid body and fluid domain are calculated. Therefore, the method called ‘prismatic boundary technique [44-46] ‘is used.

Considering the vital area rather than the rest of the domain, the success of fully-coupled physical fields is dependent on the calculation of thermal boundary layer as stated previously, where the energy change is the most in thermodynamics. The ‘prismatic boundary technique’ is mainly designed to mesh these kinds of area.

By previous experience, the whole calculating domain in thermal-flow field would be divided into two parts, the solid body and fluid flow. For the solid body, most of them are the heat source, and due to the high thermal conductivity of the material, the energy is transferred easily and the temperature change is not massive. Therefore, the tetrahedral element is used in the solid body domain. However, the tetrahedral element could not stretch well in the border of curved surface, and this could impact

the accuracy of calculation results. In fluid domain, the tetrahedral and prismatic boundary are both used. To most fluid area outside the thermal boundary layer, the energy transport, temperature and velocity are not large, the tetrahedral elements can also be used to save computational cost. To the thermal boundary layer, the prismatic boundary method is used, it consists of prism elements with both quadrilateral and triangle base, as well quadrilateral for 2D surface. 3D hexahedral and 2D quadrilateral elements are efficient to resolve the unidirectional problem in the whole domain, which is suitable to the area controlled by shear stress. When facing the intricate geometry, both tetrahedral and pyramid 3D elements can be added in the boundary to curved corners.

2.5.3 Mesh pattern

In this thesis, the surface of solid busbar conductor is the vital area in the whole domain, because it is the place where most energy transfer take place from the solid heat source to the air flow, as stated as thermal boundary in the busbar compartment model. From the concept of thermal boundary layer, the heat transfer direction can be seen as only in one direction, from the body surface to air flow. Therefore, this thermal boundary layer is filled with 3D hexahedral and 2D quadrilateral mesh elements. Inside the busbar and air domain, the energy of different mesh cells does not change much, hence the tetrahedral mesh elements are used to fill the two domains, whilst the prism element with triangle base and pyramid elements which are stretched well, are placed in the corner or curved spaces. Therefore, the mesh pattern for the busbar compartment model is shown in Figures 2.16 and 2.17:

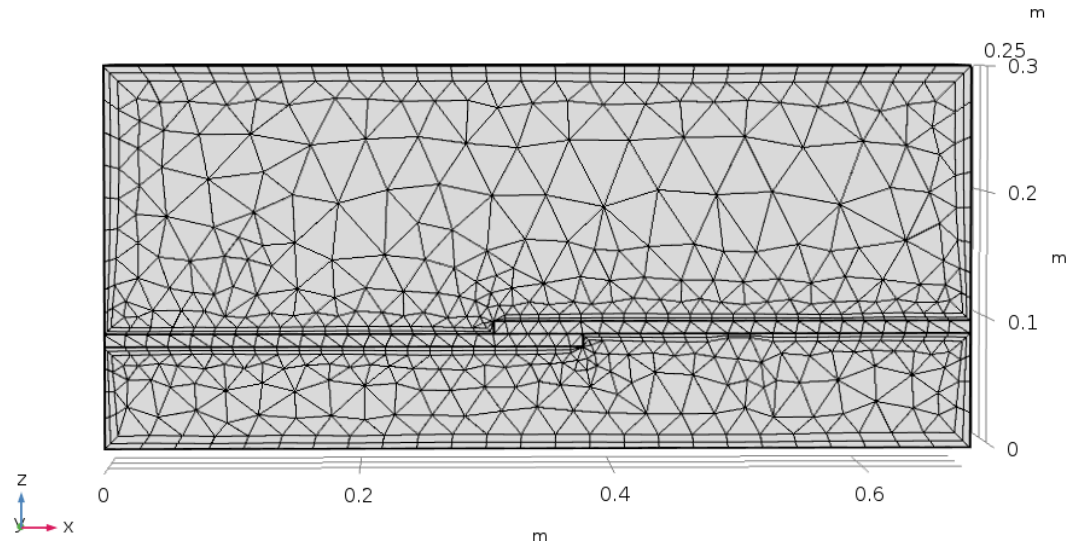

Fig. 2. 16 Front view of mesh pattern for the busbar compartment model

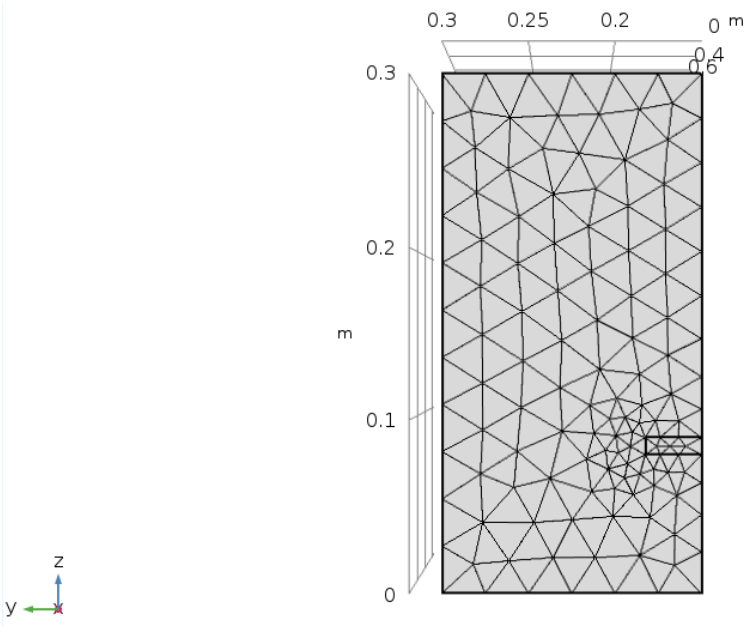

Fig. 2. 17 Side view of mesh pattern for the busbar compartment model

Post-data process and result plotting are the final two steps for CFD simulation. Although important, they are rather straight forward hence no more description will be given on these two topics.

2.6 Summary

Finite element method for numerical analysis of thermal flow field is specially developed into a subject as so called computational fluid dynamics (CFD). In this Chapter, thermal dissipation processes and governing equations are studied and key issues for CFD simulation, such as boundary condition setting, initial value setting, meshing pattern and etc are discussed. This forms a basis for fundamental understanding and further research studies in Chapter 4.

Chapter 3 Experimental Set-up

3.1 Introduction

In chapter 3, the experimental design and its setup are introduced. The experiment is used to validate our mathematic model and the numerical calculation in CFD software COMSOL. To do the validation in the thermal-flow field calculation, a busbar compartment model based on the geometry of KYN-28 switching cabinet was designed. The temperature variation of both solid conductor and flow fluid were measured and recorded.

This project is funded by Pinggao Group Ltd., therefore, all the experimental devices, i.e. busbar conductors and Perspex enclosure, are all from Pinggao company.

3.2 Experiment setup design

The experimental setup is designed for the measurement of electrical resistance and temperature inside the switching cabinet. Because the project is focused on busbar compartment, the overlapped busbars are placed in a Perspex enclosure to represent the whole compartment.

To enable the busbar conductor to reach a steady-state condition, a stable current source HSXSLQ-H/2500A is used, and it also has the function of acquiring the temperature measurement. The electrical resistance was measured by the machine DLR 600 A, which provides an accurate result even the resistance below 100μΩ. Thermocouple and thermos-reader are used to measure the temperature and display the values. The configuration of our experimental setup and individual devices are shown in Figure 3.1 to Figure 3.4:

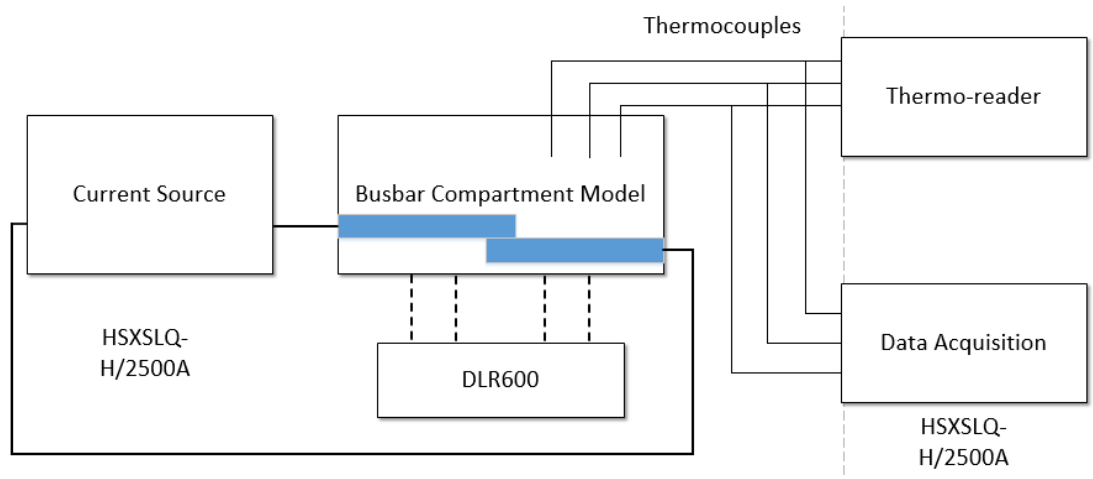

Fig. 3. 1 Configuration of experiment setup

Fig. 3. 2 HSXSLQ-H/2500A current source and temperature data acquisition machine

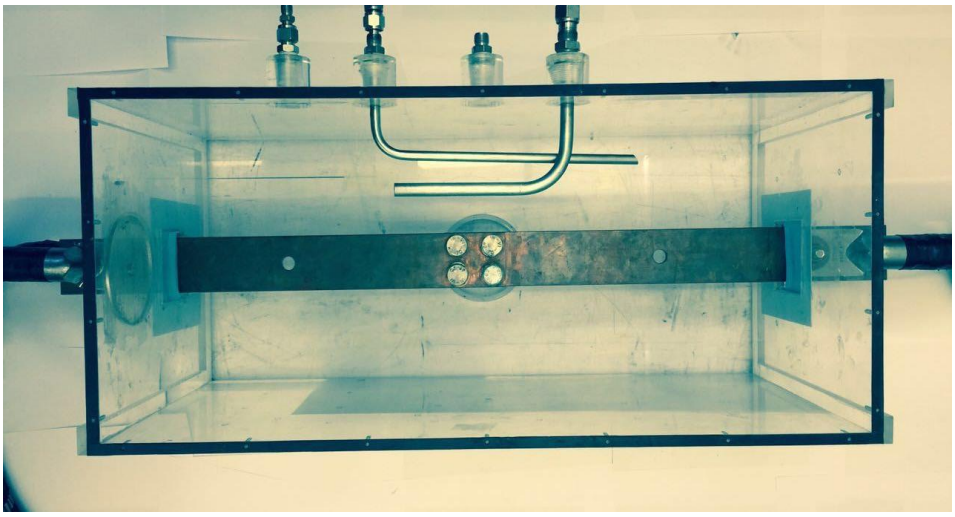

Fig. 3. 3 Busbar compartment model

Fig. 3. 4 Electrical resistance measurement machine DLR600

3.1.1 Current source

In the experimental setup, an stable current source is the vitally important component. Therefore, the current source and temperature data acquisition device HSXSLQ-H/2500A is selected and used. As the current source, it can provide a stable

AC current, of which range is r.m.s from 0 to 2500 A, and the accuracy of current is 0.5%±3 A. As the required current range in our experiment is from 600 A to 1200 A, the current change is within 0.5%.

HSXSLQ-H/2500A consists of two different parts, a stable current source as well as a temperature acquisition device which could record the temperature measured by thermocouples connected to the device. For temperature measurement and recording, there are eight channels to acquire temperature measured by thermocouples connected at the back of the machine, and the temperature variation can be recorded in every 5 seconds. Moreover, all the data could be displayed in chart, graph or table at the front panel, which helps identify a steady-state condition, especially in our cases. All the recordings can be output as well, which makes it easy to obtain and analyse the results using other available external software. However, the accuracy and uncertainty of these channels should be defined, and relevant calibration tests are introduced and described in section 3.4.2.

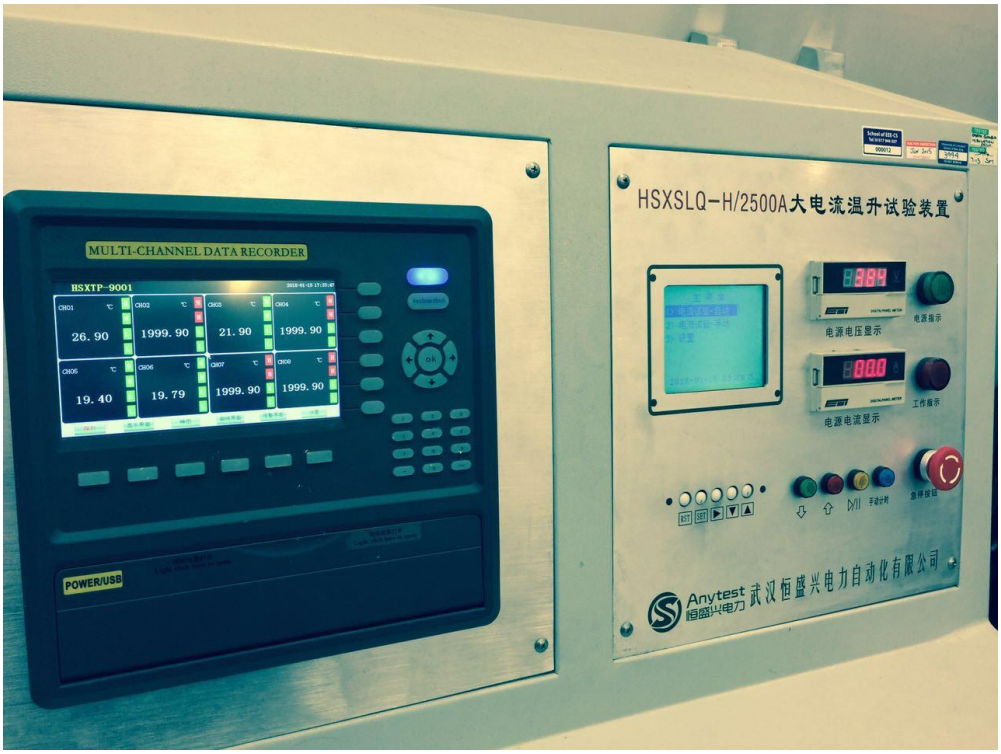

Fig. 3. 5 Temperature measurement and recording in HSXSLQ-H/2500A

HSXSLQ-H/2500A is connected with the simplified busbar compartment model by cables. To reduce the thermal effect of cable connection due to the contact resistance, preliminary tests on the cable connections have been done by previous colleague in [47]. In [47], a suitable torque was defined and 80Nm was recommended when bolts were screwed to connect the cable to copper busbar and adaptors were also used.

Fig. 3. 6 Adaptors used (above) and cable connected (below)

3.1.2 Busbar compartment model

A simple geometry is built in our experimental setup instead of the whole complex structure of KYN-28 switching cabinet. In the whole current loop, the hottest spots are mainly located in contact areas, which are busbar joints and circuit breaker contact arm. Compared to tulip contact arm in circuit breaker, the busbar bolted joint has a more simple and uniform geometry, which is also easy for the processor to

measure the temperature and electrical resistance. Therefore, the design of enclosure and conductor are based on the busbar compartment in KYN-28 switching cabinet.

The geometry of our busbar compartment model was based on the KYN-28 switching cabinet from Pinggao Company, and the IEC standard 60694 (common specification for high-voltage switchgear and control-gear standards) is also taken as a reference when the simplified busbar compartment model is designed.

In IEC 60694 section 6.5.2 (arrangement of the experiment), the environment of test is defined as 'the environment should be substantially free from air current, and the velocity of ambient air should not exceed 0.5 m⁄s'. Therefore, the ambient temperature and air velocity are checked and recorded before each test, to make sure the environment would be confirmed to comply to standards.

With the respect to the design of solid conductor, the busbars in the KYN-28 switching cabinet are for three-phase and they are supported by insulators (structure introduced in section 1.3). In IEC standard 60694, it is reported in section 6.5 (temperature-rise test) as 'temperature-rise tests of three-pole switchgear could be made with only a single pole, if the rated normal current of switchgear is more than 630A'. As for the insulator supporting, it is defined as 'insulation part may be appreciably reduced, when the insulation to earth has no significant influence on temperature-rises in large switchgear'.

Considering the geometry of KYN-28 switching cabinet in chapter 1, the rated current of KYN-28 switching cabinet is from 630 A to 4000 A, and the dimension of the whole cabinet is as large as 180 cm×150 cm×120 cm and the insulation part in the busbar compartment is bushing, which insulates the busbar conductor to the metal enclosure. This large size cabinet and the bushing insulation mean that the insulation only have negligible influence on the temperature-rise. In the light of above, the

conductor is taken as a single-phase copper busbar without support insulators, and it is placed in an enclosure. The configuration of the single busbar enclosure is shown in Figure 3.7:

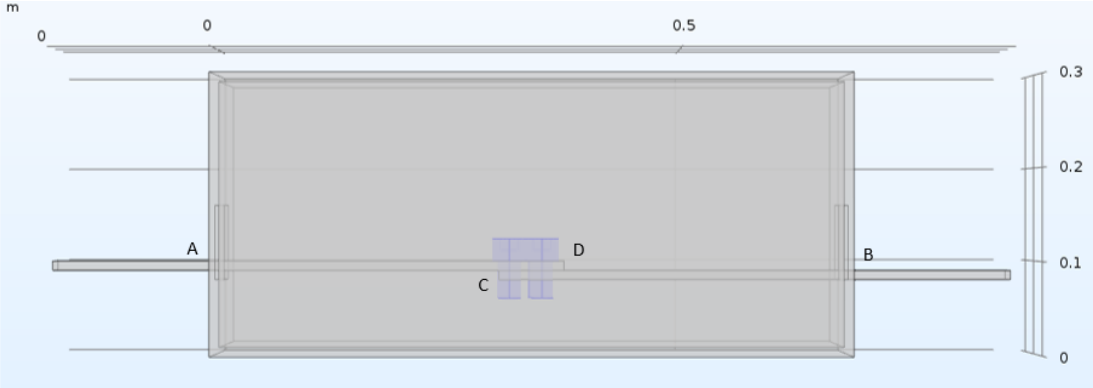

Fig. 3. 7 Configuration of busbar conductor placed in the enclosure

As this project is funded by Pinggao Group company, the copper busbar is provided by the company, and its dimensions are 550 mm×65 mm×10 mm. The two busbars are connected by four M24 hexagonal bolts, and the overlapping area is 70 mm×65 mm. The enclosure is made of Perspex, whose dimensions are 700 mm×300 mm×300 mm. On two side walls, there are two opening square, whose dimension is 8 mm*8 mm, for placing the busbars. After placing the busbar in the enclosure, the two opening squares are sealed with thermal-pad. In Figure 3.7, A and B are the busbar points at the opening square, points C and D are the terminals of overlapped busbar contact. All these dimensions are a reflection of the busbar compartment in the KYN-28 switching cabinet of Pinggao Group Ltd.

In summary, the simple busbar compartment model is designed as two busbars overlapped with each other and placed in a Perspex enclosure.

3.1.3 Thermocouple and thermo-reader

To validate the computer simulation model, the temperatures of both solid conductor and fluid air should be measured and recorded. There are two common methods to measure the temperature in the electrical devices, infrared camera or thermocouple. For infrared camera, it is normally used by pointedly its lens to a solid object's external surface and capture the image of solid object with temperature profiles, however the infrared light cannot pass through the wall of switching cabinet enclosure to capture the conductor's temperature. Thus, the camera can only measure the temperature of the outer surface of the enclosure. As the domain inside the enclosure is what engineers care, thermocouple was chosen as the temperature measurement device in our experiment. Furthermore, the thermocouple is also advantageous in terms of low cost, high accuracy and good stability at various levels of temperature, in addition to its ruggedness, repeatability and a fast response time.

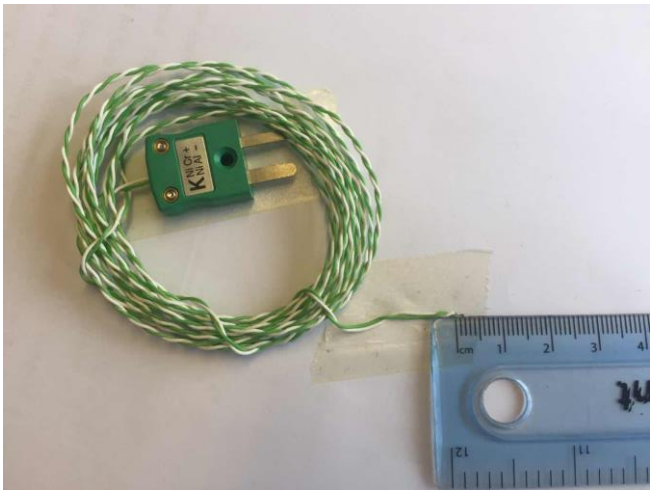

Fig. 3. 8 K type thermocouple used in experiment

Considering the temperature range and stability, the K type thermocouple is selected for this project. The temperature range is from -75 ^{o}C to 260 ^{o}C, and this kind of thermocouple could also measure the temperature in fluid, which helps us to measure the temperature of air inside the enclosure. For the sensor tip part of K type

thermocouple, its length is less than 2 mm, and this dimension could ensure the position of measurement in air flow. However, the accuracy and its uncertainty of the thermocouple is not defined, hence thermocouple calibration test in section 3.4.2.

Thermocouple works due to the principle of Seebeck effect, which states that a small voltage difference exists at the junction of two dissimilar metals.

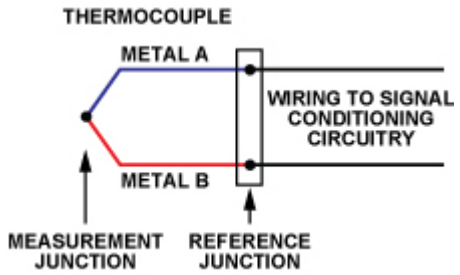

Fig. 3. 9 Thermocouple structure

In our cases, the thermocouples are placed on the surface of conductor, the conductor current and eddy current would have an impact to the small voltage drop in the thermocouple. Moreover, the air gap between thermocouple and solid surface would also affect the accuracy of measurement dramatically.

Due to the reasons above, thermocouples will be covered with a kind of material, called thermal-paste. Thermal-paste, is a thermally conductive and electrically insulating compound. It acts to maximise the heat transfer from the solid surface to the thermocouple sensor and eliminates the air gap between the conductor and thermocouple.

Five thermocouples were connected to the channels of HSXSLQ-H/2500A device to read and record the temperatures measured by thermocouples, however five channels are not enough for all the points measured. Therefore, a digital thermos-reader is needed to read the temperature measurement made by the rest of thermocouples. 1/2 6802 II Dual Channel Digital Thermometer is selected as the two-

channel digital thermometer. The plug of thermocouple can be easily inserted into the digital thermometer. Moreover, the digital thermometer can connect to a sensible and accurate probe, of which accuracy is 0.4%±0.1 ^{o}C. This thermometer and its probe would help us to define a temperature reference when the calibration test was carried out in section 3.4.1.

Fig. 3. 10 Digital thermometer and sensible probe

3.3 Experimental objective and methodology

In the temperature-rise test, there are four parts which need to measure the temperatures, as solid conductor, air flow, enclosure surface and ambient environment. Because this project is mainly focused on the prediction of maximum temperature in electrical apparatus under normal working condition, the steady-state condition of thermal modelling is what we need to study. The steady-state condition means the energy equilibrium, also means the temperature would not change with time. In standard IEC 60694, the steady-state condition is defined as: 'the test shall be made over a period of time sufficient for the temperature-rise to reach a stable value. This condition is deemed to be obtained when the increase of temperature-rise does not exceed 1 K in 1 hour.' Therefore, the finial temperature results should

be ensured its change is within 1 K in the last one hour. HSXSLQ-H/2500A has a data acquisition system which displays the temperature versus time, and therefore is useful to help identify the steady-state condition.

3.3.1 Ambient temperature

The temperature-rise test is to identify the temperature difference between the hottest area and ambient temperature. Therefore, an accurate measurement of ambient temperature is vitally important.

According to IEC standard 60694, the ambient temperature should be measured using the method: such as ambient air temperature, which is the average temperature of the air surrounding of the enclosed switchgear and control-gear, should be measured during the last quarter of the test period by means of at least three thermocouples. The thermocouple or other temperature-detecting devices equally distributed around the switchgear and control-gear at about the average height of its current-carrying parts and at a distance of about 1 m from the switchgear and control-gear. The thermocouple shall be protected against air currents and undue influence of heat. In order to avoid indication errors because of rapid temperature changes, the thermocouple may be put into small bottles containing about 0.5 litre of oil. During the last quarter of the test period, the change of ambient air temperature shall not exceed 1 K in 1 hour.

In our case, the copper busbars are both placed in the Perspex enclosure, and the temperature-rise change of the two busbars is estimated from 10 K to 60 K by natural convection. The test, which was measuring the velocity of air, was done every time to ensure the air flow does not affect the measurement of ambient temperature. Thus, three thermocouples are just placed in the three-dimension at 1m each away from the enclosure.

3.3.2 Copper conductor

In temperature-rise test, the temperature of hot spots in the system tested must be obtained. The heat is generated by the current carried in the conductor, so the solid conductor is the hottest area in the system. However, the thermal conductivity of copper is as high as 385 (W/(m·K)), which means the copper is good at transferring the heat and the temperature change along the busbar is relatively small. Due to this, the temperature change along the busbar is smaller compared to the temperature-rise of surrounding air. Hence, there is no need to place too many thermocouples to measure the copper busbar temperatures. Moreover, although the two busbars are not at the same height in the enclosure, the height difference is only 1 cm, whose effect can be ignored compared to the height of enclosure as 30 cm.

Therefore, a preliminary test is introduced in section 3.4.2 to define the positions of thermocouples placed along the busbar.

3.3.3 Air and enclosure

To validate the fully coupled thermal-flow processes, enough details must be obtained to validate the mathematical description of flow field. There are three factors used to describe the flow field, as velocity, pressure and temperature.

Compared to velocity and pressure of the flow, temperature is the easiest one to be measured, when considering the geometry of large-size electrical device and the measurement method. The flow velocity can only be measured by anemometer, and the size of anemometer is the limiting factor to place it in our system, whistle the K type thermocouple has only a length of 2 mm. Therefore, the thermocouples can be placed in the enclosure and the size of them are so small that they would not have a dramatic impact on the flow.

In the whole experimental system, it is impossible to measure the temperature of air flow at all points. Thus, the temperature of the hottest air can be measured, the temperature data can be used to represent the air flow. At the same time, an accurate prediction of temperature along solid enclosure wall of electrical device, is also helpful to monitor the temperature inside when the device is in normal working condition. Therefore, the temperature measurement is taken not only in air but also on the outside of solid enclosure wall.

As we all know, air flow right above the busbar is hotter than the air at other points, because the contact area generates more heat. Therefore, the measurement positions are in the middle y-z plane of the whole three-dimension geometry. The thermocouple position is shown in Figure 3.11:

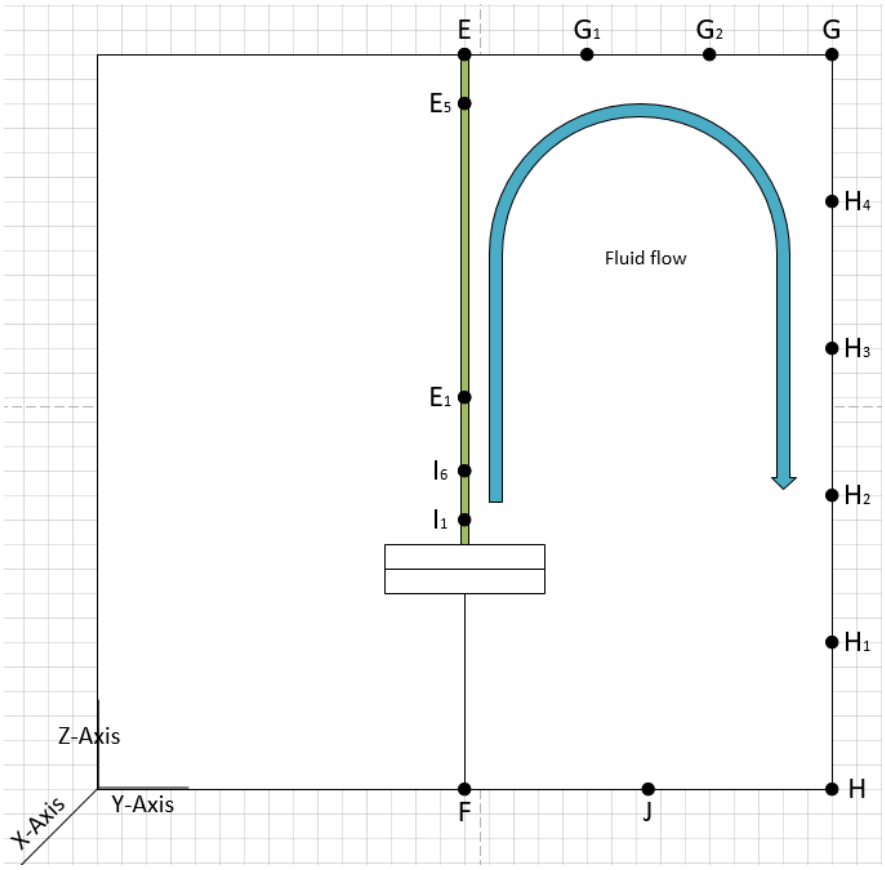

Fig. 3. 11 Middle y-z plate in three-dimension geometry. F (0.34,0.15,0) I_1 (0.34,0.15,0.105) I_5 (0.34,0.15,0.13) E_1 (0.34,0.15,0.16) E_5 (0.34,0.15,0.28)

E(0.34,0.15,0.3) G_1(0.34,0.2,0.3) G_2(0.34,0.25,0.3)G(0.34,0.3,0.3) H_4(0.34,0.3,0.24) H_3 (0.34,0.3,0.18) H_2 (0.34,0.3,0.12) H_1 (0.34,0.3,0.06) H (0.34,0.3,0) J(0.34,0.225,0) F(0.34,0.15,0)

In Figure 3.11, E and F are the middle points of outside of top and bottom solid wall respectively. G and H are the corner points of outside boundary wall respectively. Point I is in the middle of the overlapping busbar. Point J is the middle point between point F and point H. All the points E, F, J and H are placed on the outside wall of enclosure. The air flow is assumed that the cold air from bottom absorbs the heat from busbar, and the temperature rises, then the air goes up. Because there is no escape from the top wall, the air has to flow in the direction from point E to point G along the wall side, and then the air flows in the direction from the point G to bottom. In this whole process, the air would transfer the heat to the outside environment through the wall, and when the air flows from point G to bottom wall, it would get cooled and then go the busbar area again. The arrows indicate the airflow direction and they should not be taken as in the absolute sense.

As we can see, the side view is an axis-symmetric geometry from line EF, this means we only need to measure the temperature distribution in a half geometry, from E, G, H to F. The temperature of hot air is what we care most, so the temperature distribution between point I to E is useful to us. Moreover, according to the thermal boundary layer concept, the temperature in this layer is not a linear increase from point I to E. Therefore, from point I to point E, there are 12 K type thermocouples used, six are placed from point I upwards with a step of 5 mm, namely I_1 to I_6, and five thermocouples are placed from point I_6 upwards with a step of 30 mm, namely E_1 to E_5, and one thermocouple is placed on point E. These twelve thermocouples were attached in an insulating stick, which is the green area in Figure 3.11. The diameter of the stick is 4 mm. For the top wall, the distance from E to G, there are three thermocouples placed rightwards with a step of 50 mm, namely G_1, G_2 and

G. For the right side of wall, the path from point G to H, there are 4 thermocouples placed downwards with a step of 60 mm, namely H_4 to H_1. The last thermocouple is placed in point J to measure the temperature of bottom solid wall.

3.4 Preliminarily tests

3.4.1 Thermocouple and HSXSLQ-H/2500A machine calibration test

In the experimental setup, there are two devices used to measure the temperature, one is the K type thermocouple and the other is the data acquisition HSXSLQ-H/2500A system. The systematic error and uncertainty of these devices would affect the results. Therefore, a calibration test should be run firstly to determine the error and uncertainty of the machine, as well the thermocouple and the data acquisition system.

Considering the temperature range in this project, the normal temperature range should be from 20 ^{o}C to less than 80 ^{o}C. To identify the errors and uncertainties in this temperature range, the calibration test could been done by using iced water and boiling water, whose temperature can be referenced as nearly 0 ^{o}C and 100 ^{o}C. If the difference of each thermocouple to the measured calibration reference temperature is approximately the same in these two scenarios, the uncertainty and error of each thermocouple can be determined. To ensure the accuracy of temperature difference between the reference point and the thermocouple to be calibrated, a highly accurate probe sensor shown in section 3.1.3 and the thermocouple should be placed at the same place in either iced bath or the boiling bath (shown in Figure 3.12).

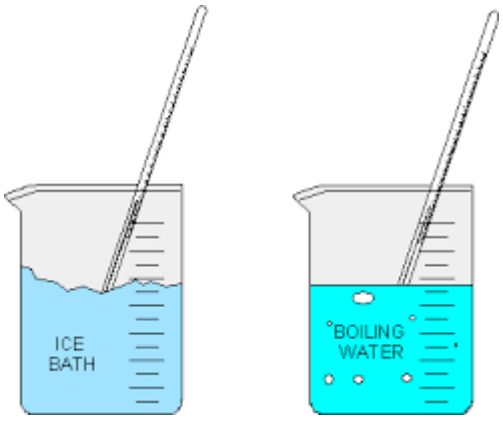

Fig. 3. 12 Iced and boiling water bath

The digital thermometer introduced in section 3.1.3 has two channels, to display the temperatures measured by the reference probe sensor in Figure 3.10 and the thermocouple shown in Figure 3.8. Therefore, one channel is connected to the probe sensor, and the other channel is connected to each individual thermocouple tested. Both iced water and boiling water calibration tests were done three times for repeatability.

The calibration results of the five channels of the HSXSLQ-H/2500A machine is shown in Table 3.1 to Table 3.2:

Table 3. 1 Iced water calibration test for data acquisition system

Temperature difference in each channel (K)	Iced water test 1	Iced water test 2	Iced water test 3	Average temperature difference (K)
Channel 1	0.2	0.4	0.2	0.27 ± 0.11
Channel 2	1.5	1.8	1.4	1.57 ± 0.21
Channel 3	0.4	0.6	0.8	0.60 ± 0.20
Channel 4	0.8	0.9	0.8	0.83 ± 0.06
Channel 5	1.8	2.0	2.4	2.07 ± 0.31

Table 3. 2 Boiling water calibration test for data acquisition system

Temperature difference in each channel (K)	Boiling water test 1	Boiling water test 2	Boiling water test 3	Average temperature difference (K)
Channel 1	0.4	0.6	0.2	0.40 ± 0.20
Channel 2	1.8	1.9	1.7	1.80 ± 0.10
Channel 3	1.0	0.8	0.8	0.87 ± 0.10
Channel 4	0.9	1.0	0.9	0.93 ± 0.06
Channel 5	2.2	2.4	2.4	2.33 ± 0.12

From the results above, the uncertainty of each channel at the temperature of 0 ^{o}C and 100 ^{o}C is shown in Table 3.3:

Table 3. 3 Uncertainty of each channel between iced water and boiling water calibration test for data acquisition system of HSXSLQ-H/2500A

Temperature difference in each channel (K)	Temperature difference in iced water test (K)	Temperature difference in boiling water test (K)	Average temperature difference (K)
Channel 1	0.27 ± 0.11	0.40 ± 0.20	0.33
Channel 2	1.57 ± 0.21	1.80 ± 0.10	1.69
Channel 3	0.60 ± 0.20	0.87 ± 0.10	0.74
Channel 4	0.83 ± 0.06	0.93 ± 0.06	0.88
Channel 5	2.07 ± 0.31	2.33 ± 0.12	2.20

The systematic error of the temperature measured by each channel of HSXSLQ-H/2500A is calculated as the average value of temperature differences between the reference and the calibrated channel for both iced and boiling water tests, shown in Table 3.3. The systematic error of each individual channel was defined as the average value of the temperature differences for both iced and boiling water tests.

In the tests above, the temperature measured by these 5 channels were all above the temperatures measured by the accurate probe shown in Figure 3.10. Therefore, for

the following results, the systematic errors are taken care of by the measured temperature value minus the systematic error when analyzing the results.

The same work has been done to the other 20 thermocouples, and the results of three repeatability tests are shown in Table 3.4:

Table 3. 4 Uncertainty of each channel between iced water and boiling water calibration test for 20 thermocouples

Temperature difference in each channel (K)	Temperature difference in iced water test (K)	Temperature difference in boiling water test (K)
Thermocouple 1	0.5 ± 0.2	0.3 ± 0.3
Thermocouple 2	0.6 ± 0.0	1.0 ± 0.2
Thermocouple 3	0.6 ± 0.1	0.6 ± 0.4
Thermocouple 4	0.6 ± 0.3	0.4 ± 0.2
Thermocouple 5	0.7 ± 0.3	0.8 ± 0.2
Thermocouple 6	0.7 ± 0.1	0.3 ± 0.2
Thermocouple 7	0.9 ± 0.5	0.8 ± 0.2
Thermocouple 8	0.9 ± 0.4	0.9 ± 0.4
Thermocouple 9	0.9 ± 0.2	0.9 ± 0.4
Thermocouple 10	1.0 ± 0.1	0.8 ± 0.2
Thermocouple 11	0.9 ± 0.1	0.6 ± 0.4
Thermocouple 12	0.8 ± 0.4	0.7 ± 0.1
Thermocouple 13	0.8 ± 0.2	0.9 ± 0.1
Thermocouple 14	0.8 ± 0.4	0.4 ± 0.3
Thermocouple 15	0.9 ± 0.6	0.6 ± 0.1
Thermocouple 16	0.9 ± 0.4	0.8 ± 0.5
Thermocouple 17	0.9 ± 0.6	0.7 ± 0.4
Thermocouple 18	0.8 ± 0.4	0.8 ± 0.3
Thermocouple 19	0.7 ± 0.3	0.6 ± 0.2
Thermocouple 20	0.6 ± 0.2	0.9 ± 0.5

In the calibration test of thermocouple, the temperature differences between the thermocouple and accurate probe are not all the positive value, the K type thermocouple has the random error or uncertainty in temperature measurement as shown in Table 3.4. The maximum random uncertainties in iced bath and boiling water are 1.0±0.1 ^{o}C and 0.9±0.4 ^{o}C respectively. Therefore, the random error of thermocouples in this project is all within 1 ^{o}C.

3.4.2 Busbar preliminary test

Most of the solid conductors have high thermal conductivity, which means the temperature difference along the busbar is relatively small. In this project, the busbar material is copper, of which thermal conductivity is as large as 385 (W/(m·K)). Considering the amount of temperature measurement devices, a preliminary test has been done to define the amount and location of thermocouples placed along the busbar. The geometry of the overlapped busbars in our experimental setup is Figure 3.13:

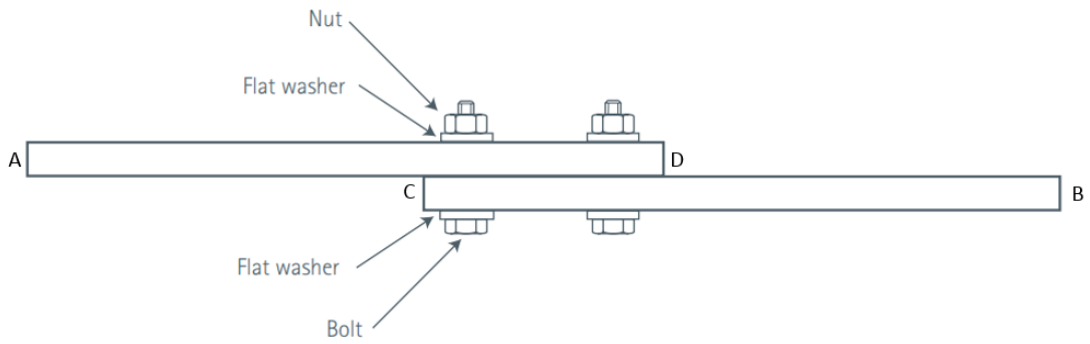

Fig. 3. 13 Configuration of busbar connection

The height of each busbar is only 1 cm, which is small as compared to the height of enclosure 30 cm. Therefore, this preliminary test is going to validate whether the overlapped busbar can be seen as a symmetric object in temperature-rise test. If it can be seen as a symmetric object geometry, the amount of thermocouples used along the busbar can be cut down to a half at least.

Therefore, the preliminary tests were carried out in three different loads, and fifteen thermocouples were placed along the distance between point A to point B. The point A is set as an origin point, and other places are described by the distance to point A. The whole length of line AB is 68 cm, so the A is described as 'L=0 cm', point B is described as 'L=68 cm'. The results of three different loads are shown in the Table 3.5:

Table 3. 5 Temperature-rise along the busbar calibration test

Position of thermocouple	Temperature-rise in 600A load current (K)	Temperature-rise in 700A load current (K)	Temperature-rise in 800A load current (K)
L=0 cm	14.4	20.6	26.1
L=5 cm	14.7	21.0	26.5
L=10 cm	14.9	21.2	26.9
L=15 cm	15.3	21.5	27.3
L=20 cm	15.5	21.9	27.8
L=25 cm	15.8	22.1	28.1
L=30 cm	15.9	22.4	28.4
L=34 cm	16.0	22.5	28.5
L=38 cm	15.9	22.5	28.4
L=43 cm	15.8	22.2	28.2
L=48 cm	15.6	22.0	27.8
L=53 cm	15.4	21.6	27.6
L=58 cm	15.0	21.2	27.1
L=63 cm	14.7	21.0	26.5
L=68 cm	14.6	20.8	26.2

The results measure temperature along busbar are shown in Figure 3.14:

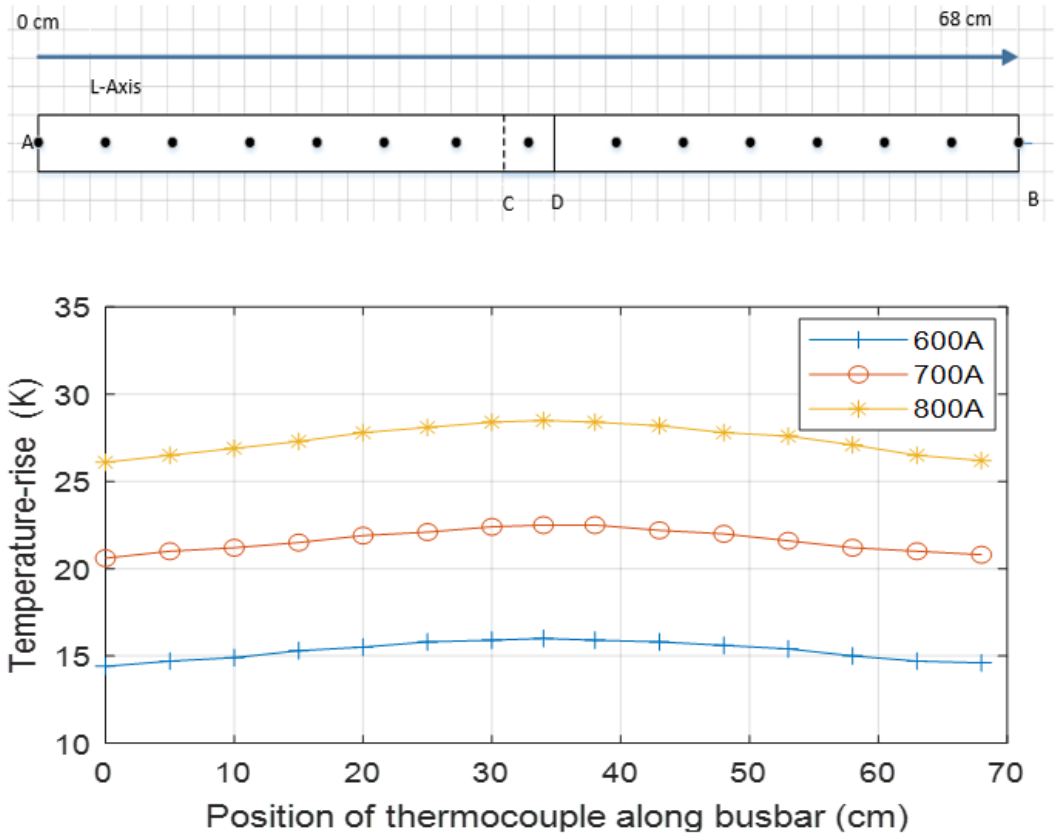

Fig. 3. 14 Temperature distribution along busbar

From Figure 3.14, it can be proved that the temperature variation along the overlapped busbar can be seen as mirror symmetric with the central line located at the middle of the length of the busbars. Considering IEC standard 60694 and the uncertainty of thermocouple, it is not necessary to place 15 thermocouples along the busbar, 5 thermocouples are chosen to be placed at a half of the busbar, which are placed at L=0 cm, 10 cm, 20 cm, 30 cm and 34 cm away from the A point.

3.5 Summary

CFD simulation will be verified by experiments to prove the principle used in thermal modelling, temperature management and optimisation of design. In this chapter, the individual components and the experimental setup were introduced. Calibration tests of thermocouples and data acquisition systems were carried out to define the

measurement accuracy. The experimental plan to identify the maximum temperature and air flow field was also discussed. This will help to study contact resistance mode in Chapter 4 and to validate the models in Chapter 5.

Chapter 4 Contact Resistance Model

As we understand, contact resistance at busbar joints tend to be higher and it makes the busbar joint hotter than busbar. C-M-Y model is chosen to calculate the contact resistance, which takes pressure, temperature and contact surface roughness into consideration. However, the validity of this C-M-Y model for our busbar connection needs to be assessed, especially the empirical parameters used in the model. For this verification purpose, there are two sets of experimental data obtained in the tests, the measured electrical resistance and temperature of busbar. The electrical resistance is mainly used to validate the temperature resistivity coefficient of the copper; and the C-M-Y's contact resistance model needs both the electrical resistance and temperature measured under several load currents. Of course, the temperature results are also used to validate the fully-coupled physical processes simulated by the computer model. They are also used to predict the maximum temperature in the busbar compartment model under different load currents.

4.1 C-M-Y model for busbar compartment model

The mathematical description of C-M-Y model is shown as in equation (2-6). In this thesis, the influence of temperature and contact pressure are wanted, and the electrical conductivity in contact surface $\sigma_{contact}$ is equal to the electrical conductivity of copper busbar, as the material of two sides of the contact surface is the same. Therefore, the equation of the contact resistance in this project of the overlapped busbar can be re-written as in equation (4-1):

$$R_i = \frac{1}{1.25\sigma_{contact}} \cdot \frac{\sigma_{asp}}{m_{asp}} \left(\frac{p}{H_c}\right)^{-0.95} \cdot \frac{1}{A} \qquad (4\text{-}1)$$

where: R_i (Ω) is the contact resistance, $\sigma_{contact}$ (S/m) is the electrical conductivity in contact surface, m_{asp} is the average slope of the microscopic asperities, σ_{asp} (m) is the

average height of the microscopic asperities, H_c (P_a) is the reference micro-hardness, always set as 3 GP_a, p (P_a) is the contact pressure applied on the surface, A (m^2) is the area of the contact surface.

The parameter σ_{asp} and m_{asp} of surface roughness are provided by the manufacturer report, as 80 μm and 0.4 respectively.

From the description of C-M-Y model, the temperature effect on the contact surface is dependent on the resistivity temperature coefficient of copper busbar. At the same time, the influence of contact pressure in C-M-Y model is defined by the experiment, the parameter -0.95 is averaged also from the empirical formula, reported in [35, 37, 38] based on the dimension of electronic heat sink. Therefore, before applying the C-M-Y model to govern the contact resistance in our thermal-flow study, the parameter should be validated by experiments.

4.2 Electrical resistance measurement and verification tests

To validate the C-M-Y model, two types of resistance need measuring, pure copper busbar resistance and the contact resistance. As shown in Figure 4.1, the resistance of a certain length of copper busbar is measured from point A to point C in Figure 4.1. These results are used to check the temperature coefficient of resistivity, which describes the relationship between electrical resistance and temperature. On the other hand, the contact resistance is measured from point C to point D, where is the overlapping area of the two busbars.

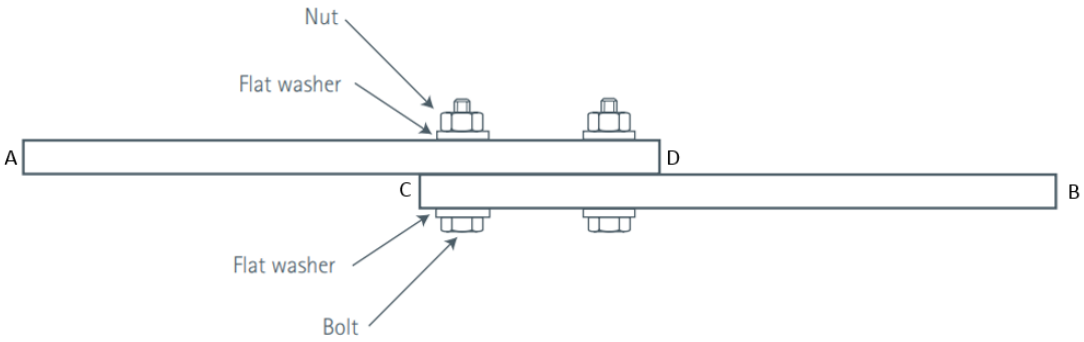

Fig. 4. 1 Side view of the simplified cabinet configuration

According to section 6.4 in IEC standard 60694, the method to measure the electrical resistance is described as: 'the measurement of the d.c. voltage drop or resistance shall be made before the temperature-rise test, with the switchgear and controlgear at the ambient air temperature and after the temperature-rise test when the switchgear and controlgear has cooled to a temperature equal to the ambient air temperature. The measured resistances in these two tests shall not differ by more than 20%'. This is important as temperature-rise tests should not make permanent changes of the properties of materials.

With respect to the accuracy of experimental results, the resistance measurement of copper busbar at different temperatures follows the instruction. Then, to obtain the resistivity temperature coefficient, the electrical resistance from point A to point C would be measured before and immediately after the temperature-rise experiments. For the resistance of contact area, it also needs measuring before and immediately after the experiments, to study temperature effect to contact resistance.

4.2.1 Circuit resistance

Considering the whole length of two busbars (750 mm) and resistivity of copper (1.72×10^{-8} Ω·m) at ambient temperature, the unit of resistance of the whole circuit is micro-ohm (μΩ). Therefore, the four-wire connection method is needed for precise

resistance measurement and Megger DLRO 600 Digital Microhmmeter was chosen to measure the resistance.

The four-wire (Kelvin) measurement method is preferred for resistance values below 100 μΩ, and Megger DLRO 600 uses this method as well. The Kelvin method of resistance measurement uses four separate wires. Two wires carry the current, known as the source or the current leads, and they pass the current through the conductor. The other two wires known as the sense or potential leads, are used to sense the voltage drop across the conductor. Whilst some small current will flow in the sense leads, it tends to be negligible and can be ignored, as illustrated in the manual instruction of Megger DLRO 600 machine [48]. The voltage drop across the ohmmeter's sense terminals is therefore virtually the same as the voltage drop across the conductor. This method of measurement will produce accurate and consistent results when measuring electrical resistances below 100 μΩ.

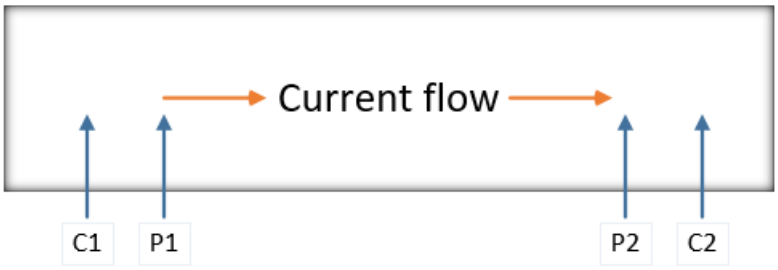

Fig. 4. 2 Four-wire measurement

In Figure 4.2 the connection of four separate wires, as two current (C1 and C2) and potential (P1 and P2) are shown. To ensure the high accuracy of resistance measurement, the current wires must be placed outside the potential wire.

For Megger DLRO 600, the method it used is four-wire method. The accuracy of voltage, current and resistance of DLRO 600 is shown in Table 4.1:

Table 4. 1 Accuracy of Megger DLRO 600

	Voltage	Current	Resistance
Accuracy	±0.5%±0.1 mv	±0.5%±0.1 A	Better than 1%

The uncertainty of 1% is acceptable in this project, because the whole resistance of two overlapped busbar is estimated as 20 μΩ, the influence of 1% uncertainty can be regarded as negligible.

4.2.2 Contact resistance

Referred from [28], the contact resistance is likely to bring extra resistance in the current loop. Therefore, the contact area always generates additional heat, and it is the most common hot spots in electrical apparatus. A suitable mathematical description of contact resistance must be validated, so it can be sure in the mathematical model to predict the hottest spots and the maximum temperature in the electrical device.

The contact resistance is affected by temperature, contact pressure and surface roughness. Due to the temperature range 20 ^{o}C to 90 ^{o}C in this thesis, the change caused by temperature can be negligible to the surface roughness. The influence of pressure and temperature was then studied and defined. For pressure, the contact resistance can be measured under different well-defined torque. As for temperature, the contact resistance will be measured immediately after temperature-rise test.

However, when current flows through a joint formed by two overlapping conductors, the lines of current flow are distorted and the effective resistance of the joint is increased since current only flows through a portion of the material.

Therefore, the resistance measured from point C to point D is not only the contact resistance, but also including the resistance of overlapped busbars. The geometry of overlapping area is shown Figure 4.3:

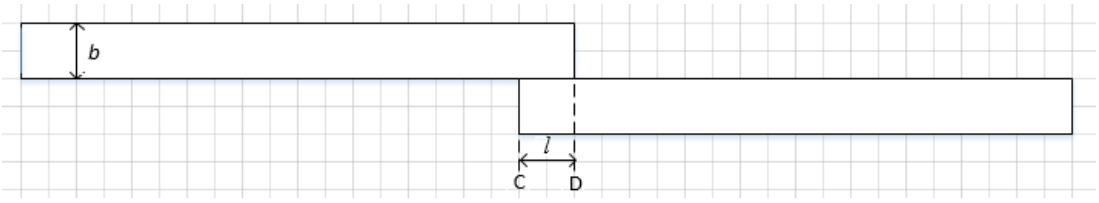

Fig. 4. 3 Configuration of overlapping busbar

Reported in the handbook 'Copper for busbars' [49], the resistance of the joint measured is a combination of two resistances:

$$R_j = R_s + R_i \tag{4- 2}$$

where R_j (Ω) is the resistance measured of the conductor from point C and D; R_s (Ω) is the streamline effect or spreading resistance, due to diversion of the current flow through the contact area; R_i (Ω) is the contact resistance of the joint.

In [49] and [50], it was proven that the streamline effect is dependent only on the ratio of the length of the overlap l to the thickness of the busbars b, and not on the width, and the relationship is shown in Figure 4.4:

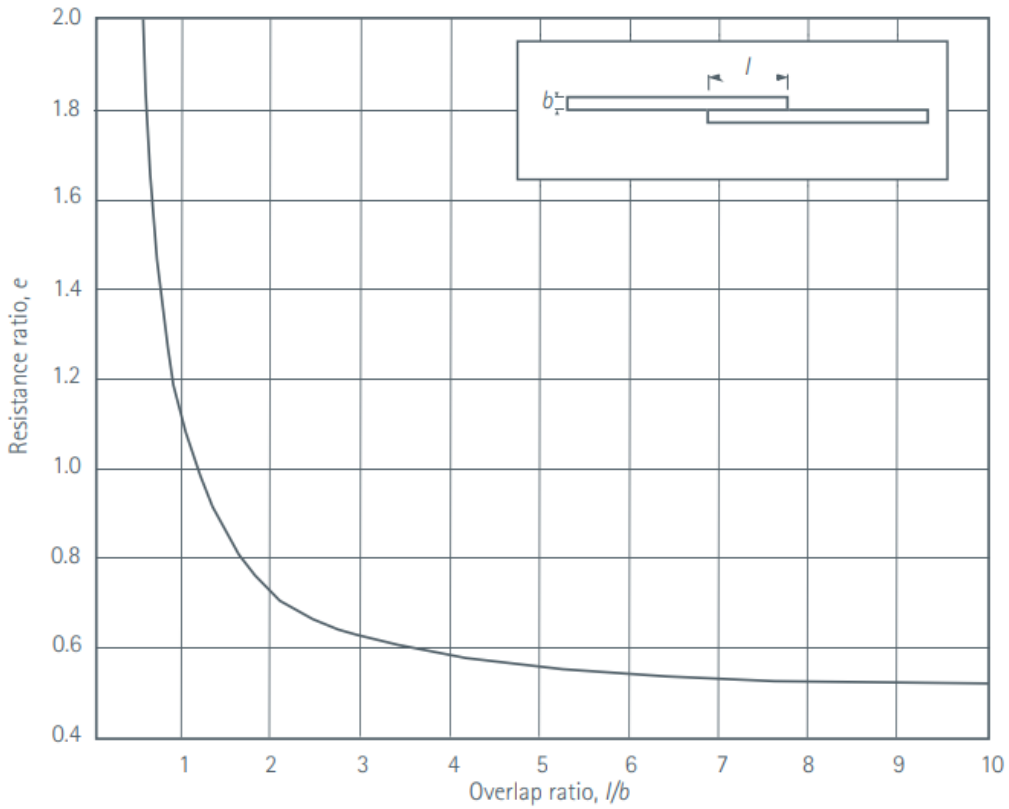

Fig. 4. 4 Relationship of resistance ratio[49]

The resistance ratio e, in Figure 4.4 is the ratio of the resistance of a joint due to streamline effect R_s, to the resistance of an equal length of single conductor R_b, and the equation is:

$$e = \frac{R_s}{R_b} = \frac{ab}{\rho l} R_s \tag{4- 3}$$

where a (m) is the width of busbar, b (m) is the thickness of busbar, l (m) is the length of overlap, ρ (Ω·m) is the resistivity of the conductor, R_s (Ω) is the resistance of the overlap section. It is also reported in [49], the spreading resistance can be calculated in equation (4-4) when the connection bolts dramatically reduce the efficiency of streamline effect:

$$R_s = \frac{\rho l}{(a-nd)b} e \quad (4\text{-}4)$$

where d (m) is the diameter of the hole for bolt connection, n is the number of bolts across the width of busbar.

By equations (4-2) to (4-4), we can easily calculate the contact resistance R_i, and find out the accurate contact resistance under different conditions.

4.3 Validation of contact resistance model

4.3.1 Resistivity temperature coefficient

The resistance of the busbar was measured from point A to point C in Figure 4.1 by Megger DL600 as shown in Figure 4.2 under different load currents, and the temperature of copper busbar was also measured and recorded under different load currents. Both the electrical resistance and the temperature-rise results by measurement are shown in Table 4. 2:

Table 4. 2 Electrical resistance of busbar under various load current

Load current (A)	Average temperature of busbar (°C)	Resistance of busbar (μΩ)
0	20.00	8.1
600	35.20	8.5
700	41.55	8.8
800	47.35	8.9
900	53.70	9.1
1200	75.90	9.8

Then the resistivity of copper busbar is calculated, and the copper electrical resistivity versus temperature is also drawn in Figure 4.5:

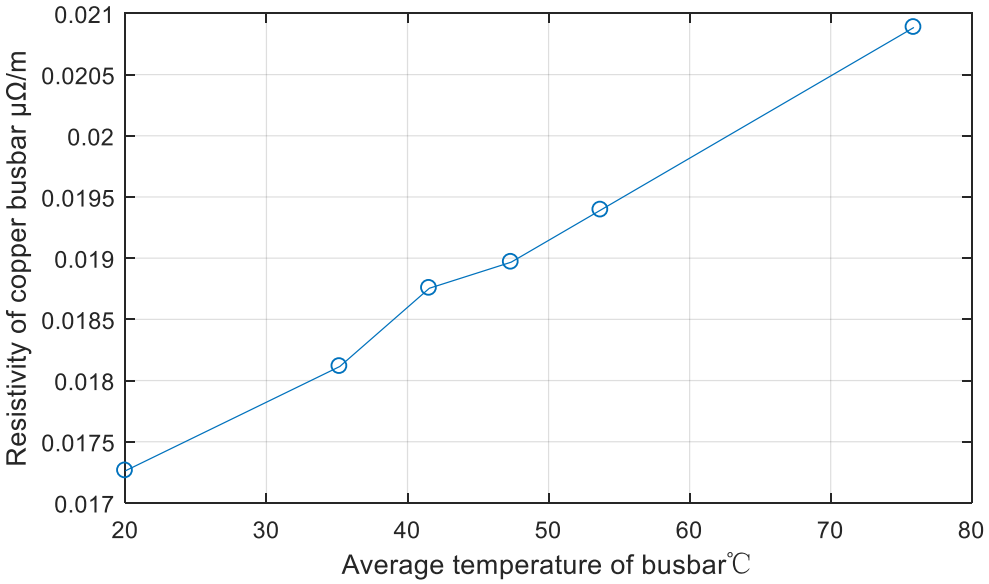

Fig. 4. 5 Electrical resistivity of busbar versus average temperature

There is a small deviation at 700 A load current from the linear trend of resistance versus average temperature of busbar as shown in Figure 4.5, and it might be influenced by the resolution of Megger DL600 as well as the uncertainty of thermocouple.

However, it can be derived that the copper temperature resistivity coefficient of our copper busbar is estimated as 0.00361. To reduce the random errors in the experiments, this test was repeated three times, and the estimated value of resistivity temperature coefficient is shown respectively as 0.0036, 0.0044 and 0.0049, and the average value is 0.0043±0.0008, which matches the value as 0.00396 reported in [26].

4.3.2 C-M-Y model

For the first factor, i.e. temperature, the C-M-Y model describes its effect on the contact resistance as the same as the resistivity temperature coefficient of conductor material.

In the experiment, the contact resistance was measured from point C and D in Figure 4.1, and the temperature was also measured by placing a thermocouple in a drilled hole inner one of the busbar right on the contact area. The spreading resistance R_s was described in equation (4-3) and equation (4-4) and the ratio in Figure 4.3, hence the contact resistance can be determined by these equations and all measured and calculated results are given in Table 4.3:

Table 4. 3 Calculated contact resistance of busbar

Load Current (A)	Measured temperature of contact area (°C)	Measured resistance R_j (μΩ)	Calculated spreading resistance R_s (μΩ)	Calculated contact resistance R_i (μΩ)
0	20.0	2.8	3.79	-0.99
600	36.0	3.0	4.02	-1.02
700	42.5	3.0	4.13	-1.13
800	48.6	3.1	4.21	-1.11
900	54.8	3.2	4.28	-1.08
1200	78.2	3.4	4.62	-1.22

However, the value of contact resistance cannot be minus. This shows that the empirical equation (4-5) is not applicable in our busbar model. As indicated in Figure 4.6, neglecting all the area in dashed, equation (4-5) is too severe in eliminating the area current can flow and hence overestimates the spreading resistance. To compensate this severe overestimation, in our study, the spreading resistance is calculated as inversely proportional to the value of spreading resistance in equation (4-4) by the ratio of copper areas with and without the four bolts. Therefore, the spreading equation can be calculated as shown in equation (4-5):

$$R_s = \frac{\rho l}{ab} e \cdot \frac{al}{al - n\pi(\frac{d}{2})^2} \quad (4\text{-}5)$$

where a (m) is the width of busbar as 0.0065 m, b (m) is the thickness of busbar as 0.01 m, l (m) is the length of overlap area as 0.07 m, ρ (Ω·m) is the resistivity of the conductor as 1.72×10^{-8} (Ω·m), R_s (μΩ) is the spreading resistance of the overlap

section, d (m) is the diameter of connection bolt as 0.024 m, and n is the number of the connection bolts as 4.

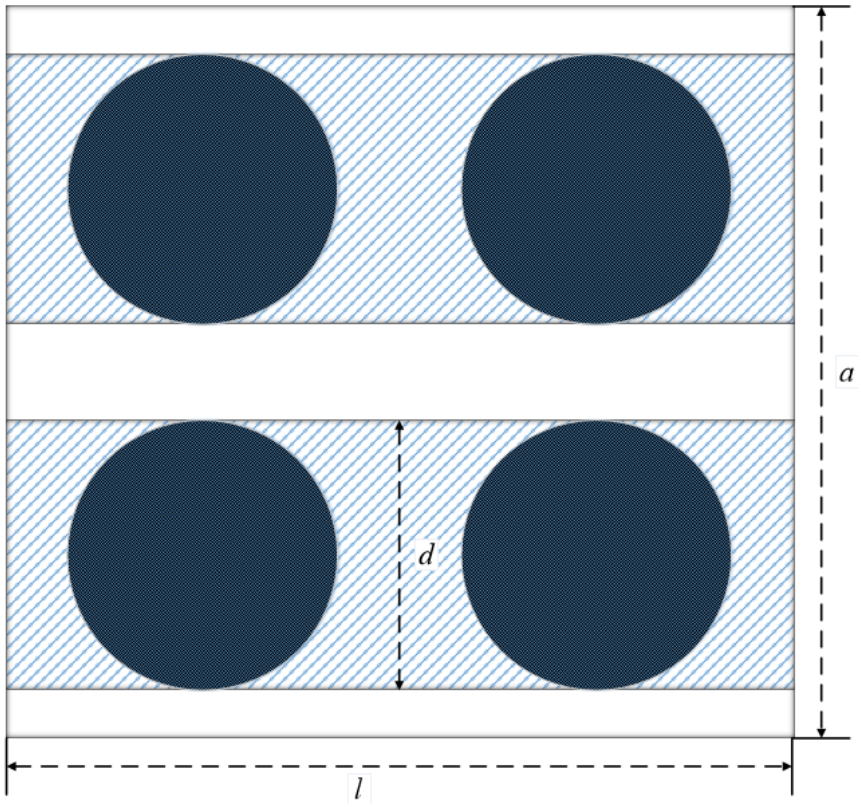

Fig. 4. 6 Top view of bolt joint

Then the value of spreading resistance from equation (4-5) and the calculated contact resistance are shown in Table 4.4:

Table 4. 4 Calculated contact resistance of busbar under different load current

Load Current (A)	Measured temperature of contact area (°C)	Measured resistance R_j (μΩ)	Calculated spreading resistance R_s (μΩ)	Calculated contact resistance R_i (μΩ)
0	20.0	2.8	1.69	1.11
600	36.0	3.0	1.80	1.20
700	42.5	3.0	1.84	1.16
800	48.6	3.1	1.88	1.22
900	54.8	3.2	1.92	1.28
1200	78.2	3.4	2.07	1.33

The fitted linear curved for these six values of contact resistance yields the slope calculated as 0.0044. There is a small deviation at 800 A and 900 A load current from the linear trend of resistance versus average temperature of busbar joint, and it might be influenced by the resolution of Megger DL600 as well as the uncertainty of thermocouple. To reduce the random errors in the experiment, the test was repeated three times, and the estimated value of temperature resistivity coefficient of contact area is shown respectively as 0.0044, 0.0049 and 0.0042. The average value was calculated as 0.0045±0.0004, which matches the value 0.0043±0.0008 in section 4.3.1.

For the second factor, the contact pressure, it could be controlled by controlling the torque applied when tightening the bolts in our experiment. The sensitivity study of the contact pressure was done under zero load current, which means the ambient temperature was assumed to be a constant. The torque applied on the bolts was changed from 40 Nm to 80 Nm, the repeatability tests were done three times, and the results of contact resistance are shown in Table 4.5.

The contact pressure is calculated as:

$$p = \frac{T_q \cdot n}{K \cdot d \cdot S} \quad (4\text{-}6)$$

where p (P_a) is the contact pressure of overlapping area, T_q (Nm) is the torque applied, n is the number of bolt used in the overlapping area as 4, K is the nut factor as 0.20, S (m^2) is the nominal area of overlapping surface as 0.0046 m^2, d (m) is the diameter of connection bolt as 0.024 m.

Table 4. 5 Calculated contact resistance of busbar under different torque

Torque applied on bolts (Nm)	Calculated pressure on contact surface (MP_a)	Measured resistance R_j (μΩ)	Calculated spreading resistance R_s (μΩ)	Calculated contact resistance R_i (μΩ)
40	7.3	4.3±0.4	1.69	2.61±0.4
50	9.2	3.8±0.2	1.69	2.11±0.2
60	11.0	3.4±0.1	1.69	1.71±0.1
70	12.8	3.0±0.1	1.69	1.31±0.1
80	14.7	2.8±0.0	1.69	1.11±0.0

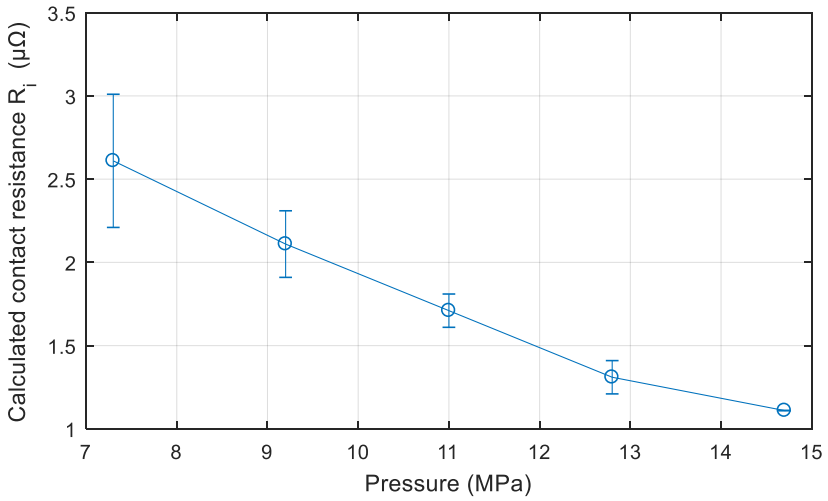

Fig. 4. 7 Contact resistance versus pressure applied on contact area

The fitted cured for these five values of contact resistance yields the equation as:

$$R_i = 28.17 \times (p)^{-1.186} \quad (4\text{- }7)$$

The factor of contact pressure is estimated as -1.186, is different to the value of -0.95 given in C-M-Y contact resistance model.

Therefore, the comparison of contact resistance calculated between C-M-Y model and experimental results are shown in Table 4.6:

Table 4. 6 Comparison of contact resistance between experiment and C-M-Y model

Torque applied on bolts (Nm)	Calculated pressure on the contact surface (MP_a)	Contact resistance R_i of C-M-Y model (μΩ)	Contact resistance R_i of Experiment (μΩ)
40	7.3	2.24	2.61±0.4
50	9.2	1.80	2.11±0.2
60	11	1.51	1.71±0.1
70	12.8	1.31	1.31±0.1
80	14.7	1.15	1.11±0.0

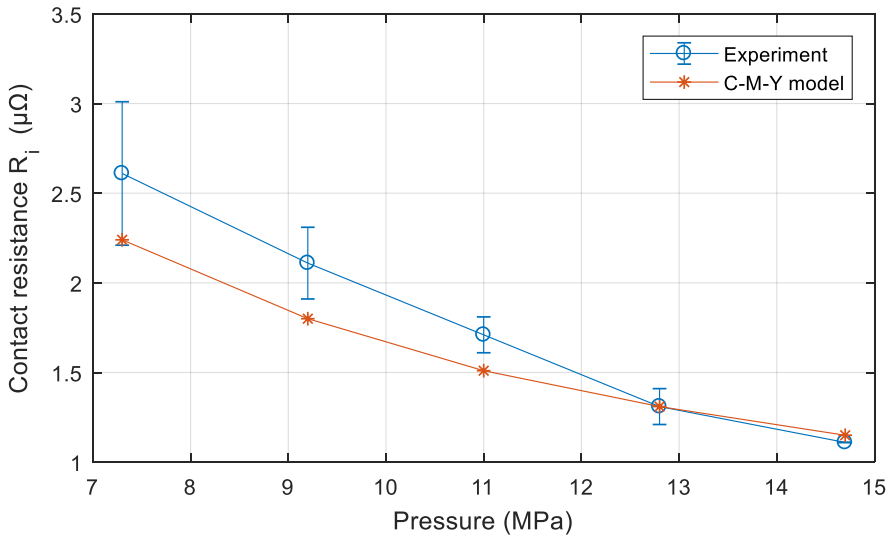

Fig. 4. 8 Contact resistance versus pressure in C-M-Y model and experiment

In Figure 4.8, the results of calculations and experiment show an agreement in the high level of contact pressure. The low pressure applied does not provide a uniform distribution of real contact area, as 'A-spots', on the contact surface. The torque

applied in this report was always set as 80 Nm, and the modified C-M-Y model was then used in the thermal-flow studies in CFD software COMSOL.

4.4 Summary

To predict the maximum temperature in busbar compartment, the busbar joint area is more important, as the contact resistance generates more Joule heating than any other places. In this chapter, the C-M-Y model, which is widely used to calculate the contact resistance, was validated by experimental tests and measurements. The empirical parameters of the model were re-evaluated for our busbar compartment model. This modified C-M-Y model was then used in the thermal-flow field simulation work, which can help provide an accurate prediction of the maximum temperature in the CFD simulation in Chapter 5.

Chapter 5 CFD Models and Experimental Validation

Computer aided design based on differential CFD models not only provides vital details to understand the mechanisms involved in the operation but also enable more rapid and cost-effective prototyping of switching cabinet product. However, simulation models and their results need to be validated by experiments and tests. In this chapter, mesh refinement study was first carried out to gain the understanding of the influence of mesh size. Boundary conditions are then defined for our busbar compartment model. Simulation results of the model with properly chosen mesh system and boundary conditions are finally compared with experimental results under different load currents.

5.1 Convergence

The governing equations for fluid flow are set as Navier-Stokes equations, which are nonlinear equations. The equations are solved by imposing restrictive conditions, as boundary condition. In computational fluid dynamics (CFD), the solution must be calculated iteratively. Convergence is thus vitally important to the numerical solution.

Residue, which directly quantifies the error in the solution of the system of equations, is one of the most fundamental and important factors to reflect the convergence of an iterative solution. In the CFD analysis, the residual measures the local imbalance of a conserved variable in each individual mesh element. However, in an iterative numerical solution, the residual will never be exactly zero. The lower the residual value is, the more numerically accurate the solution is. In CFD study, RMS (root mean square) residual levels of 10^{-4} are regarded loosely as converged, levels of 10^{-5} are

considered to be well converged, and levels of 10^{-6} are considered to be tightly converged. Therefore, the residual in COMSOL is set as 10^{-6} in this project.

Nevertheless, a smaller value of residual would cost a longer time in the numerical calculation. To help speed up the calculation, a suitable initial value needs to be found. As we all know, obtaining the final thermal-flow field in a real-world scenario is extremely hard from setting an initial value of zero of all quantities. Fortunately, COMSOL allows the result from last iteration step to be set as the initial value for next calculation step. By this, we could give a smaller input to a random factor, such as temperature boundary, load current or gravity force to make the solution convergent easily first, and then gradually increase this factor to the real value. By tests, choosing the factor of gravity has the same simulation results with choosing the temperature or current, but it saves more time. Due to the incremental change caused by slight increase of gravity force, the solution can reach the final steady-state results by stationary solver in COMSOL.

However, the method above still needs many iteration steps to reach the final desired results, and each simulation of the busbar compartment model under different scenarios would take one or two weeks. Therefore, the time-dependent solver is used to improve the previous methods. The time-dependent solver is easier to find a solution than stationary-solver in CFD, and it can speed up calculation process when the final solution does not change with time step.

Therefore, the final simulation strategy we used was to use the stationary solver to obtain a solution with smaller gravity force input, and then this result from the stationary solver can be set as the initial value for the time-dependent solver. Then, we gradually increased the gravity force to the real value we want and give an enough timescale. This calculation process would only take two to three days, and convergence of numerical solution is validated by the key quantities in thermal-flow field in our busbar compartment model, i.e. maximum temperature and air velocity.

5.2 Mesh refinement study

COMSOL is used to build predictive computational models of real-world scenarios. The accuracy of the prediction of real-world behaviour which can be obtained from Finite Element Analysis model is directly related to the finite element mesh that is used. Defined by each individual element mesh, a set of governing equations, are solved in each element. When these elements are made smaller and smaller, as the mesh is refined, the computed solution will approach the true solution.

However, due to the limitation of computational resource and time consumption, infinite number of refined mesh elements are not feasible nor recommended, a mesh refinement study is therefore carried out, which means an optimal number of mesh elements will be found to obtain an appropriate result with the minimum computational cost. Thus, the process of mesh refinement study is a key step in validating any finite element model and gaining confidence in the software, the model and the results [51].

5.2.1 Mesh pattern

As previously explained in section 2.5, the mesh pattern is designed individually for different physical processes. Considering the heat generation and dissipation processes in the busbar compartment model, the mesh pattern consists of three domains or areas, i.e. busbars, thermal boundary layer and air.

In busbar domain, the temperature gradient inside the busbars is small because the thermal conductivity of copper is as large as 385 (W/(m·K)). Only the tetrahedral elements are applied in the busbar domain, whilst a few tetrahedral elements could stretch well in corner or curved places, the simulation results would not be affected due to small temperature gradient inside the busbars. The proportion of the elements in busbar domain to the whole amount of mesh elements in the system is 5%.

As for the thermal boundary on the surface of busbar or enclosure, it is assumed that the heat transfer right on these surfaces are in one direction by thermal conduction. Therefore, the thin 3D prism elements with quadrilateral base and 2D quadrilateral elements are placed right on the surface for two layers, which are used to make numerical solution easily calculate the massive heat transferred, and the number of the prism element layer was tested and shown they would not affect the simulation results. In the corner, the triangle elements are used to fit the curved places. The proportion of elements used in the thermal layer to the total amount is 8%.

The rest is the air domain, which has a much bigger space than the other two areas. The temperature gradient is expected to be smaller than that in the thermal boundary layer. However, the velocity of air may have small fluctuation with time even when the system is overall in steady-state in reality. By testing, the air domain is mainly filled with tetrahedral elements, the difference to busbar domain is the mesh elements in curved or corner space would affect the flow field and velocity distribution, so very few pyramid and prism elements were used in this area. The proportion of the elements in air domain of the total amount is 87%.

In conclusion, the mesh pattern for the busbar compartment model was designed as shown in Figure 5.1:

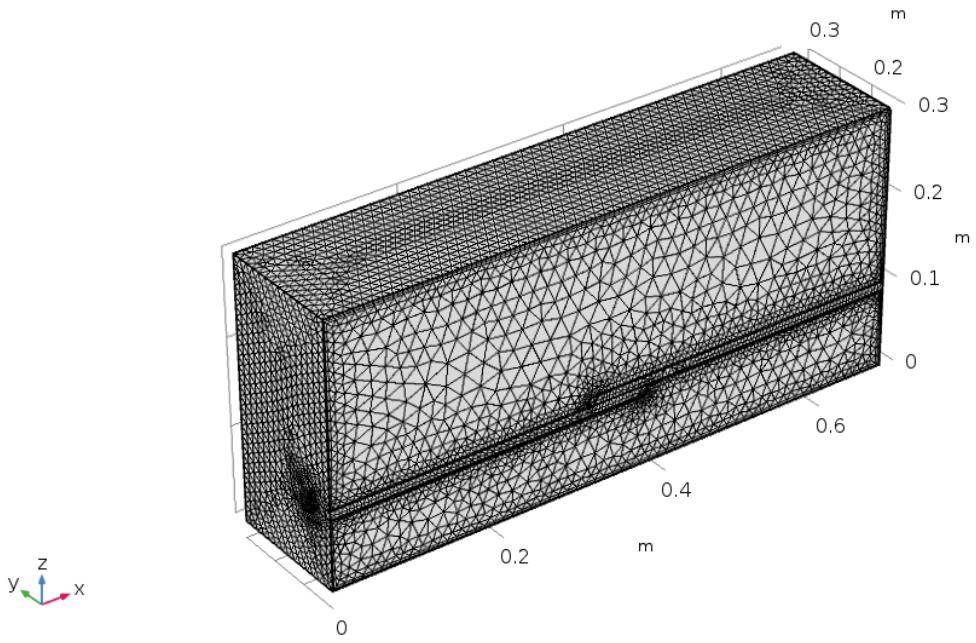

Fig. 5. 1 Mesh pattern of busbar compartment model

In the next step of mesh refinement study, only the mesh amount would increase, and the proportion of each domain or area is the same.

5.2.2 Mesh element amount

Based on this mesh pattern, mesh refinement is done by changing the total amount of mesh elements.

With previous experience on COMSOL, it is recommended that the analysis using a FEA model in COMSOL should begin with a preliminary mesh. The preliminary mesh should be coarse, meaning the mesh cell would be relatively large. This first coarse mesh needs a small amount of computational resource and less computing time. Although the coarse mesh may give less accurate results, the results could be used as an initial value for the subsequent calculation. In addition, it also provides a rough understanding and verification on the applied condition. After computing the physical process in a coarse mesh, the process of refinement will begin. With the increase of mesh elements in the same domain, different results obtained by different mesh

systems will be compared. This comparison is most done by analysing the main physical quantities in the crucial domain, field or boundary. By comparing these scalar quantities, it is possible to judge the influence of mesh size and convergence of the solution with respect to mesh refinement. After comparing a minimum of three successive solutions, an asymptotic behaviour of the solution starts to emerge, which means the changes in the solution between meshes become smaller. Eventually, these changes will be small enough that the uncertainty from numerical calculation is regarded as acceptable [38].

In our case, the minimum amount of meshing element in 'prismatic layer' mesh pattern is chosen to be 20000, and the maximum amount is 700000 which reaches the limit of the computational resource as 64G. From 20000 to 700000, there are 6 mesh systems, whilst the proportion or the ratio of the elements distributed in different areas in the domain system is the same. These 6 different amounts of mesh elements are named as extra coarse mesh, coarser mesh, coarse mesh, less coarse mesh, normal mesh, fine mesh respectively. The different mesh amounts are shown in Table 5.1:

Table 5. 1 Different mesh systems

Mesh system	Extra coarse	Coarser	Coarse	Less coarse	Normal	Fine
Mesh element	29315	61115	162488	246930	304688	709027

The extra coarse mesh pattern and fine mesh pattern are shown in Figures 5.2 and Figure 5.3 respectively,

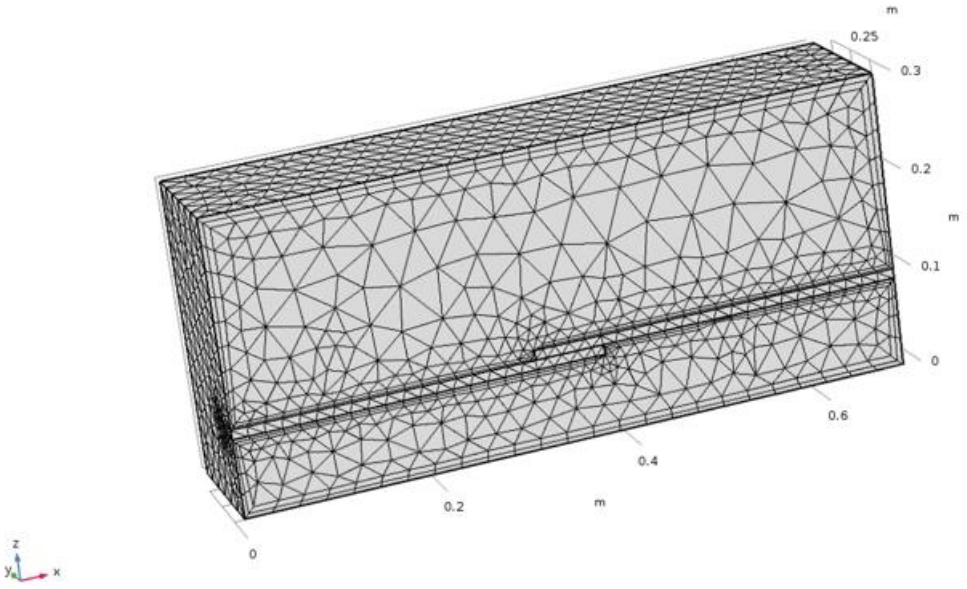

Fig. 5. 2 Extra coarse mesh system

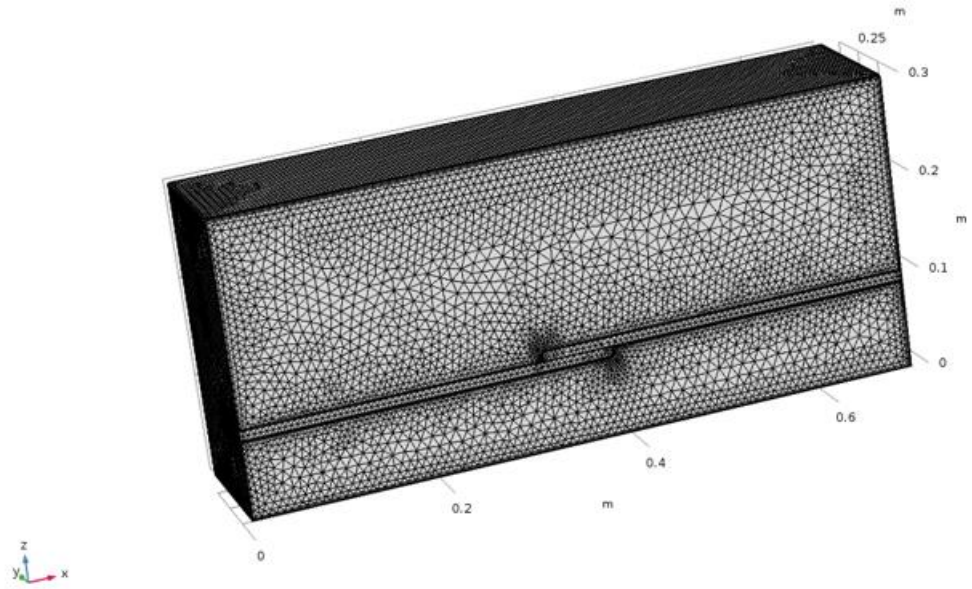

Fig. 5. 3 Fine mesh system

As seen above, the fine mesh system provides a much higher spatial resolution than the extra coarse mesh system. The mesh is fine enough when the main quantities, in crucial area and on boundaries does not change much with the increase of mesh elements.

In our model, the thermal-flow field is represented by temperature, velocity and thermal boundary layer. Reported in [51], the results from mesh refinement study should be compared to conclude on the adequacy of the mesh system. In our case, the quantities are focused on the contact surface temperature, air velocity distribution of the middle y-z plane, the thickness of thermal boundary layer and the average temperature of top boundary solid wall. In this project, although each individual case was studied with respect to mesh refinement (technically it may not be necessary although natural convection in air under different temperature could result in some differences, for this it would be left in the future work area to discuss), only the 800 A load current is taken as an demonstrating example in this section.

Over the whole domain, contact surface is the hottest in the system due to electrical heating. The maximum temperature-rises on the contact surface for different mesh systems are compared, as shown in Table 5.2 and Figure 5.4:

Table 5. 2 Maximum temperature on the busbar contact surface at 800 A load current

Mesh type	Mesh element	Maximum temperature-rise (K)
Extra coarse	29315	26.67
Coarser	61115	27.25
Coarse	162488	28.17
Less coarse	246930	28.57
Normal	304688	28.58
Fine	709027	28.60

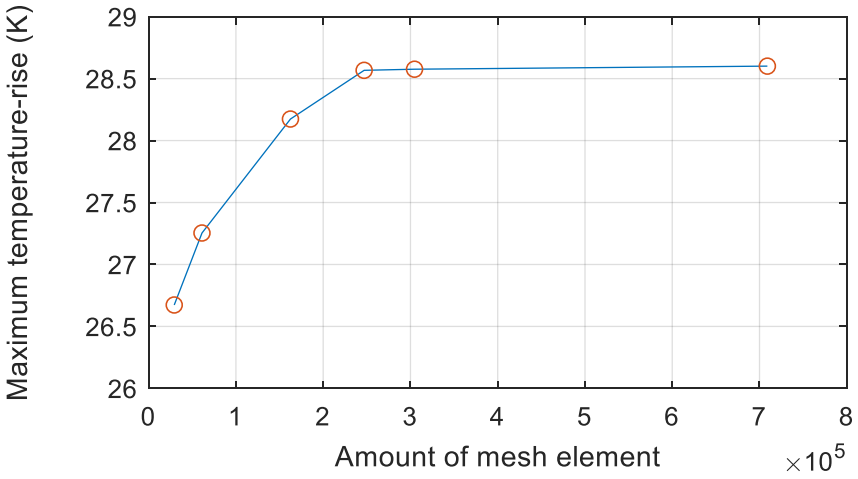

Fig. 5. 4 Maximum temperature on the busbar contact surface at 800 A load current

The next key quantity of the thermal-flow field for comparison is the velocity of air flow. From the numerical results, the air velocity on the middle y-z plane is the largest, as the air absorbs more energy from the contact resistance's Joule heating. The numerical results of the maximum air velocity in the middle plane are shown in Table 5.3 and Figure 5.5:

Table 5. 3 Maximum air velocity in the middle y-z plane at 800 A load current

Mesh type	Mesh element	Maximum velocity of air (m⁄s)
Extra coarse	29315	0.128
Coarser	61115	0.139
Coarse	162488	0.151
Less coarse	246930	0.163
Normal	304688	0.167
Fine	709027	0.168

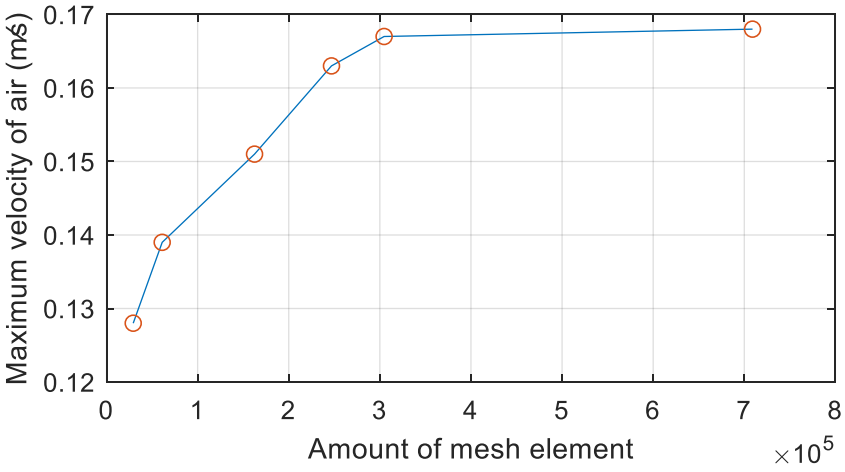

Fig. 5. 5 Maximum air velocity in middle y-z plane at 800 A load current

The third comparison is focused on the thickness of thermal boundary layer. From the layer concept, the temperature will drop dramatically in this layer, and an accurate prediction of this layer enables us to obtain an accurate flow field. The thickness of thermal boundary layer is calculated as [40]:

$$\delta = \frac{5 \cdot L}{\sqrt{R_e}} \tag{5-1}$$

where δ (m) is the thickness of thermal boundary of laminar flow, L (m) is the characteristic linear dimension to each geometry, and it is no more than the distance from upper busbar surface to top enclosure wall as 20 cm in this case, R_e is Reynolds number introduced in section 2.3. By previous calculation of R_e, the thickness of thermal boundary layer was estimated no more than 10 mm.

The length of the layer and 2D plot of temperature and velocity field are shown in Table 5.4 and Figure 5.6 and 5.7.

Table 5. 4 Length of thermal boundary layer right above busbar contact at 800 A load current

Mesh type	Mesh element	Length of thermal boundary layer (mm)
Extra coarse	29315	1.25
Coarser	61115	1.20
Coarse	162488	1.18
Less coarse	246930	1.18
Normal	304688	1.18
Fine	709027	1.18

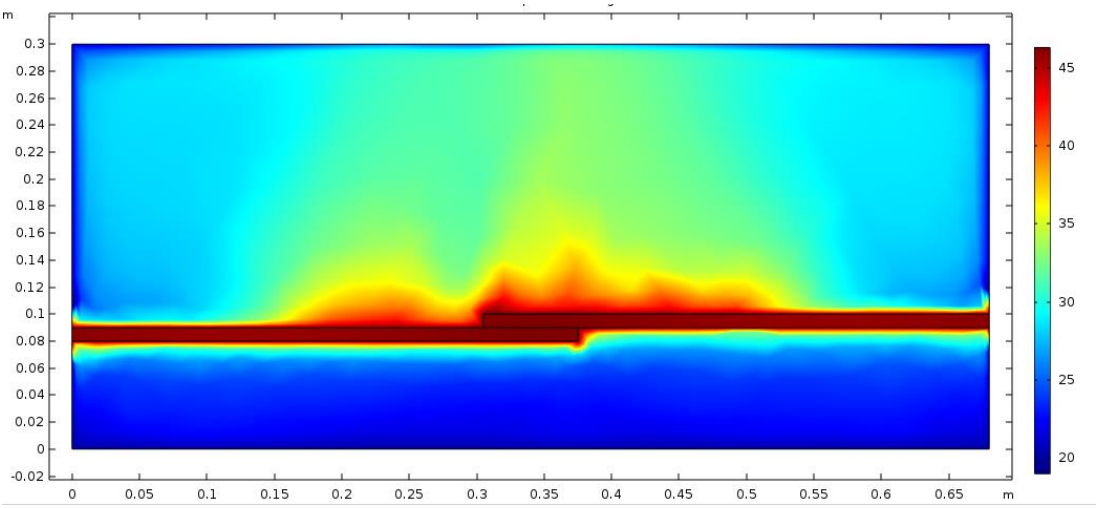

Fig. 5. 6 Temperature distribution (°C) in the middle x-z plane in extra coarse mesh system at 800 A load current

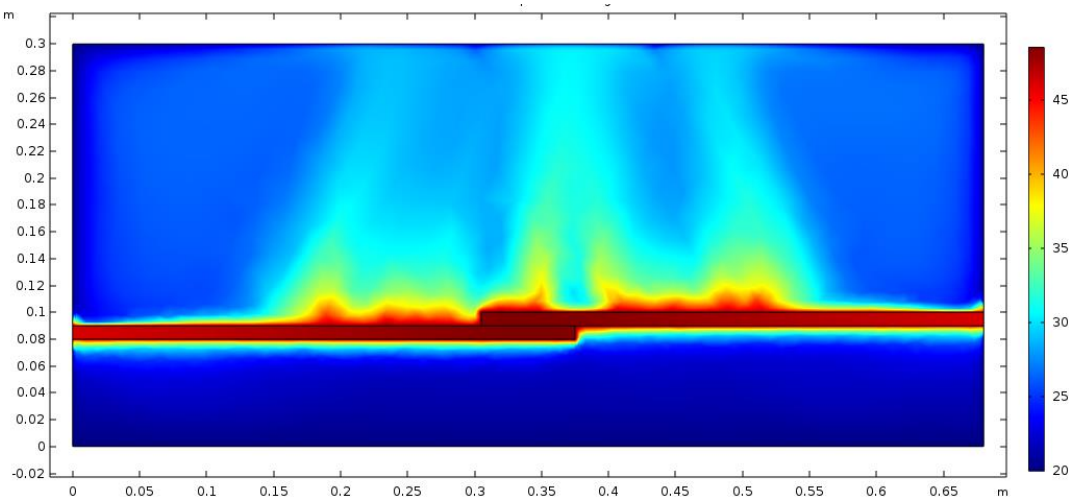

Fig. 5. 7 Temperature distribution (°C) in the middle x-z plane in less coarse mesh system at 800 A load current

The thermal boundary layer is defined as an area with great temperature drop gradient right on the busbar surface. Therefore, from the results of these six mesh systems, it is concluded that the less coarse system (element amount 246930) can provide a sufficiently high spatial resolution with the minimum mesh elements.

The last comparison is focused on the average temperature of the top enclosure wall. As the top wall of the enclosure has a temperature higher than any other side wall, the average value of its temperature is taken as an auxiliary quantity to validate the results of mesh refinement study. The temperature results are shown in Table 5.5 and Figure 5.8.

Table 5. 5 Average temperature of top enclosure wall at 800 A load current

Mesh type	Mesh element	Average temperature of solid enclosure top wall (°C)
Extra coarse	29315	23.06
Coarser	61115	22.76
Coarse	162488	22.41
Less coarse	246930	22.19
Normal	304688	22.18
Fine	709027	22.18

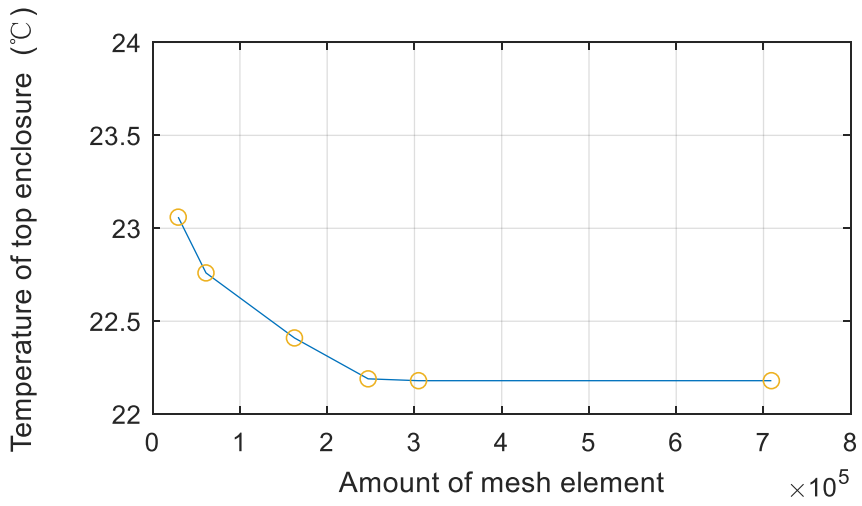

Fig. 5. 8 Average temperature of top enclosure wall at 800 A load current

In conclusion, the less coarse mesh system with element number of 246930 was selected as the suitable mesh system for the 800 A load current, taking all the above factors into consideration. In this mesh system, the average mesh size for thermal boundary layer was 0.002235 m^3, whilst the average size of mesh element in the air flow was 0.02812 m^3.

In the subsequent mesh refinement studies for other load currents, the main factors, as the maximum temperature of contact surface and the y-z plane air velocity, are used as criteria to choose the optimal amounts of mesh elements. By mesh refinement study for different load current range between 600 A to 1200 A, the less coarse mesh system was assessed as the suitable mesh system.

5.3 Experimental results

The experimental results obtained from the setup, which was described in Chapter 3, are shown in this section. The temperature-rise were measured on busbar surface,

air flow and enclosure walls under 600 A, 800 A and 1200 A load current. All the tests under each individual current were repeated three times.

As explained in section 3.3.2, the temperatures measured along busbar were taken in five points, and each point is described by the distance to origin point A, as shown in Figure 3.11. The temperature-rise result of busbar are shown in Table 5.6 and Figure 5.9.

Table 5. 6 Busbar temperature-rise measured under different load currents

Temperature-rise (K) / Points along busbar	600 A load current Experiment	800 A load current Experiment	1200 A load current Experiment
$l = 0\ cm$	14.4 ± 0.4	26.1 ± 0.4	53.4 ± 0.7
$l = 10\ cm$	15.0 ± 0.3	27.0 ± 0.3	54.9 ± 0.8
$l = 20\ cm$	15.5 ± 0.3	27.8 ± 0.4	56.7 ± 0.8
$l = 30\ cm$	16.0 ± 0.6	28.6 ± 0.8	57.8 ± 0.6
$l = 34\ cm$	16.4 ± 0.8	28.7 ± 0.6	58.2 ± 0.5

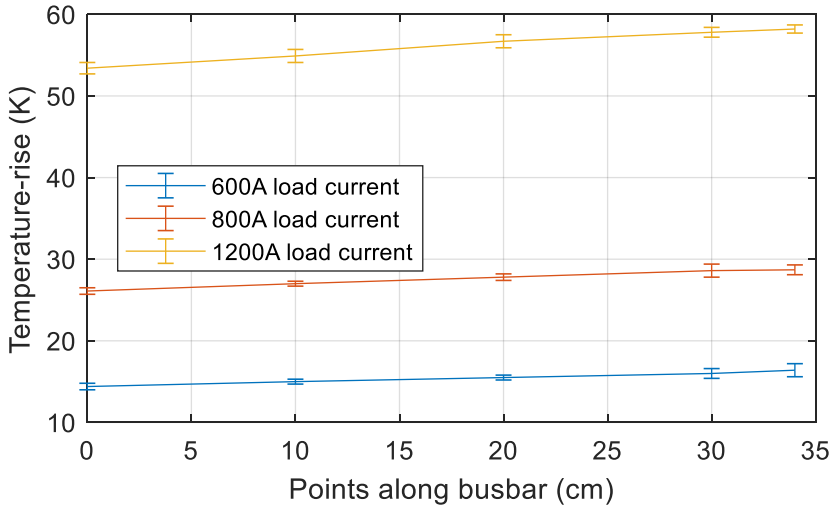

Fig. 5. 9 Busbar temperature-rise measured under different load currents

As stated in section 3.2, the temperatures were measured at points I_1 to E to represent the temperature distribution in air, and points G_1 to F, to represent the temperature distribution along enclosure wall. The experimental results obtained were shown in Table 5.7, Figure 5.10 and Table 5.8.

Table 5. 7 Air temperature-rise measured under different load currents

Temperature-rise (K) / Key points in air fluid	600 A load current Experiment	800 A load current Experiment	1200 A load current Experiment
$I_1(0.34,0.15,0.105)$	11.9 ± 0.6	20.5 ± 1.1	42.2 ± 1.9
$I_2(0.34,0.15,0.110)$	9.4 ± 0.5	16.4 ± 0.6	33.8 ± 1.7
$I_3(0.34,0.15,0.115)$	8.1 ± 0.8	14.2 ± 0.8	31.2 ± 1.6
$I_4(0.34,0.15,0.120)$	7.8 ± 0.4	13.9 ± 1.0	29.1 ± 1.4
$I_5(0.34,0.15,0.125)$	7.6 ± 0.6	13.5 ± 0.9	28.6 ± 1.8
$I_6(0.34,0.15,0.130)$	7.4 ± 0.2	12.8 ± 0.6	27.8 ± 1.5
$E_1(0.34,0.15,0.160)$	4.9 ± 0.4	10.1 ± 0.8	25.6 ± 1.6
$E_2(0.34,0.15,0.190)$	3.9 ± 0.6	8.4 ± 0.4	20.3 ± 1.2
$E_3(0.34,0.15,0.220)$	3.7 ± 0.4	7.9 ± 0.6	18.1 ± 0.9

$E_4(0.34,0.15,0.250)$	3.6 ± 0.8	7.1 ± 0.5	16.8 ± 1.4
$E_5(0.34,0.15,0.280)$	3.2 ± 0.2	6.8 ± 0.7	15.9 ± 1.1
$E(0.34,0.15,0.300)$	3.1 ± 0.4	4.1 ± 0.6	7.4 ± 0.8

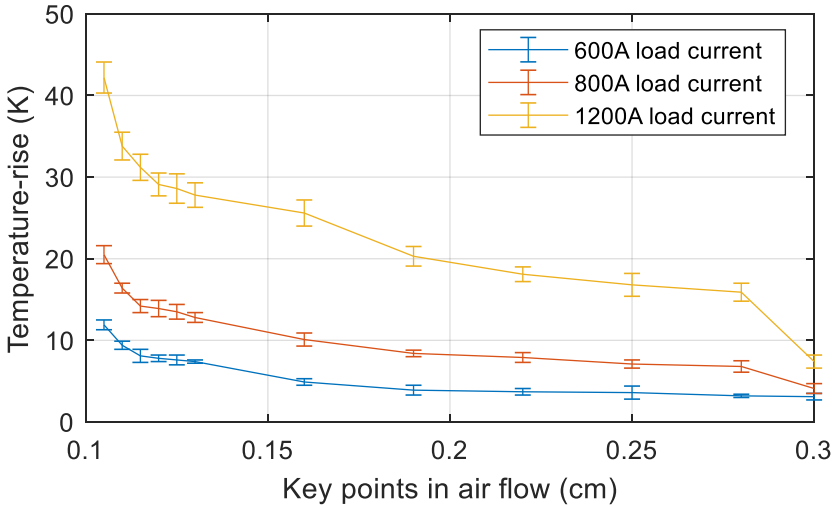

Fig. 5. 10 Air temperature-rise measured at different load currents

Table 5. 8 Wall temperature-rise measured under different load currents

Temperature-rise (K) / Key points on the wall	600 A load current Experiment	800 A load current Experiment	1200 A load current Experiment
$G_1(0.34,0.2,0.3)$	1.2 ± 0.6	2.9 ± 0.6	7.1 ± 0.8
$G_2(0.34,0.25,0.3)$	0.8 ± 0.4	2.4 ± 0.2	6.4 ± 0.7
$G(0.34,0.3,0.3)$	0.4 ± 0.2	0.4 ± 0.8	0.9 ± 0.8
$H_4(0.34,0.3,0.24)$	0.8 ± 0.3	1.7 ± 0.6	4.8 ± 1.0
$H_3(0.34,0.3,0.18)$	0.7 ± 0.2	1.6 ± 0.5	4.1 ± 0.6
$H_2(0.34,0.3,0.12)$	0.8 ± 0.7	1.4 ± 0.7	2.4 ± 0.5
$H_1(0.34,0.3,0.06)$	0.6 ± 0.5	0.6 ± 0.4	1.1 ± 0.5
$J(0.34,0.225,0)$	0.4 ± 0.4	0.2 ± 0.3	0.8 ± 0.4

5.4 Validation of numerical results

In this section, the comparison between numerical and experimental results is carried out. To validate the numerical model, its results, in terms of solid conductor temperature, air temperature and solid boundary wall temperature, are compared with the experimental data obtained using the test set-up described in Chapter 3. Before discussing the validation, a study for suitable boundary condition of the CFD model was conducted first.

5.4.1 Influence of boundary conditions

A study was carried out to confirm the suitability of boundary conditions, that are physically correct and possible to implement in COMSOL. As stated above, there are two common ways to set the boundary conditions when numerically calculating the thermal-flow filed, i.e. setting the boundary with constant temperature or setting the boundary with heat flux. Referring to relevant international standards (IEC 60694), the temperature for the wall of switching or control gear could be set as the ambient temperature or as a constant temperature. If the boundary could be set as a constant temperature, the implementation will be easy and convergence faster.

The case of 800 A was randomly chosen and taken as an example in this boundary condition study, results from two different boundary conditions were compared under the 800 A load current.

The first boundary condition is to set a constant temperature on each solid wall. The value of the temperature of each wall is determined from experimental data. In the experimental setup, several thermocouples were placed on the outside wall of the enclosure, and the measurement values were averaged and then used as the average temperature of each wall. For example, in Figure. 3.11, the temperatures measured at point G_1, G_2 and G, were averaged to represent the temperature of the top wall in

our busbar compartment model. From the experimental data at 800 A load current, the top wall and side walls are all averaged and then set as 20 ^{o}C.

On the other hand, the second boundary condition is to set the heat flux from the enclosure boundary to outside environment. By the definition of ambient temperature in IEC 60694, the busbar compartment model should be placed in a larger dimension domain. The boundary of the large dimension domain should be set as 1 m away to each side wall of the busbar compartment model, and then the boundary of the large dimension domain is set as ambient temperature, whilst enclosure boundary is set to a heat flux. The simulation model of this boundary condition requires numerous computer memory. Therefore, the boundary condition of heat flux is simplified as only taking the busbar compartment model into consideration, and the outside dimension of the air is neglected. The heat flux boundary is governed by Newton's cooling law and Stefan-Boltzmann theory, equation (2-13) and (2-14). In these two equations, the only parameter of heat transfer coefficient h is from empirical formula, its value which was used for our scenarios is from 5 to 7.5 [52]. It was found through sensitivity study that the exact value of h in the range between 5 to 7.5 does not significantly change the simulation results. Taking the scenario of 800 A load current as an example, the heat dissipated by convection of enclosure wall was estimated as 5.25 W, then the average temperature difference of the walls was evaluated as 0.35 ^{o}C when choosing different heat transfer coefficient as 5 or 7.5 using equation (2-10). From the results of sensitivity study of h, its value was selected as 5, which matched well with the experimental data.

Next, results of these two boundary conditions are compared in two aspects, i.e. the temperature distribution and flow filed with a 3D plot.

The first comparison is for the temperatures in the solid copper conductor, as shown in Table 5.9.

Table 5. 9 Busbar temperature-rise comparison between experimental and simulation results of different boundary conditions

Temperature -rise (K) / Points along busbar	800 A load current Experiment	800 A Load current Simulation with constant temperature boundary	Temperature difference Simulation-Experiment	800 A Load current Simulation with heat flux boundary	Temperature difference Simulation-Experiment
$l = 0\ cm$	26.1 ± 0.4	26.10	0	26.10	0
$l = 10\ cm$	27.0 ± 0.3	26.82	-0.18	26.92	-0.1
$l = 20\ cm$	27.8 ± 0.4	27.60	-0.2	27.85	-0.25
$l = 30\ cm$	28.6 ± 0.8	28.38	-0.22	28.47	-0.09
$l = 34\ cm$	28.7 ± 0.6	28.47	-0.23	28.58	-0.11

From Table 5.9, it can be seen that both boundary condition settings yield good agreements with experimental results in terms of the temperature prediction of solid conductor. Compared with experimental results, the maximum value of temperature difference is 0.23 ^{o}C for constant temperature boundary condition, whilst the maximum value of temperature difference for the heat flux boundary condition is 0.11 ^{o}C. Both temperature differences are within 2 ^{o}C of measurement accuracy and can be regarded as acceptable.

The differences of thermal boundary layer under the two boundary conditions are compared, which are plotted in Figure 5.11 and 5.12. These two figures both plot the middle x-z plane of the busbar compartment model.

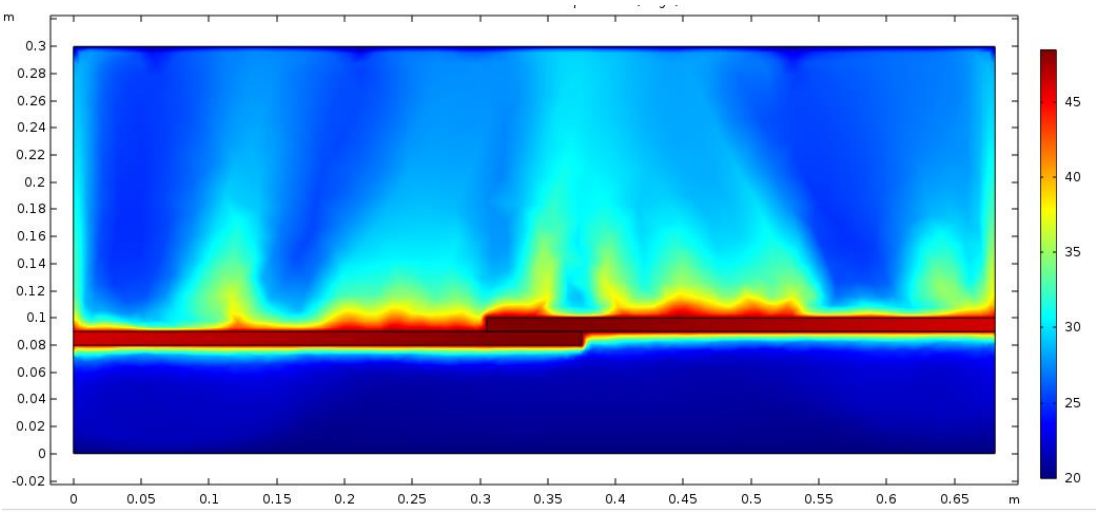

Fig. 5. 11 Temperature distribution (°C) in the x-z middle plane with constant temperature boundary condition

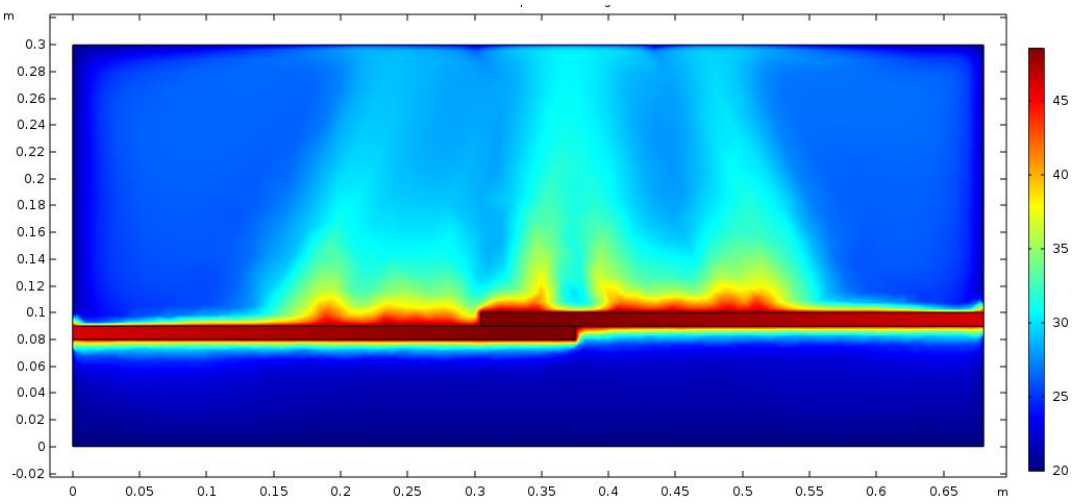

Fig. 5. 12 Temperature distribution (°C) in the x-z middle plane with heat flux boundary condition

In Figure 5.11 and Figure 5.12, the flow patterns are for both conditions nearly the same, as air has a trend to move to the busbar joint area and go up by buoyancy force, whilst the condition of constant temperature has some hot spots on the busbar and strong air flow near the terminal of the busbar. This is because the two side walls in y-z plane are set as thermal-insulated in the boundary condition of constant

temperature, and heat which should have been dissipated by the side walls have no way to dissipate but taken into air.

The next comparison of temperature is focused on the air flow in the middle y-z plane, the values of temperature-rise at the same points are found as shown in Table 5.10 and comparisons are made between the different boundary conditions and the experimental results:

Table 5. 10 Air flow temperature-rise comparison between experimental and simulation results of different boundary conditions

Temperature-rise (K) / Points on busbar	800 A Load current Experiment	800 A load current Simulation with constant temperature boundary	Temperature difference Simulation-Experiment	800 A load current Simulation with heat flux boundary	Temperature difference Simulation-Experiment
I_1	20.5 ± 1.1	22.62	2.12	23.08	2.58
I_2	16.4 ± 0.6	19.05	3.15	19.24	3.34
I_3	14.2 ± 0.8	16.61	2.41	16.72	2.52
I_4	13.9 ± 1.0	15.84	1.94	16.04	2.14
I_5	13.5 ± 0.9	15.17	1.67	15.81	2.31
I_6	12.8 ± 0.6	14.80	2.0	15.02	2.22
E_1	10.1 ± 0.8	11.58	1.48	12.86	2.76
E_2	8.4 ± 0.4	9.80	1.4	10.78	2.38
E_3	7.9 ± 0.6	9.02	1.12	10.04	2.14
E_4	7.1 ± 0.5	8.45	1.35	9.54	2.44
E_5	6.8 ± 0.7	8.42	1.62	9.25	2.45
E	4.1 ± 0.6	0	-4.1	5.01	0.91

From the above results, it can be seen that the temperature for the area of thermal boundary layer (from point I_1 to point I_6) between two boundary conditions show a tiny difference as 0.12 K to 0.64 K, whilst the temperature difference between two boundary conditions outside the thermal boundary layer is as large as 1.28 K.

For the air flow right above the busbar joint area, the air takes the energy from the surface and it flows towards the top boundary wall. Then the air has no way out but to follow the wall. Before reaching the bottom wall, the air can absorb some energy and go up again by buoyancy force.

The CFD results of temperature distribution and air flow direction are compared. In Figure 5.13 and 5.14, the temperature distribution and the air flow direction in this middle plane are shown, and it can be seen that the air flow field in the middle y-z plane indicated indirectly by the temperature distribution under these two different boundary conditions nearly are the same.

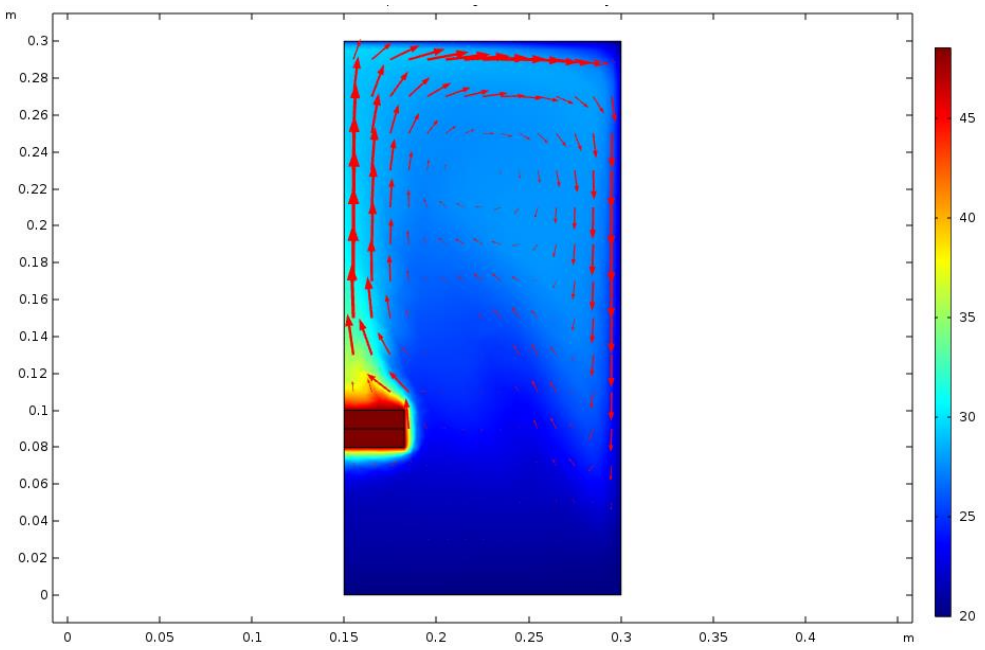

Fig. 5. 13 Temperature distribution (°C) and air flow arrows in middle y-z plane of heat flux setting boundary

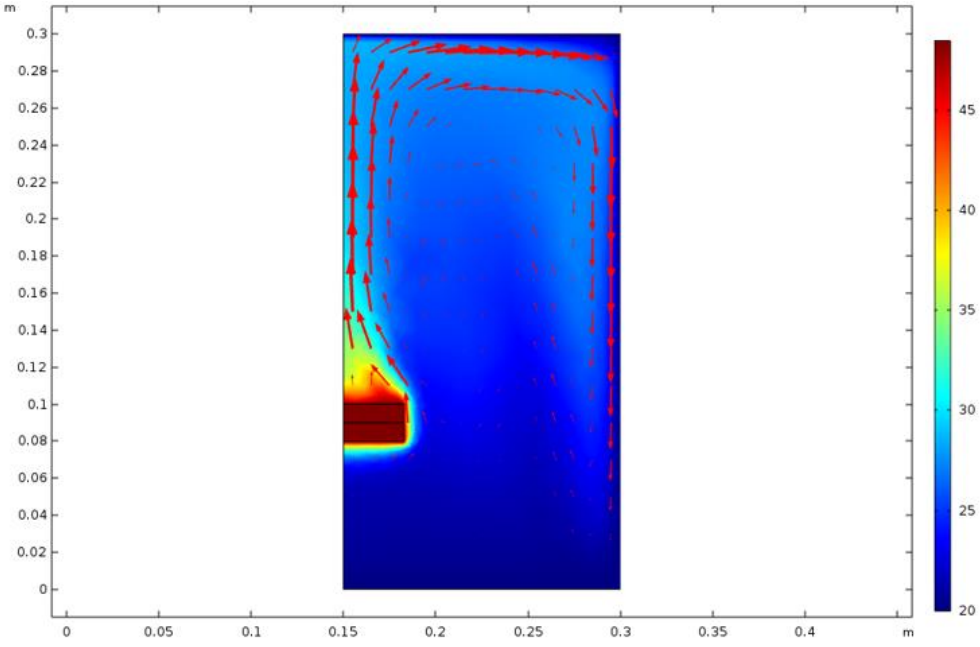

Fig. 5. 14 Temperature distribution (°C) and air flow arrows in middle y-z plane of constant temperature setting boundary

In conclusion, although the boundary condition of setting a constant temperature greatly saves time, it relies too much on the experimental data. The boundary condition of setting heat flux makes the governing equations more complicated and takes more time in the simulation process. Since it relies less on the data from experimental results and allows independent CFD simulation studies and design practice, the heat flux boundary condition should be used, and its results are also accurate.

5.4.2 Validation of thermal-flow models under different load currents

The accuracy of temperature prediction is checked in this section for other load currents. Results are obtained with the thermal flux boundary condition.

Referring to IEC standard 606934, steady-state can be regarded as achieved if the temperature change within 1 hour is less than 1 K. At the same time, the total acceptable uncertainty of experimental data is defined as 2 K, when considering the uncertainty of thermocouple.

Figure 5.15 shows the three-dimensional results of the temperature distribution and air direction arrows under 800 A load current as an example. It meets the physical analysis and prediction, the air absorbs the energy from busbar and dissipate the heat towards outside environment by enclosure wall. The hot air goes up towards to the top wall, and follow the top wall to side walls, and then re-gather to the busbar area again.

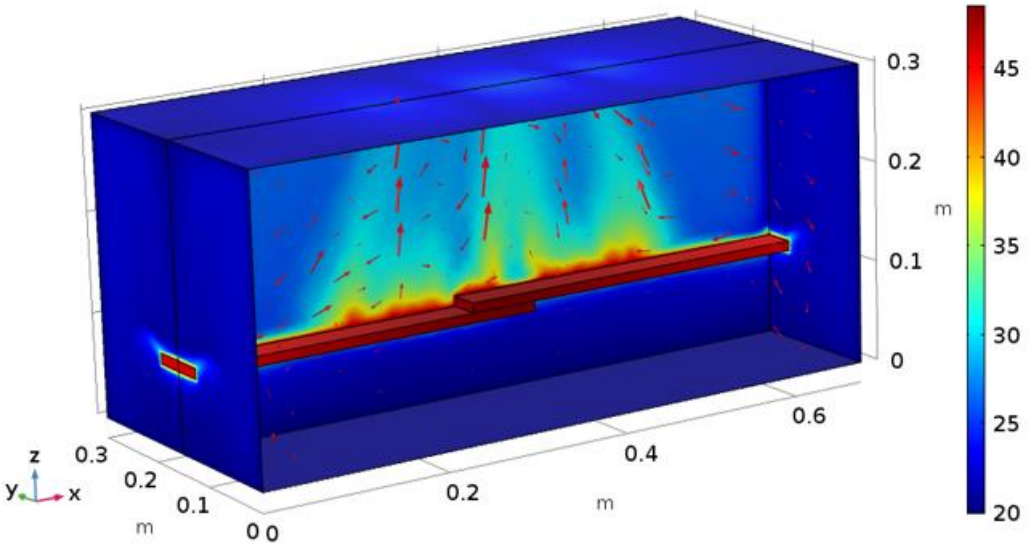

Fig. 5. 15 Temperature distribution (°C) and air velocity in three-dimension

5.4.2.1 Conductor temperature

The busbar is the only heat source in the busbar compartment model, and the temperature distribution of solid conductor is a vital part to predict since it has the highest temperature in the compartment. The comparison is done with different load currents, 600 A, 800 A and 1200 A, as shown in Figures 5.16 to 5.18 below, the reference point from where distance is measured is point A in Figure 3.13.

Table 5. 11 Busbar temperature comparison between experiment and simulation at 600 A load current

Temperature-rise (K) / Points along busbar	600 A load current Experiment	600 A load current Simulation
$l = 0\ cm$	14.4 ± 0.4	14.40
$l = 10\ cm$	15.0 ± 0.3	14.92
$l = 20\ cm$	15.5 ± 0.3	15.57

$l = 30\ cm$	16.0 ± 0.6	15.91
$l = 34\ cm$	16.4 ± 0.8	16.08

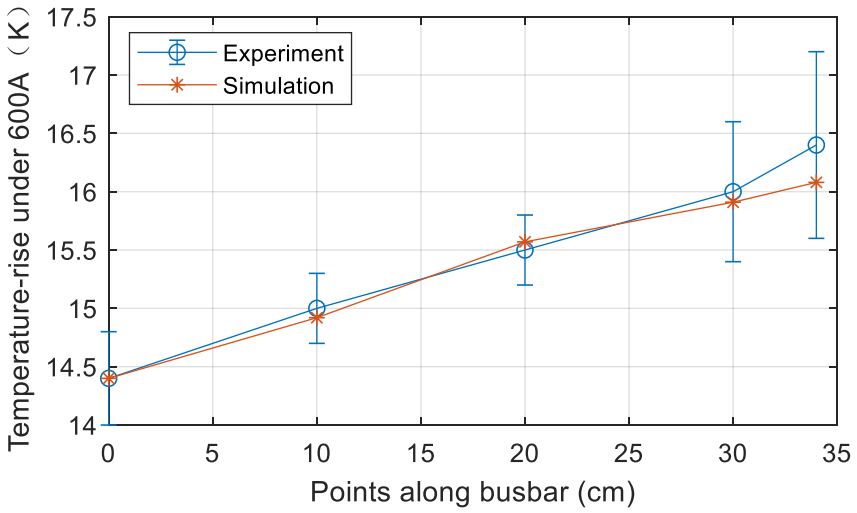

Fig. 5. 16 Comparison of measured and simulated busbar temperature-rise at 600 A load current

Table 5. 12 Comparison of measured and simulated busbar temperature-rise at 800 A load current

Temperature-rise (K) / Points along busbar	800 A load current Experiment	800 A load current Simulation
$l = 0\ cm$	26.1 ± 0.4	26.10
$l = 10\ cm$	27.0 ± 0.3	26.92
$l = 20\ cm$	27.8 ± 0.4	27.85
$l = 30\ cm$	28.6 ± 0.8	28.47
$l = 34\ cm$	28.7 ± 0.6	28.58

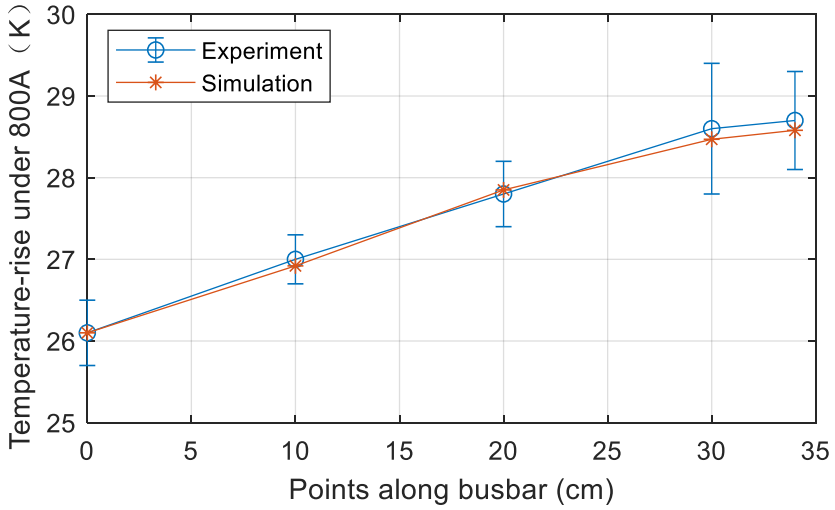

Fig. 5. 17 Comparison of measured and simulated busbar temperature-rise at 800 A load current

Table 5. 13 Comparison of measured and simulated busbar temperature-rise at 1200 A load current

Temperature-rise (K) / Points along busbar	1200 A load current Experiment	1200 A load current Simulation
$l = 0\ cm$	53.4 ± 0.7	53.40
$l = 10\ cm$	54.9 ± 0.8	55.40
$l = 20\ cm$	56.7 ± 0.8	57.38
$l = 30\ cm$	57.8 ± 0.6	59.25
$l = 34\ cm$	58.2 ± 0.5	59.60

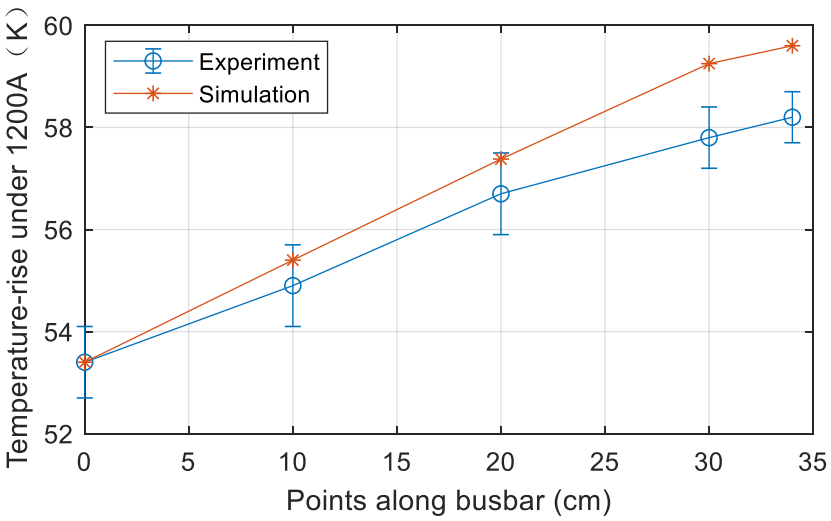

Fig. 5. 18 Comparison of measured and simulated busbar temperature-rise at 1200 A load current

From the above results, it can be easily seen that the simulation results show a high agreement with the experimental results. At the current load of 600 A and 800 A, the maximum temperature difference along busbar is 0.8 K. For the scenario under 1200 A, the predicted temperature along the busbar is 1.45 K higher than the experimental results in average, whilst the temperature difference is still within 2 K.

This highly accurate prediction of temperature distribution along busbar is mainly due to the fact that the boundary condition set on the terminal of copper busbar with the measured temperature.

5.4.2.2 Temperature in air flow

Although the temperatures of the terminals of busbar are set as the known boundary condition, it cannot ensure the accurate numerical solution for the temperature and velocity of air flow. The velocity of air was not easily and directly measured, however the temperature of air was measured to indirectly describe the direction and severity the air flow. Therefore, the prediction of temperature distribution in air flow is vitally important for the validation process.

In this section, the temperatures of air between experiment and simulation are compared. Considering the extrusion length of the thermocouple sensor as 2 mm in Figure 3.8, the spatial temperature results from numerical solution have been averaged for the area with a radius 2 mm away the points I to E (Figure 3.11).

Table 5. 14 Comparison of measured and simulated air temperature-rise at key points at 600 A current load

Temperature-rise (K) / Key points in air fluid	600 A load current Experiment	600 A load current Simulation
$I_1(0.34,0.15,0.105)$	11.9 ± 0.6	13.41
$I_2(0.34,0.15,0.110)$	9.4 ± 0.5	11.46
$I_3(0.34,0.15,0.115)$	8.1 ± 0.8	10.38
$I_4(0.34,0.15,0.120)$	7.8 ± 0.4	9.84
$I_5(0.34,0.15,0.125)$	7.6 ± 0.6	9.61
$I_6(0.34,0.15,0.130)$	7.4 ± 0.2	9.35
$E_1(0.34,0.15,0.160)$	4.9 ± 0.4	7.69
$E_2(0.34,0.15,0.190)$	3.9 ± 0.6	6.37
$E_3(0.34,0.15,0.220)$	3.7 ± 0.4	5.85
$E_4(0.34,0.15,0.250)$	3.6 ± 0.8	5.67
$E_5(0.34,0.15,0.280)$	3.2 ± 0.2	5.45
$E(0.34,0.15,0.300)$	3.1 ± 0.4	2.54

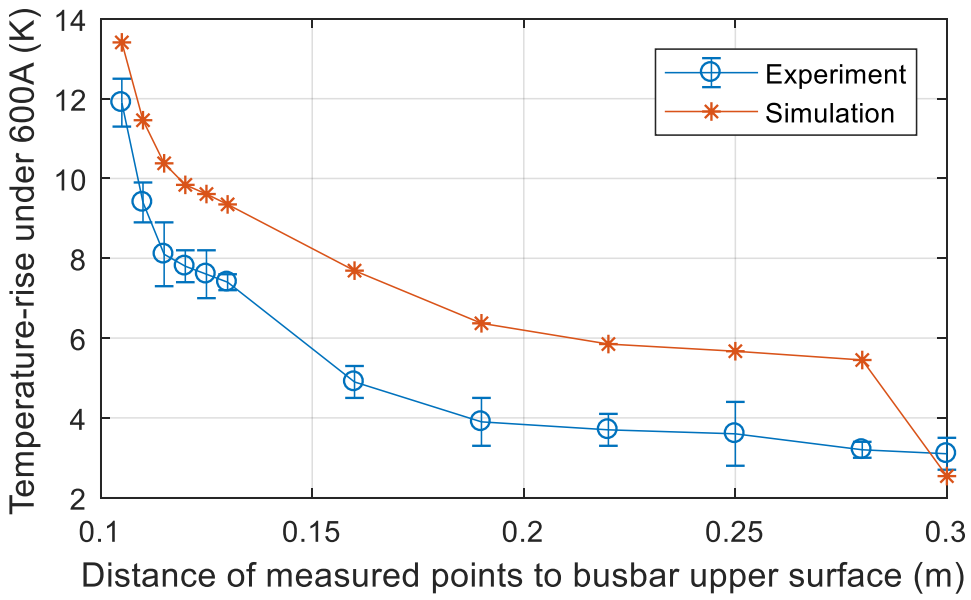

Fig. 5. 19 Comparison of measured and simulated air temperature-rise at key points at 600 A load current

Table 5. 15 Comparison of measured and simulated air temperature-rise at key points at 800 A load current

Temperature-rise (K) / Key points in air fluid	800 A load current Experiment	800 A load current Simulation
$I_1(0.34,0.15,0.105)$	20.5 ± 1.1	23.08
$I_2(0.34,0.15,0.110)$	16.4 ± 0.6	19.24
$I_3(0.34,0.15,0.115)$	14.2 ± 0.8	16.72
$I_4(0.34,0.15,0.120)$	13.9 ± 1.0	16.04
$I_5(0.34,0.15,0.125)$	13.5 ± 0.9	15.81
$I_6(0.34,0.15,0.130)$	12.8 ± 0.6	15.02
$E_1(0.34,0.15,0.160)$	10.1 ± 0.8	12.86
$E_2(0.34,0.15,0.190)$	8.4 ± 0.4	10.78
$E_3(0.34,0.15,0.220)$	7.9 ± 0.6	10.04
$E_4(0.34,0.15,0.250)$	7.1 ± 0.5	9.54
$E_5(0.34,0.15,0.280)$	6.8 ± 0.7	9.25
$E(0.34,0.15,0.300)$	4.1 ± 0.6	5.01

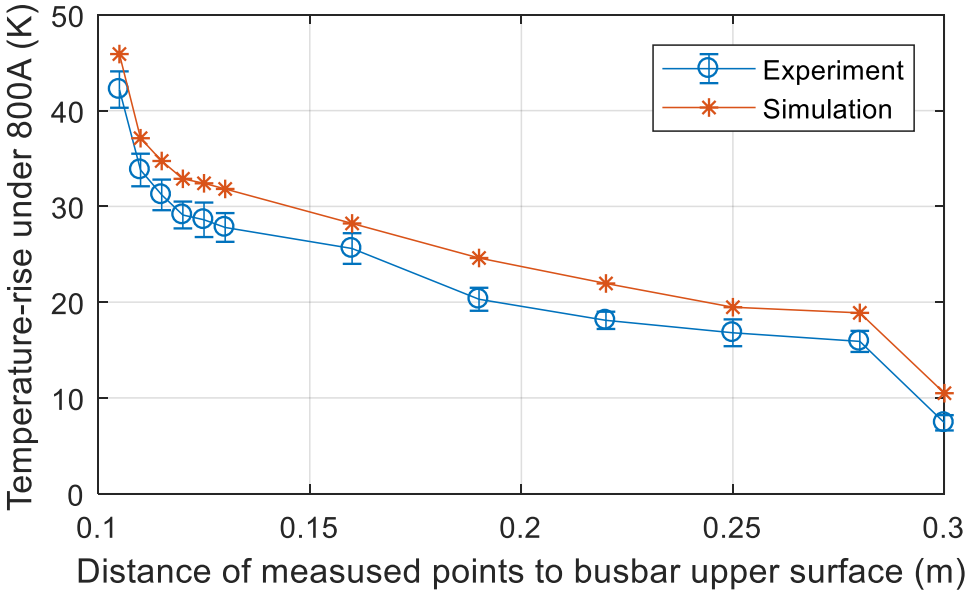

Fig. 5. 20 Comparison of measured and simulated air temperature-rise at key points at 800 A load current

Table 5. 16 Comparison of measured and simulated air temperature-rise at key points at 1200 A load current

Temperature-rise (K) / Key points in air fluid	1200 A load current Experiment	1200 A load current Simulation
$I_1(0.34,0.15,0.105)$	42.2 ± 1.9	45.91
$I_2(0.34,0.15,0.110)$	33.8 ± 1.7	37.12
$I_3(0.34,0.15,0.115)$	31.2 ± 1.6	34.74
$I_4(0.34,0.15,0.120)$	29.1 ± 1.4	32.88
$I_5(0.34,0.15,0.125)$	28.6 ± 1.8	32.41
$I_6(0.34,0.15,0.130)$	27.8 ± 1.5	31.82
$E_1(0.34,0.15,0.160)$	25.6 ± 1.6	28.22
$E_2(0.34,0.15,0.190)$	20.3 ± 1.2	24.61
$E_3(0.34,0.15,0.220)$	18.1 ± 0.9	21.95
$E_4(0.34,0.15,0.250)$	16.8 ± 1.4	19.47
$E_5(0.34,0.15,0.280)$	15.9 ± 1.1	18.88
$E(0.34,0.15,0.300)$	7.4 ± 0.8	10.49

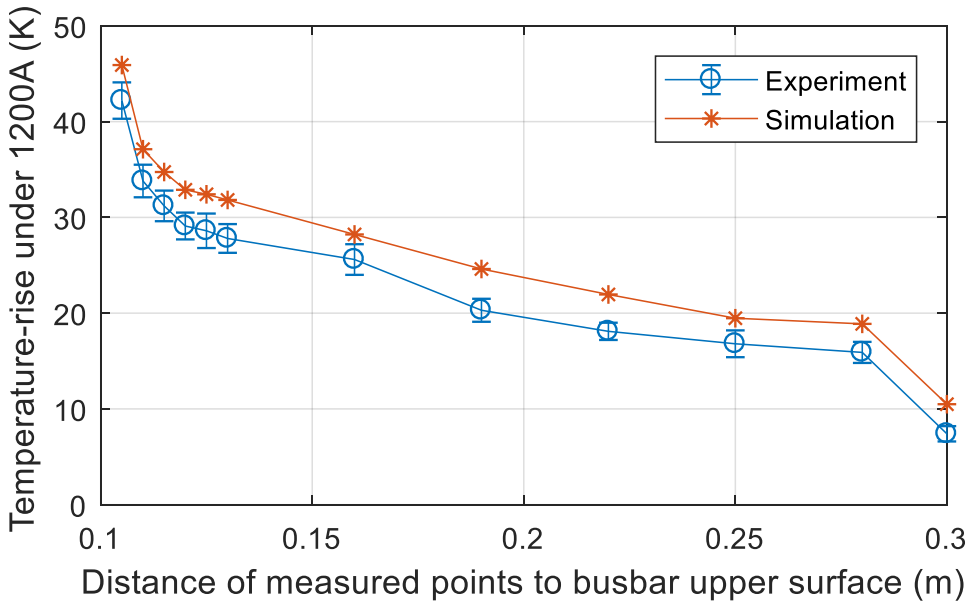

Fig. 5. 21 Comparison of measured and simulated air temperature-rise at key points at 1200 A load current

From the above results, it can be seen that the differences between measured and simulated temperatures at the same physical locations are nearly the same from point I_1, I_2, I_3, I_4, I_5, I_6, E_1, E_2, E_3, E_4 to point E_5 under each individual load current. The average value of temperature differences under each individual load is given in Table 5.17:

Table 5.17 Average of temperature differences between simulation and experiment results in air flow versus load current

Load Current (A)	600	800	1200
Average of temperature-rise difference between simulation and experiment (K)	2.14	2.48	3.48

In low temperature conditions, the air velocity has a linear relationship with the temperature of air. Therefore, the results above prove that the air flow in the 3D numerical simulation results flows in the same velocity as those in the experiments.

The above comparison also shows the experiment and simulation temperature distribution of air flows in the y-z middle plane have the same trend of temperature drop. The high temperature gradient near the surface, which is assumed as thermal boundary layer, have been shown both in simulation and experimental results, as in Figure 5.19 to Figure 5.20. However, the experimental results are slightly smaller than the simulation results, it is mainly caused by the in-perfect seal of busbar compartment model, and some other supporting tubes in the enclosure. It can be concluded that the temperature difference is increased with the increase of load current, and the value is as large as 3.48 K under the 1200 A load current. This might be caused by the strong air flow, which makes the temperature right above the busbar joint change more than 1 K within 1 hour time even in a steady-state condition.

5.4.2.3 Wall temperature

When a large switching or control gear works in its normal condition with high load current, it is difficult or unsafe to measure the temperature inside. However, the temperature distribution inside the gear or cabinet is vitally important to ensure the safe working condition for metal conductor and supporting insulator. If we can simulate the gear or the cabinet and deem the simulation to be correct, then by monitoring the temperature distribution along the wall, we could indirectly derive the thermal condition inside the cabinet or the gear.

Therefore, the temperature distributions on the enclosure wall between experimental and simulation results are compared in this section. The comparison was done for the top wall, one side wall of x-z plane and bottom wall.

Table 5. 17 Comparison of measured and simulated air temperature-rise at wall points under 600 A load current

Temperature-rise (K) / Key points on the wall	600 A load current Experiment	600 A load current Simulation
$G_1(0.34,0.2,0.3)$	1.2 ± 0.6	2.00
$G_2(0.34,0.25,0.3)$	0.8 ± 0.4	1.34
$G(0.34,0.3,0.3)$	0.4 ± 0.2	0.11
$H_4(0.34,0.3,0.24)$	0.8 ± 0.3	1.21
$H_3(0.34,0.3,0.18)$	0.7 ± 0.2	0.98
$H_2(0.34,0.3,0.12)$	0.8 ± 0.7	0.75
$H_1(0.34,0.3,0.06)$	0.6 ± 0.5	0.42
$J(0.34,0.225,0)$	0.4 ± 0.4	0

Table 5. 18 Comparison of measured and simulated air temperature-rise at wall points under 800 A load current

Temperature-rise (K) / Key points on the wall	800 A load current Experiment	800 A load current Simulation
$G_1(0.34,0.2,0.3)$	2.9 ± 0.6	3.84
$G_2(0.34,0.25,0.3)$	2.4 ± 0.2	2.77
$G(0.34,0.3,0.3)$	0.4 ± 0.8	0.54
$H_4(0.34,0.3,0.24)$	1.7 ± 0.6	2.38
$H_3(0.34,0.3,0.18)$	1.6 ± 0.5	1.91
$H_2(0.34,0.3,0.12)$	1.4 ± 0.7	1.62
$H_1(0.34,0.3,0.06)$	0.6 ± 0.4	0.99
$J(0.34,0.225,0)$	0.2 ± 0.3	0

Table 5. 19 Comparison of measured and simulated air temperature-rise at wall points under 1200 A load current

Temperature-rise (K) / Key points on the wall	1200 A load current Experiment	1200 A load current Simulation
$G_1(0.34,0.2,0.3)$	7.1 ± 0.8	8.54
$G_2(0.34,0.25,0.3)$	6.4 ± 0.7	6.38
$G(0.34,0.3,0.3)$	0.9 ± 0.8	1.57
$H_4(0.34,0.3,0.24)$	4.8 ± 1.0	5.34
$H_3(0.34,0.3,0.18)$	4.1 ± 0.6	4.86
$H_2(0.34,0.3,0.12)$	2.4 ± 0.5	2.68
$H_1(0.34,0.3,0.06)$	1.1 ± 0.5	1.75
$J(0.34,0.225,0)$	0.8 ± 0.4	0

The results from Table 5.18 to Table 5.20, all are shown that the temperature difference between simulation and experimental results are within 2 K. Therefore, the simulation provided an accurate temperature distribution along the wall of the busbar compartment model.

5.5 Summary

CFD modelling is one of the most popular methods to study thermal behaviour of power apparatus at this computer age, however the simulation principle need to be validated first before it is commonly used in apparatus design. The mesh refinement study was firstly carried out and a suitable boundary condition was found and validated of the busbar compartment model under study. The experimental results mainly the temperature of busbar, busbar joint and the air temperature above the busbar were then introduced. The simulation results are then compared with the experimental results and both show a high degree of agreement. Therefore, it was

concluded that the principles of the model are correct, and they can be used to build a complete switching cabinet structure to help optimize the design

Chapter 6 Conclusion and Future Work

6.1 Summary and conclusion

The temperature-rise phenomenon in a model busbar compartment has been studied. The work contains two parts. The first part is to measure the contact resistance and temperature-rise, and the second part is to establish a three-dimensional model to predict the temperature distribution in the busbar compartment.

Contact resistance is a result of the electrical connection of two conductors where effective conducting area is drastically reduced due to surface roughness. It leads to the production of surface heating and contributes towards temperature-rise and formation of hot spot. In the present work the applicability a widely used contact resistance model, the C-M-Y model, has been studied. The empirical parameters of the C-M-Y model were re-evaluated based on the geometry of the model busbar compartment and the measured contact resistance at different temperatures. Results show that the prediction based on the C-M-Y model agree reasonably well with the experimental results in a wide range of applied pressure between the surfaces. For example, the contact resistance was calculated as 1.15 μΩ under 14.7 MP_a using the C-M-Y model whilst the resistance was measured as 1.11 μΩ under the same pressure used in experiment.

The temperature-rise measurement in the present experiment has a maximum uncertainty of 2 ^oC after the systematic error of the measurement system was corrected. Within the model busbar compartment, the highest temperature-rise is located on the busbar joint with a value of 16.4 K at 600 A, 28.7 K at 800 A and 58.2 K at 1200 A of load current. The thickness of the thermal layer in air where rapid temperature drop takes place near the busbar surface is about 1.18 mm.

The three-dimensional model established in the present work considers the variation of material properties as a function of temperature. The influence of mesh size was studied first and it has been found that using a total grid of 24690 with a typical mesh size of 0.002235 m^3 near the busbar surface, the results are computationally accurate. The simulation and experimental results of temperature-rise in busbar show a good agreement. The maximum temperature difference of these results was 1.45 K, which is within the uncertainty of temperature measurement. As for the fluid in the enclosure, the temperature-rise of air in the simulation model was slightly different from the experimental ones, with a value of 2.14 K at 600 A, 2.48 K at 800 A and 3.48 K at 1200 A. The experimental results are lower than the simulation results, which is mainly caused by the in-perfect seal of the model busbar compartment on its both sides, and some other supporting tubes in the enclosure. It was observed that the temperature difference is increased with the increase of load current, and the maximum value is 3.48 K at 1200 A load current. The larger temperature difference at higher current is also partly caused by the instable natural convection flow right above the busbar joint under the present experimental conditions. This is evidenced by the observation that the air temperature over the busbar experiences a variation of 1 K within 1 hour even when the overall temperature field of the busbars reaches a steady-state situation.

6.2 Future work

The work presented in this thesis indicated that the simulation methodology applied in the model busbar compartment is also applicable to the thermal-flow field calculation in other electrical apparatus. In order to further improve the accuracy of prediction, there is some future work which could be implemented as following:

- The validation process in Chapter 4 is only specific for the busbar joint in our model. In switching cabinet or other large-size electrical apparatus, there are

some different and more complex geometries of contact area, such as tulip contact finger in circuit breaker. The parameters, affected by temperature and pressure, are needed to accurately predict the maximum temperature-rise for solid component.

- In Chapter 5, all the CFD simulation models took a long time to obtain a convergent model. By mesh refinement study, the simulation process could save time by find a suitable mesh element number. However, it is assumed that the individual mesh element size of fluid is mainly dependent on the fluid velocity. To help industry optimize the design, the size of mesh element should be determined for various velocity of flow.
- In Chapter 5, a method is provided to predict the temperature-rise inside the large-size electrical apparatus by measuring the temperature at the boundary wall. This method could help online monitoring to predict the thermal behaviour of the apparatus in normal operation. This method needs to be validated for metal-enclosure apparatus, where the temperature difference among different points on the boundary wall is larger than the values on the Perspex wall used in the present study.

References

[1] Wikipedia, ''Ultra-high voltage electricity transmission in China.'' [Online]. Available: https://en.wikipedia.org/wiki/Ultra-high-voltage_electricity_transmission_in_China. [Accessed: 14-Feb-2018].

[2] J. D. Yan, "Prediction of electrical heating and thermal management for switching equipment," University of Liverpool, Liverpool, 2014.

[3] M. Rajagopal, K. Seetharamu, and P. Ashwathnarayana, "Transient thermal analysis of induction motors," *Proceeding of the 1996 International Conference on Power Electronics, Drives and Energy Systems for Industrial Growth*, pp. 932-939, 1996.

[4] H. K. Versteeg and W. Malalasekera, *''An introduction to computational fluid dynamics: the finite volume method,''* 2nd ed. Pearson Education Press, 2007.

[5] J. Paulke, H. Weichert, and P. Steinhaeuser, "Thermal simulation of switchgear," *IEEE Transactions on Components and Packaging Technologies,* vol. 25, pp. 434-439, 2002.

[6] Wikipedia, ''History of Switchgear.'' [Online]. Avalible: https://en.wikipedia.org/wiki/Switchgear. [Accessed: 27-Jan-2018].

[7] J.-m. Zhang, C. Gao, H. Feng, G.-c. Yan, F. Zhao, D.-l. Yuan, "A coupled three-dimensional fluid-thermal fields analysis of KYN28A-12 switch cabinet," *Proceeding of 1st International Conference on Electric Power Equipment-Switching Technology (ICEPE-ST)*, pp. 466-470, 2011.

[8] Common specifications for high-voltage switchgear and controlgear standards, IEC 60694, 2002.

[9] A.C. metal-enclosed switchgear and controlgear for rated voltages above 1 KV and up to and incluiding 52 KV, IEC 60298, 1996.

[10] P. Mellor, D. Roberts, and D. Turner, "Lumped parameter thermal model for electrical machines of TEFC design," *IEE Proceedings B (Electric Power Applications)*, pp. 205-218, 1991.

[11] A. Boglietti, A. Cavagnino, M. Lazzari, and M. Pastorelli, "A simplified thermal model for variable-speed self-cooled industrial induction motor," *IEEE Transactions on Industry Applications,* vol. 39, pp. 945-952, 2003.

[12] D. Staton, "Thermal computer aided design-advancing the revolution in compact motors," *Proceeding of IEEE International Electric Machines and Drives Conference,* Boston, pp. 858-863, 2001.

[13] A. Boglietti, A. Cavagnino, D. Staton, M. Shanel, M. Mueller, and C. Mejuto, "Evolution and modern approaches for thermal analysis of electrical machines," *IEEE Transactions on Industrial Electronics,* vol. 56, pp. 871-882, 2009.

[14] A. Boglietti, A. Cavagnino, and D. A. Staton, "TEFC induction motors thermal models: A parameter sensitivity analysis," *IEEE Transactions on Industry Applications,* vol. 41, pp. 756-763, 2005.

[15] Y. Lee, S.-Y. Hahn, and S. K. Kauh, "Thermal analysis of induction motor with forced cooling channels," *IEEE Transactions on Magnetics,* vol. 36, pp. 1398-1402, 2000.

[16] D. A. Staton and A. Cavagnino, "Convection heat transfer and flow calculations suitable for electric machines thermal models," *IEEE Transactions on Industrial Electronics,* vol. 55, pp. 3509-3516, 2008.

[17] C. Mejuto, M. Mueller, M. Shanel, A. Mebarki, and D. Staton, "Thermal modelling investigation of heat paths due to iron losses in synchronous machines," *Proceeding of 4th Interantional Conference on Power Electronics, Machines and Drives*, April 2008.

[18] S. Kim, H. Kim, S. Hahn, B. Lee, K. Park, Y. Shin*, et al.*, "Coupled finite-element-analytic technique for prediction of temperature rise in power apparatus," *IEEE Transactions on Magnetics,* vol. 38, pp. 921-924, 2002.

[19] J. Mugglestone, S. Pickering, and D. Lampard, "Effect of geometric changes on the flow and heat transfer in the end region of a TEFC induction motor," *Proceeding of Ninth International Conference on Electrical Machines and Drives*, pp. 40-44, 1999.

[20] S. Pickering and D. Lampard, "Recent Advancement in the Thermal Design of Electric Motors," *Proceeding of SMMA 2001 Fall Technology Conference*, pp. 1-11, 2011.

[21] M. Shanel, S. Pickering, and D. Lampard, "Conjugate heat transfer analysis of a salient pole rotor in an air cooled synchronous generator," *Proceeding of IEEE IEMDC on Electric Machines and Drives,* pp. 737-741, 2003.

[22] W.-B. Yang, S.-J. Mo, D. Lianga, and F.-J. Zhen, "Numerical Study of Overheat Fault in Copper Wire Caused by Bad Contact Base on Multi-physics Coupling," *Proceeding of 7th International Conference on Intelligent Computation Technology and Automation (ICICTA),* pp. 400-405, 2014.

[23] J.-K. Kim, J.-Y. Lee, S.-B. Wee, and S.-C. Hahn, "A novel coupled magneto-thermal-flow analysis for temperature rise prediction of power apparatus," *Proceeding of IEEE ICEMS on Electrical Machines and Systems,* pp. 585-588, 2008.

[24] P. U. Frei and H. O. Weichert, "Advanced thermal simulation of a circuit breaker," *Proceedings of the 50th IEEE Holm Conference on Electrical Contacts and the 22nd International Conference on Electrical Contacts*, pp. 104-110, 2004.

[25] J. N. Fox, *"Temperature Coefficient of Resistance,"* 1st ed. Physics Education Pressed, 1990.

[26] Resistivity, ''Metal Resistivity Temperature Coeffcient.'' [Online]. Available: http://www.endmemo.com/physics/resistt.php

[27] C. W. Weißenfels, P. Comput Mech, "Numerical modeling of electrical contacts," *Computational Mechanics,* vol. 46, pp. 301–314, 2010.

[28] R. holm, ''*Electrical contact,''* 4th ed. Springer-Verlag Pressed, Berlin, 2000.

[29] M. Pinnel and K. Bradford, "Influence of some geometric factors on contact resistance probe measurements," *IEEE Transactions on Components, Hybrids, and Manufacturing Technology,* vol. 3, pp. 159-165, 1980.

[30] J.-M. Depond, D. Leroy, L. Oberli, and D. Richter, "Examination of contacts between strands by electrical measurement and topographical analysis," *IEEE Transactions on applied superconductivity,* vol. 7, pp. 793-796, 1997.

[31] G. Moustafa, "Studies on mechanical contact devices for bolted Bus-Bar connections," *International Journal of Applied Science and Engineering Research,* vol. 2, pp. 128-136, 2013.

[32] Y. Li, J. Duan, J. Liang, B. Li, and Y. He, "Study on contact resistance of 10kV switch cabinet," *Proceeding of IEEE PES Asia-Pacific on Power and Energy Engineering,* pp. 1450-1454, 2016.

[33] M. Vogler and S. Sheppard, "Electrical contact resistance under high loads and elevated temperatures," *Welding Journal,* vol. 9, pp. 231-238, 1993.

[34] J. Queffelec, N. B. Jamaa, D. Travers, and G. Pethieu, "Materials and contact shape studies for automobile connector development," *Proceedings of the Thirty-Sixth IEEE Holm Conference on Electrical Contacts and the Fifteenth International Conference on Electrical Contacts*, pp. 225-231, 1990.

[35] M. Grujicic, C. Zhao, and E. Dusel, "The effect of thermal contact resistance on heat management in the electronic packaging," *Applied Surface Science,* vol. 246, pp. 290-302, 2005.

[36] H. C. Hottel, *''Radiant heat transmission,''* 3rd ed. McGraw-Hill Pressed, New York, US, 1954.

[37] M. Cooper, B. Mikic, and M. Yovanovich, "Thermal contact conductance," *International Journal of heat and mass transfer,* vol. 12, pp. 279-300, 1969.

[38] ''*Thermal Contact Resistance Simulation*.'' [Online]. Available: https://www.comsol.com/blogs/thermal-contact-resistance-simulation/

[39] D. W. Hahn and M. N. Ã–zisik, ''*Heat conduction,''* 3rd ed. John Wiley & Sons Pressed, 2012.

[40] J. Holman, ''*Heat transfer,''* 1st ed. Mc Gran–Hill Book Company Pressed*,* Soythern Methodist University*,* 1992.

[41] C. L. Yaws, *''Handbook of transport property data: viscosity, thermal conductivity, and diffusion coefficients of liquids and gases,''* 1st ed. Gulf Publication Company Pressed, 1995.

[42] A. Aziz, "A similarity solution for laminar thermal boundary layer over a flat plate with a convective surface boundary condition," *Communications in Nonlinear Science and Numerical Simulation,* vol. 14, pp. 1064-1068, 2009.

[43] L. Prandtl, "On the motion of a fluid with very small viscosity," *Proceeding of 3rd International Mathematics Congress*, pp. 484-491, 1904.

[44] K.-J. Bathe and H. Zhang, "A mesh adaptivity procedure for CFD and fluid-structure interactions," *Computers & Structures,* vol. 87, pp. 604-617, 2009.

[45] D. Sharov and K. Nakahashi, "Hybrid prismatic/tetrahedral grid generation for viscous flow applications," *AIAA journal,* vol. 36, pp. 157-162, 1998.

[46] C. A. Brebbia and S. Walker, ''*Boundary element techniques in engineering*,'' 1st ed. Newnes Pressed, Dec 2013.

[47] C. Odiaka, "Temperature rise in a simplified electrical device," Univeristy of Liverpool, Liverpool, 2013.

[48] ''*Megger DLRO600 Low Resistance Ohmmeter Details*.'' [Online]. Available: https://www.tester.co.uk/megger-dlro600-low-resisitance-ohmeter

[49] D. C. P. T. Norris, *"Copper for Busbars,"* European Copper Institute Pressed, 2014.

[50] S. Melsom and H. Booth, "The efficiency of overlapping joints in copper and aluminium busbar conductors," *Journal of the Institution of Electrical Engineers,* vol. 60, pp. 889-899, 1922.

[51] ''*How to Implement a Mesh Refinement Study*.'' [Online]. Available: https://www.comsol.com/blogs/how-to-implement-mesh-refinement-study/ [Accessed: 2013]

[52] Heat transfer coefficient. *''Convective Heat Transfer.''* [Online]. Available: https://www.engineeringtoolbox.com/convective-heat-transfer-d_430.html